UNIVERSITÀ DEGLI STUDI DI CATANIA

Ph.D. in Science and Technology of Materials XXVIII Cycle

Ph.D. Thesis

Metal organic chemical vapor deposition of multifunctional fluoride phases

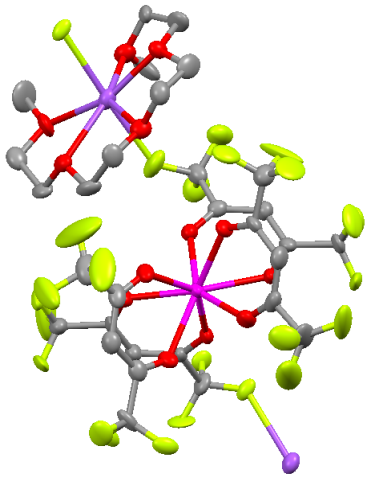

Ph.D. Student: ***Sergio Orazio Battiato***

Advisor:
Prof. Graziella Malandrino

Coordinator:
Prof. Maria Grazia Grimaldi

2012-2015

Contents

Introduction

Inorganic metal fluorides and oxide-fluorides have significant importance in the development of many new technologies, and are impacting various key points of modern life, that is, energy production and storage, microelectronics and photonics, catalysis, automotive, building, etc.

In the past few years, fluoride materials have attracted a great and increasing interest due to their multifunctional properties, such as ferroelectricity, induced ferro/antiferromagnetism, thermal stability, high transparency and low phonon energy. Among them, the study of ferroelectric, magnetic, and more recently, multiferroic properties has stimulated considerable interest.

In multiferroic materials, at least two of the three ferroic orders, ferroelectricity, ferromagnetism and ferroelasticity, coexist, exhibiting an interesting electromagnetic coupling.

The interesting coupling effect between the ferroic orders in these materials is of topical interest for their applications in advanced materials, especially in futuristic read-write electronic devices.

Currently, the research on multiferroic materials is directed towards Bi-containing perovskite such as $BiFeO_3$ or $BiMnO_3$ and toward both hexagonal and orthorhombic rare-earth manganites such as $HoMnO_3$ and $TbMnO_3$. In general, fluoride based compounds are highly symmetric and, for this reason, fluoride-based ferroelectric compounds are scarcely reported in literature.

Among the few known ferroelectric fluoride crystals, the barium fluoride $BaMF_4$ (M=Mg, Mn, Co, Ni, Zn) phases have recently caught substantial attention in view of their interesting and multifunctional properties.

The $BaMF_4$ isostructural compounds represent a rare example of ferroelectric fluorides. In these systems, the ferroelectricity is not due to the presence of ions usually considered to be "ferroelectrically active", such as empty d-shell cations or lone-pair active cations (e.g., Bi^{3+}, Pb^{2+}), but arises only from geometrical effects, which involve both rotational motions of the fluorine octahedra and polar displacements of the Ba cations. The instability is caused solely by size effects and geometrical constraints; no charge transfer between anions and cations occurs as a result of the

structural distortion. Therefore, the $BaMF_4$ multiferroics represent an example of proper "geometric ferroelectricity", a mechanism that has been proposed as a possible way to incorporate both magnetism and ferroelectricity in the same system.

The goal of this work is to explore a new class of multiferroic non-oxide based materials, focusing on the class of $BaMF_4$ systems, to widen the range of candidates for magnetoelectric device applications. In addition, fluoride compounds have compelling advantages for many optical applications due to their unique combination of low phonon energy, high UV absorption edge energy, and relatively weak crystal field.

Compared with oxides, fluorides are considered to be efficient hosts for down-conversion (DC) and upconversion (UC) luminescence of rare earth (RE) ions due to their low phonon energies and optical transparency over a wide wavelength range.

The choice of host materials is of great importance in designing lanthanide-based luminescent UC materials for efficient practical applications.

To date, lanthanide (Ln^{3+}) ions doped luminescent upconversion (UC) fluorides have been extensively investigated to develop potential applications, such as display devices, solid-state lasers, solar cells and biological imaging Over the past few years, considerable efforts have been devoted to select the ideal host materials. Among the fluorides reported, rare earth (RE) doped $NaYF_4$ and $NaGdF_4$ are considered as the most efficient DC and UC host lattices, and have recently raised increasing attention. Many applications of RE-doped fluorides have been demonstrated, such as lasers, optical communications, display devices, and so on. Furthermore, in literature it is possible to find out numerous demonstrations of the potential applications of these systems for both in vitro and in vivo high contrast imaging as well as for biodetection and biosensing applications.

On the other hand, trivalent RE-doped MF_2 (with M=Sr, Ca, Ba, Cd) compounds are also considered a suitable material characterized by low energy phonons (usually less than 300 cm^{-1}) and large transfer coefficients between the RE ions. In this typology of halide hosts, multiphonon

relaxation is thought to be strongly suppressed and therefore efficient UC luminescence can be obtained.

In this context, the present work discusses about some different rare-earth doped fluoride materials based on $NaREF_4$ and MF_2 host lattices, which possess physical properties of technological interest. It is well known, that for some of the cited applications, it is desirable to synthesize the above mentioned functional materials in the form of nanostructured films.

In this work, Metal Organic Chemical Vapor Deposition (MOCVD) approaches have been used to fabricate the fluoride phases of interest in form of thin films. MOCVD is an attractive technique to synthesize a wide number of materials ranging from metals to insulators, allowing the control over film composition, microstructure and morphology through a suitable choice of substrate, precursor and reactant, as well as deposition parameters.

It is important to underline that the success of an MOCVD process depends critically on the availability of volatile, thermally stable precursors. To this aim, an accurate knowledge of the physical properties and thermal behaviour of precursors is of fundamental relevance for the optimization of processes in the perspective of achieving uniform and reproducible films. The structural properties of the synthesized precursors have been investigated through FT-IR spectroscopy. In regard to thermal characterization, thermogravimetric analyses (TGA) have been carried out. The physico-chemical behaviour of the films depends on the film structural characteristics, such as crystalline structure of the deposited phases, chemical composition, uniformity and eventual interactions among substrate and overlayer. Deposited films have been studied by X-ray diffraction (XRD) to determine their structure and cristallinity. Additional information regarding the epitaxial growth of thin films has been obtained using TEM (Transmission Electron Microscopy) and pole figure analysis. The film composition and purity have been assessed by energy dispersive (EDX) and wavelength dispersive (WDX) x-ray analyses. Morphological properties of thin films have been investigated through field emission scanning electron microscopy (FE-SEM).

In summary, the research activity has been carried out as in the following:

- Systematic study of precursors suitable for the MOCVD growth of $BaMF_4$ (M = Mg and Ni) films, and in particular rationalization of the relationship between precursor nature and film properties in regard to NiO films;
- Synthesis and characterization of barium, strontium and magnesium precursors;
- Synthesis and characterization of new heterobimetallic complexes sodium-gadolinium and sodium-yttrium that may act as single source precursors;
- Synthesis of undoped and Mn-doped $BaMgF_4$ thin films through Conventional and Liquid Injection MOCVD processes;
- MOCVD growth of rare earth doped alkaline earth fluoride thin films;
- Accurate analysis of the composition and structural/morphological properties of deposited films;
- Characterization of the functional properties of the synthesized materials.

Chapter 1 : Multifunctional fluoride materials

1.1 Ferroelectric and multiferroic materials

Ferroelectric materials offer a wide range of useful properties. These include ferroelectric hysteresis (used in nonvolatile memories), high permittivities (used in capacitors), high piezoelectric effects (used in sensors, actuators and resonant wave devices such as radio-frequency filters), high pyroelectric coefficients (used in infra-red detectors), strong electro-optic effects (used in optical switches) and anomalous temperature coefficients of resistivity (used in electric-motor overload-protection circuits).[1]

The piezoelectric effect describes the relation between a mechanical stress and an electrical voltage in solids. One of the unique characteristics of the piezoelectric effect is that it is reversible, meaning that materials exhibiting the direct piezoelectric effect (the generation of electricity when stress is applied) also exhibit the converse piezoelectric effect (the generation of stress when an electric field is applied). A ferroelectric material has a permanent electric dipole, and is named in analogy to a ferromagnetic material (e.g. Fe) that has a permanent magnetic dipole. A ferroelectric material exhibits a spontaneous electric polarization that can be reversed or reoriented by application of an electric field. Ferroelectricity ceases in a given material above a characteristic temperature, called its Curie temperature, because the heat agitates the dipoles sufficiently to overcome the forces that spontaneously align them. The barium titanate ($BaTiO_3$) is the most widely studied ferroelectric material. $BaTiO_3$ is a member of the perovskite family based on the mineral $CaTiO_3$, as predicted from fundamental crystal chemical principles described much earlier by Goldschmidt (1926).[2]

The perovskite ideal cubic structure does not exhibit ferroelectric effect, but the distorted tetragonal phase due to oxygen and titanium ions shifting to produce a spontaneous polarization yields a ferroelectric phase at room temperature. The solid can exist in five phases, listing from high

temperature to low temperature: hexagonal, cubic, tetragonal, orthorhombic, and rhombohedral crystal structure. All of the phases exhibit the ferroelectric effect except the cubic phase.

According to the original definition put forward by Hans Schmid,[3] multiferroic materials are those materials that combine at least two of the three ferroic orders, i.e. ferroelasticity, ferroelectricity and ferromagnetism. Traditionally, the term magnetoelectric effect is used to describe any form of cross-correlation between the magnetic and (di-)electric properties. In magnetoelectric materials, a magnetic field can induce an electrical polarization and, conversely, an electric field can induce a magnetization. It is important to point out that not necessarily a multiferroic material exhibits a linear magnetoelectric effect, and viceversa.

Due to the combination of magnetic and dielectric properties, with eventual cross-coupling between these properties, multiferroic materials have been intensively studied in view of their immense potential for device applications. These materials are considered as key components in the development of future technology, for example, in memories and read-write electronic devices.[4]

Few multiferroic compounds exist in nature, because of the difficulty to find simultaneously ferroelectric and ferromagnetic or antiferromagnetic properties in the same material. Several perovskite materials, such as $BiFeO_3$, $BiMnO_3$, $YMnO_3$, have been reported as multiferroic materials.[5-8]

Compared to oxides, there are no many fluoride-based multiferroic materials, with the coexistence of ferroelectricity and room temperature ferromagnetism, since they usually adopt high symmetry (centrosimmetric space group) that doesn't support ferroelectricity.[9] Among the few known ferroelectric fluoride crystals,[10,11] the barium fluoride $BaMF_4$ (M=Mg,Mn,Co,Ni,Zn) has recently caught substantial attention in view of its interesting, multifunctional properties.

1.1.1 $BaMF_4$: structure and properties

The isostructural $BaMF_4$ compounds crystallize in a base-centered orthorhombic structure with the C*mc2₁* polar space group. In this structure the M cations are octahedrally coordinated by the

fluorine anions and four of the fluorine ions of these octahedra are shared with neighbouring octahedra while the barium ions are ordered in BaF_8 polyhedra (Fig 1.1.1.1).[12]

The structure is polar along the c direction, and ferroelectric switching has been demonstrated for M=Ni, Co, Zn and Mg, but not for M=Mn and Fe.[12]

The origin of ferroelectricity is of fundamental interest, since $BaMF_4$ does not contain any ions that are usually considered to be "ferroelectrically active," such as empty *d*-shell cations (like Ti^{4+} or Nb^{5+}) or lone-pair active cations such as Bi^{3+} or Pb^{2+}.[13,14]

This indicates that the ferroelectricity in these systems is of different origin with respect to conventional oxide perovskite ferroelectrics, such as $BaTiO_3$ or $PbTiO_3$, where ferroelectricity is caused by charge transfer between cations and anions; hence, the ferroelectricity in $BaMF_4$ is solely due to geometrical effects.

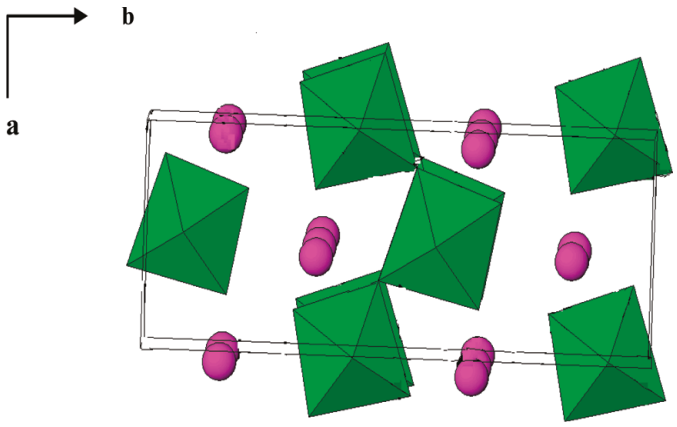

Fig. 1.1.1.1 Unit cells of $BaMF_4$. Green octahedra indicate the MF_6 unit, and pink spheres are Ba atoms.[9]

The $BaMgF_4$ compound (BMF) belongs to this class of emerging fluoride ferroelectrics and represents one of the most studied systems in view of its multifunctional properties. It exhibits room temperature ferroelectric and diamagnetic properties, where the electric polarization in the system is solely due to geometrical distortion and is directed along the c-axis. In particular, both rotational motions of the MgF_6 octahedra and displacements of the Ba cations due to relative ionic size effects and geometrical constraints result in the spontaneous ferroelectric polarization.[12]

The origin of ferroelectricity in this class of material is related to the distortion of polyhedra.

Although the pure compound doesn't exhibit ferromagnetism, it has been recently demonstrated that this property can be induced by substitutional doping of Mg by a transitional metal ion, e.g. Mn,[9,15,16] thus realizing a multiferroic material, where ferro/antiferroelectric and ferro/antiferromagnetic properties coexist simultaneously exhibiting electromagnetic coupling. The choice of manganese is due to its ionic radii in octahedral coordination (0.83 Å) comparable with the ionic radii of octahedrally coordinated Mg^{2+} (0.72 Å)[17] in BMF.

In addition, the ferroelectric fluoride $BaMgF_4$ has attracted a great attention also due to its wide transparency range and good nonlinear optical properties.[18] Thus BMF crystals have been studied as new solid-state laser materials in the UV region.[19-24]

The third order non linear refractive index of bulk BMF was found to be large and an order of magnitude larger than that of $LiNbO_3$.[25] These properties make BMF a good candidate for integrated optical devices.

On the other hand, it is rarely concerned about the luminescent properties of BMF compounds doped with rare earth ions.

It has been recently demonstrated that lanthanide doped polycrystalline BMF nanoparticles can give rise to both down-conversion luminescence for doped Eu^{3+} or Tb^{3+} and up-conversion luminescence for Yb^{3+}/Er^{3+} (Tm^{3+}).[26-28]

1.2 Lanthanide-doped fluoride materials for upconversion luminescence

Upconversion emission (UC) is a process in which two or more low energy photons are converted to higher energy radiation. An example is the conversion of infrared light to visible light. This process was first observed by Auzel in 1966.[29]

Generally, the UC process is observed in lanthanide or transition metal generally embedded in a host matrix to fabricate upconversion phosphors.

Specifically, lanthanide-doped materials are considered as the most efficient photon upconversion systems. The lanthanides, which are characterized by the progressive filling of the 4f orbitals, are a family of 14 chemically similar elements, commencing with cerium (Ce) and ending with lutetium (Lu). Lanthanide ions typically exist in their most stable oxidation state as trivalent ions (Ln^{3+}) and have a $4f^n5s^25p^6$ electron configuration ($1 < n < 14$).

The unique luminescent characteristics of lanthanide dopants arise from their electronic transitions. Owing to the dipole-forbidden nature of the 4f–4f transition, these lanthanides exhibit very long decay times in the order of microseconds, which increase the probability of sequential excitations and excited state energy transfer of the lanthanide ions.[30]

The presence of multiple metastable levels in lanthanide ions makes them a preferred dopant for UC inorganic phosphors. A typical inorganic UC phosphor contains a crystalline host material and a dopant (emitter) added in low concentration. The dopant acts as luminescent centers while the host provides a crystalline matrix to bring these centers into optimal positions.

The choice of host matrix has a strong influence on the upconversion process, since the distance between the dopant Ln^{3+} ions, their relative spatial position, their coordination numbers, and the type of anions surrounding the dopant are determined by the host lattice. Ideal host materials need to be thermally stable and have low lattice phonon energies required to minimize non-radiative losses and maximize the radiative emission. Generally, halides exhibit low phonon energies but the hygroscopic nature of halides limits their use, whereas oxides are very stable but their phonon energies are relatively higher than 500 cm^{-1}.[31,32]

Fluorides usually exhibit low phonon energies (~300-350 cm^{-1}) and high chemical stability, and thus are regarded as the most promising host materials.

Er^{3+} and Tm^{3+} ions are usually chosen as emitters to give rise to efficient UC emission.[33]

In most UC materials, the Er^{3+} concentration does not exceed 3%, because of the increased probability of cross-relaxation events over this concentration. At this low concentration, Er^{3+} ion cannot absorb the excitation light effectively, which results in low UC efficiency.

In order to increase the absorption in lanthanide-doped phosphors, a sensitizer with a sufficient absorption cross section in the NIR region is usually co-doped along with the emitting ion (see following paragraph). Trivalent ytterbium (Yb^{3+}) is the most commonly used sensitizer for UC phosphors. This is due to its larger absorption cross-section than any other lanthanide ions; moreover, the absorption band is located at 980 nm.

A typical system is represented by Er^{3+} used as emitter and Yb^{3+} as sensitizer. The energy level diagram and the electron transitions giving rise to upconversion for this system are schematized in Fig 1.2.1.

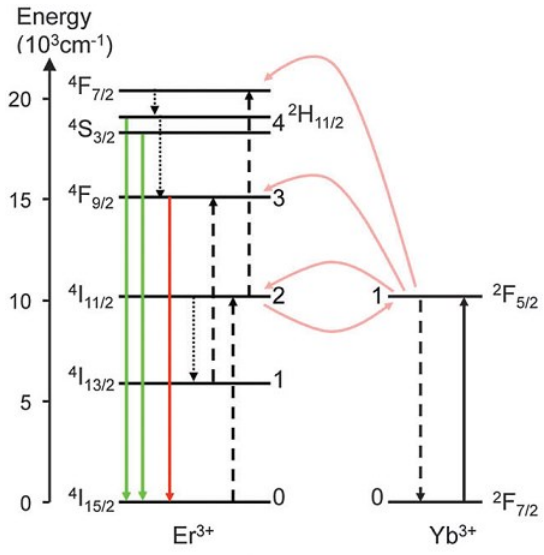

Fig. 1.2.1 Energy levels of Yb^{3+} and Er^{3+} ions relevant to the energy transfer upconversion process. Initial absorption is indicated by the black solid line narrow, the subsequent energy transfer processes by the dashed arrows, the non-radiative relaxations by dotted arrows and the final upconverted luminescence by the green and red arrows.[34]

In the Er^{3+} ion the energy difference between the $^4I_{11/2}$ and $^4I_{15/2}$ states (10350 cm^{-1}) is similar to that between the $^4F_{7/2}$ and $^4I_{11/2}$ states (10370 cm^{-1}). In addition, the energy difference between the $^4F_{9/2}$ and $^4I_{13/2}$ states is in the same region; hence, the Er^{3+} ion can be excited to a higher energy level by at least three possible transitions by absorbing IR photons of the same energy, which gives visible

upconverted green and red emissions. Yb^{3+} has an extremely simple energy level scheme with only one excited 4f level of $^2F_{5/2}$. In addition, the $^2F_{7/2}$ - $^2F_{5/2}$ transition of Yb^{3+} is well resonant with the transition energy between the $^4I_{11/2}$ and $^4I_{15/2}$ states and also the $^4F_{7/2}$ and $^4I_{11/2}$ states of Er^{3+} ions, thus facilitating the energy transfer from Yb^{3+} to Er^{3+} ions.

Usually, a higher concentration of Yb^{3+} sensitizer is doped in UC materials (18–20%). Yb^{3+} is also a standard sensitizer for Tm^{3+} and Ho^{3+} ions.

References

[1] R. Whatmore, *Springer*, 2007.

[2] V. M. Goldschmidt, *Naturwissenschaften*, 1926, **14**, 477.

[3] H. Schmid, *Multi-ferroic magnetoelectrics, Ferroelectrics*, 1994, **162**, 317.

[4] M. Bibes and A. Barthelemy, *Nature Materials*, 2008, **7**, 425-426.

[5] J. B. Neaton, C. Ederer, U.V. Waghmare, N. A. Spaldin and K. M. Rabe, *Phys. Rev. B*, 2005, **71**, 014113.

[6] N. A. Hill and K. M. Rabe, *Phys. Rev. B*, 1999, **59**, 8759.

[7] T. Lottermoser, T. Lonkai, U. Amann, D. Hohlwein, J. Ihringer and M. Fiebig, *Nature*, 2004, **430**, 541.

[8] T. Kimura, T. Goto, H. Shintani, K. Ishizaka, T. Arima and Y. Tokura, *Nature*, 2003, **426**, 55.

[9] F. N. Sayed, B. P. Mandal, O. D. Jayakumar, A. Arya, R. M. Kadam, A. Dixit, R. Naik and A. K. Tyagi, *Inorg. Chem*., 2011, **50**, 11765–11772.

[10] M. Eibschutz, H. J. Guggenheim, S. H. Wemple, I. Camlibel and M. DiDomenico, *Phys. Lett.*, 1969, **29A**, 409.

[11] F. N. Sayed, B. P. Mandal, O. D. Jayakumar and A. K. Tyagi, *AIP Advances*, 2013, **3**, 072133.

[12] C. Ederer and N.A. Spaldin, *Phys. Rev. B*, 2006, **74**, 024102.

[13] N. A. Hill, *J. Phys. Chem. B***,** 2000, **104**, 6694.

[14] R. Seshadri and N. A. Hill, *Chem. Mater.,* 2001, **13**, 2892.

[15] M. Manikandan, A. Muthukumaran and C. Venkateswaran, *Journal of Magnetism and Magnetic Materials*, 2015, **393**, 40–45.

[16] M. Manikandan, A. Muthukumaran, C. Venkateswaran, *Solid State Physics*, 2014, **1**, 1516-1517.

[17] R.D. Shannon, *Acta Crystallogr. Sect. A*, 1976, **32**, 751-767.

[18] L. Mateos, M. O. Ramirez, I. Carrasco, P. Molina, J. F. Galisteo-Lopez, E. G. Villora, C. de las Heras, K. Shimamura, C. Lopez and L. E. Bausa, *Advanced Functional Materials*, 2014, **24**, 1509-1518.

[19] N. Kodama, T. Hoshino, M. Yamaga, N. Ishizawa, K. Shimamura and T. Fukuda, *Journal of Crystal Growth*, 2001, **229**, 492–496.

[20] A. Wu, Z. Wang, L. Su, D. Jiang, Y. Zou, J. Xu, J. Chen,Y. Ma, X. Chen and Z. Hu, *Optical Materials*, 2014, **38**, 238-241.

[21] X. Zhang, S. Liu, X. Chen and W. Luo, *Solid State Communications*, 2015, **205**, 33–38.

[22] T. E. Littleford, R. E. Jackson and S.D. Mark, *Phys. Status Solidi C*, 2013, **10**, 153-155.

[23] M. Trevisani, K. V. Ivanovskikh, M. O. Ramirez, P. Molina, E. G. Villora, K. Shimamura, L. E. Bausa and M. Bettinelli, *Journal of Luminescence*, 2014, **153**, 136-139.

[24] Y. Ma; J. Chen, Y. Zheng and X. Chen, *Applied Optics*, 2012, **51**, 5432-5437.

[25] J. Chen, X. Chen, A. Wu, H. Li, Y. Zheng, Y. Ma, L. Jiang and J. Xu, *App. Phys. Lett*., 2011, **98**, 191102.

[26] C-L. Pan, H-L. Liu, Y. Guo, S. Jing, H-F. Zhou and H. Wang, *Wuli Xuebao*, 2014, **63**, 154211/1-154211/5.

[27] Z-Y. Yan, B. Yan and L-P. Jia, *Materials Research Bulletin*, 2013, **48**, 4402–4405.

[28] Z-Y. Yan and B. Yan, *Photochemistry and Photobiology*, 2013, **89**, 1262-1268.

[29] F. Auzel, *Acad. Sci. Paris B*, 1966, **263**, 819–821.

[30] W.Yang, X. Li, D. Chi, H. Zhang and X. Liu, *Nanotechnology*, 2014, **25**, 482001.

[31] J. Ohwaki and Y. Wang, *Jpn. J. Appl. Phys.*, 1994, **33**, 334–337.

[32] F. Auzel, D. Pecile and D. Morin, *J. Electrochem. Soc.*, 1975, **122**, 101–107.

[33] F. Wang and X. Liu, *Chem. Soc. Rev.*, 2009, **38**, 976–989.

[34] W. Park, D. Lua and S. Ahna, *Chem. Soc. Rev.*, 2015, **44**, 2942.

Chapter 2: Development of MOCVD precursors

2.1 Background studies on alkaline earth precursors

In this work, the most critical issues related to thin film fabrication are discussed from different points of view, from the precursor choice to the substrate nature. Indeed, the success of the MOCVD technique relies upon the precursor nature, the deposition parameters and the specifical used substrate. In particular, the importance of precursor nature becomes crucial for the synthesis of multicomponent systems, such as $BaMF_4$, for which it is necessary to have suited Ba, M and F sources. For these reasons, before growing multicomponent systems, it is of fundamental importance a preliminary study on the precursor nature and its application to the growth of single phases, e.g. barium and magnesium in the case of $BaMgF_4$, in order to optimize all the factors that influence the film properties.

Thermally stable and volatile Ba, Mg and F precursors are needed for the growth of these films. Group II metal precursors have always represented a great challenge in the MOCVD process since they show severe drawbacks in terms of mass transport properties due to the large size (except for Mg) and to the strong polarity of the alkaline earth metal centre.[1] Wide efforts have been devoted to the search for thermally stable and volatile alkaline-earth metal precursors and problems associated with Ba, much more pronounced due to the larger ionic radius of this metal compared to the other alkaline earth metals, have been overcome with the "second-generation" precursors formed by fluorinated β-diketonate polyether adducts.[2]

Concerning the precursors required for the synthesis of $BaMgF_4$ thin films, the $Ba(hfa)_2$tetraglyme, and $Mg(hfa)_2(H_2O)_2$diglyme adducts (Hfa=1,1,1,5,5,5-hexafluoroacetylacetone; tetraglyme= 2,5,8,11,14-pentaoxapentadecane; diglyme= (bis(2-methoxyethyl)ether) have been applied as

metal/fluorine single sources, since previous studies have shown that these precursors act as efficient single sources for the deposition of BaF_2 and MgF_2 respectively.[3,4,5]

Hence, they were synthesized as previously reported, and applied to the growth of binary fluoride thin films, whose properties as host matrices have been investigated as well.

Due to the great interest in the SrF_2 phase as host matrix for UC luminescence, the Sr(hfa)$_2$tetraglyme precursor has been synthesized as well[3] and applied to the MOCVD growth of SrF_2 thin films.

2.1.1 Ba(hfa)$_2$·tetraglyme

The complex Ba(hfa)$_2$·tetraglyme has been synthesised through a one-pot reaction between $Ba(OH)_2 \cdot 8H_2O$ (2.674 g, 8.47 mmol) dispersed in a CH_2Cl_2 solution (35 ml), tetraglyme (1.570 g, 7.06 mmol) and Hhfa (2.94g, 14.13 mmol). The resulting mixture was refluxed under stirring for 1 h. The excess of barium hydroxide was filtered off and the product recovered from the CH_2Cl_2 solution, in which it is soluble. The product was purified using pentane to yield colourless crystals. The structural characterization of the present precursor has been performed by FT-IR analysis. The FT-IR spectrum of Ba(hfa)$_2$·tetraglyme (Fig. 2.1.1.1) does not show any band in the 3500–3600 cm^{-1} interval thus confirming the absence of water in the coordination sphere..

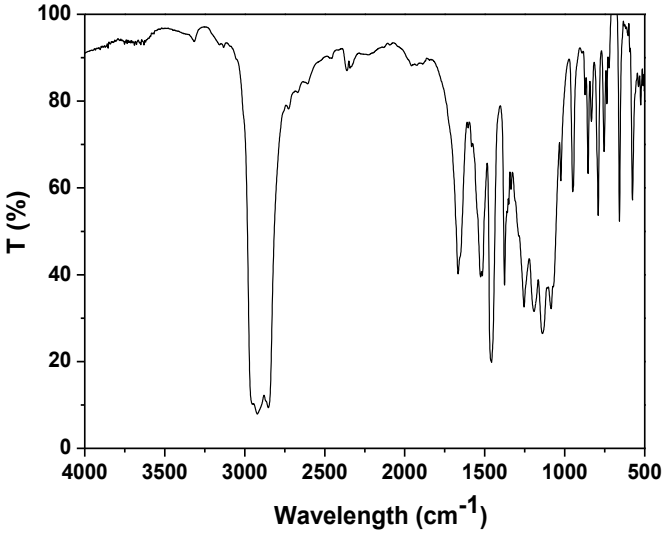

Fig. 2.1.1.1 FT-IR spectrum of Ba(hfa)$_2$·tetraglyme.

Peaks at 1658 cm^{-1} (C=O stretching vibrations) and at 1524 cm^{-1} (C=C stretching vibrations) are typical of the β-diketonate framework The other bands, observed in the range 1300–1100 cm^{-1}, represent the C–F stretchings of the hfa ligand. In addition, bands observed in the range 1100-700 cm^{-1} can be associated with glyme modes. Other features (at 2915, 1460 and 1377 cm^{-1}) are typical of the nujol used to prepare the mull.

The thermal behavior of the Ba adduct has been fully investigated by thermogravimetric analyses (TG) (Fig. 2.1.1.2). The $Ba(hfa)_2$·tetraglyme complex is thermally stable and the derivative curve of TG (DTG) consists of a single peak thus indicating that it evaporates quantitatively in the 180–310 °C range, with a residue left at 350 °C of 8 %.

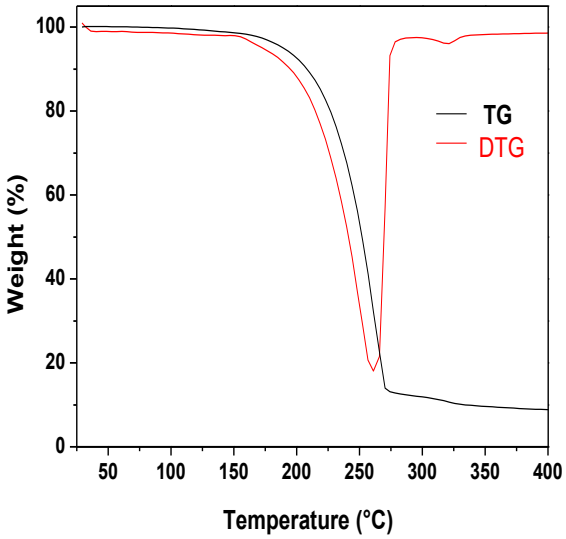

Fig 2.1.1.2 TG and DTG profiles of $Ba(hfa)_2$·tetraglyme under N_2 flow at atmospheric pressure in the 30–400 °C temperature range.

From thermal analysis it can be concluded that the $Ba(hfa)_2$·tetraglyme adduct shows a clean vaporization with a low residue as requested for MOCVD applications.

2.1.2 $Mg(hfa)_2 \cdot (diglyme)_2 \cdot (H_2O)_2$

Herein, the synthesis and transport characteristics of the magnesium precursor of formula $Mg(hfa)_2 \cdot 2H_2O \cdot 2diglyme$ [Hhfa= 1,1,1,5,5,5-hexafluoro-2,4-pentanedione, and diglyme = (bis(2-methoxyethyl)ether)], are reported. The Mg adduct was prepared using a procedure analogous to the one described for the Ba adduct from 2.041 g (4.21 mmol) of magnesium basic carbonate source $(MgCO_3)_4 \cdot Mg(OH)_2 \cdot 5H_2O$, 2.940 g (14.13 mmol) of Hhfa and 1.895g (14.13 mmol) of diglyme reagents. The procedure yields reproducibly, under open bench manipulations, a clean source adduct. A slight excess of Mg carbonate favors the isolation of the product since the excess remains insoluble and can be easily filtered off. The adduct is very soluble in common organic solvents such as ethanol, chloroform, acetone, and pentane and slightly soluble in cyclohexane. It has a very low melting point and evaporates quantitatively at low temperature under vacuum and even under atmospheric pressure despite the presence of coordinated water. The FT-IR transmittance spectrum of the $Mg(hfa)_2 \cdot 2H_2O \cdot 2diglyme$ adduct (Fig. 2.1.2.1) shows a broad envelope with two bumps in the 3292 and 3487 cm^{-1} range due to the OH asymmetric and symmetric stretching modes of coordinated water.[6] The carbonyl stretching frequency appears at 1657 cm^{-1}, whereas peaks at 1558 and 1534 cm^{-1} are associated with C=O stretching and with C=C stretching vibrations, respectively.[7] The broadband observed in the 1000-1300 cm^{-1} range may be associated with absorptions due to the polyether C-O bending and/or stretching overlapped with the C-F stretching. In addition, bands at 1015, 861, and 837 cm^{-1} can be associated with glyme modes. The C-H glyme stretching modes, lying in the 2800-3000 cm^{-1} range, overlap with nujol features. In fact, the nujol shows peaks at 2923, 1461, and 1377 cm^{-1}.

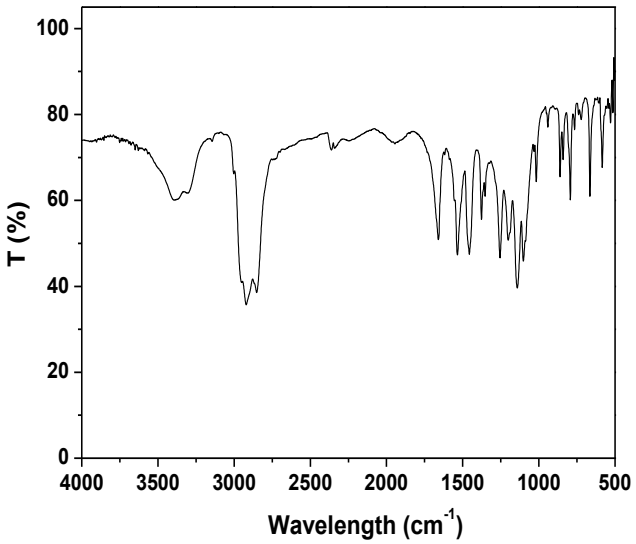

Fig 2.1.2.1 FT-IR spectrum of $Mg(hfa)_2 \cdot 2H_2O \cdot 2diglyme$.

Thermal behavior of the $Mg(hfa)_2 \cdot 2H_2O \cdot 2diglyme$ adduct has been studied by thermal gravimetric analysis (TG) experiments. Atmospheric pressure TG analysis of the $Mg(hfa)_2 \cdot 2H_2O \cdot 2diglyme$ adduct shows two regions mass loss in the temperature range 40-100 °C and 110-210 °C (Fig. 2.1.2.2). The lower-temperature process, associated with a minor mass loss (∼5%) is well-tuned with the following equation

$$Mg(hfa)_2 \cdot 2H_2O \cdot 2diglyme \rightarrow Mg(hfa)_2 \cdot 2diglyme + 2H_2O$$

The remaining 95% mass is lost quantitatively in the second step, almost without residue (<1%) left. Therefore, the lower temperature process leaves an anhydrous, liquid adduct, which evaporates intact afterward. Therefore the present Mg adduct, despite the presence of water molecules in the coordination sphere, cleanly self-generates a liquid anhydrous source that represents a single source of Mg and F elements for MOCVD processes of magnesium fluoride phases.

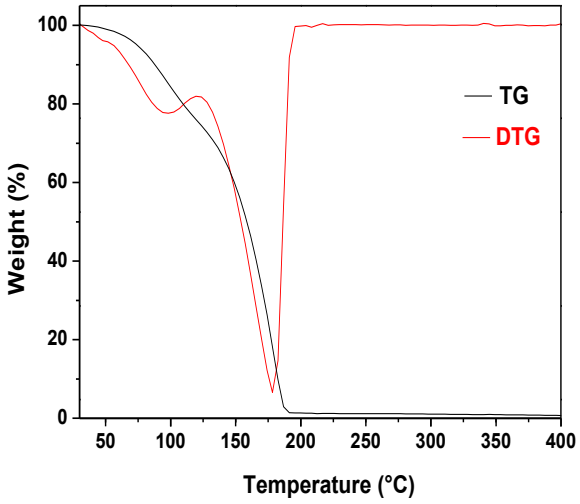

Fig. 2.1.2.2 TG and TG profiles of $Mg(hfa)_2 \cdot 2H_2O \cdot 2$diglyme under N_2 flow at atmospheric pressure in the 30–400 °C temperature range.

2.1.3 $Sr(hfa)_2 \cdot$tetraglyme

The present strontium complex was synthesized following the same scheme of the Ba and Mg precursors. The one-pot reaction between strontium hydroxide $Sr(OH)_2 \cdot 8H_2O$ (2.441 g, 9.18 mmol) dispersed in a CH_2Cl_2 solution (35 ml), tetraglyme (1.570 g, 7.06 mmol) and Hhfa (2.940g, 14.13 mmol) yielded the anhydrous, air-stable $Sr(hfa)_2 \cdot$tetraglyme adduct. The FT-IR spectrum is reported in figure 2.1.3.1. The absence of any band in the 3500–3600 cm^{-1} interval is indicative of a water-free complex. The carbonyl stretching frequency appears at 1665 cm^{-1}, while peak at 1524 cm^{-1} is associated with C=C stretching. The other bands, observed at 1300–1100 cm^{-1}, represent C-O bending and/or stretching of the polyether ligand overlapped with the C-F stretching. In addition, the spectrum shows characteristic peaks between 750 and 1050 cm^{-1} which may be considered as fingerprints of the glyme coordination to the strontium hexafluoroacetylacetonate moiety. The peaks at 2922, 1458 and 1376 cm^{-1} are assigned to the nujol.

.

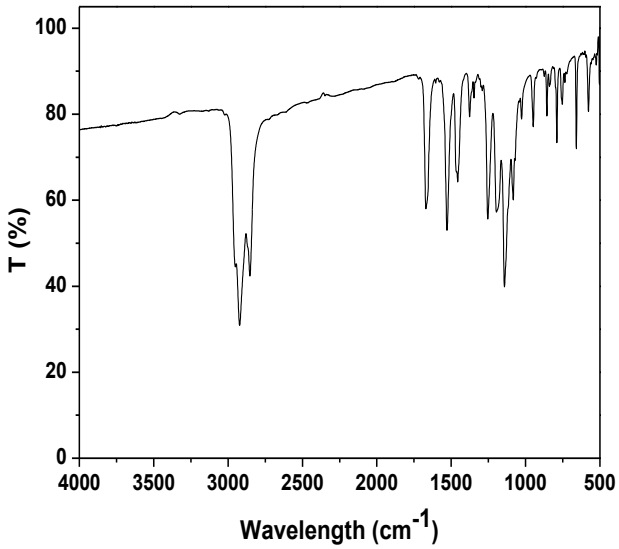

Fig. 2.1.3.1 FT-IR spectrum of $Sr(hfa)_2$·tetraglyme.

The thermal behavior of the present Sr precursor has been fully investigated by thermogravimetric analyses (TG) (Fig. 2.1.3.2). A singular sublimation step is observed. The sublimation process takes place in the temperature range 160-300 °C (residue=3% to 350 °C).

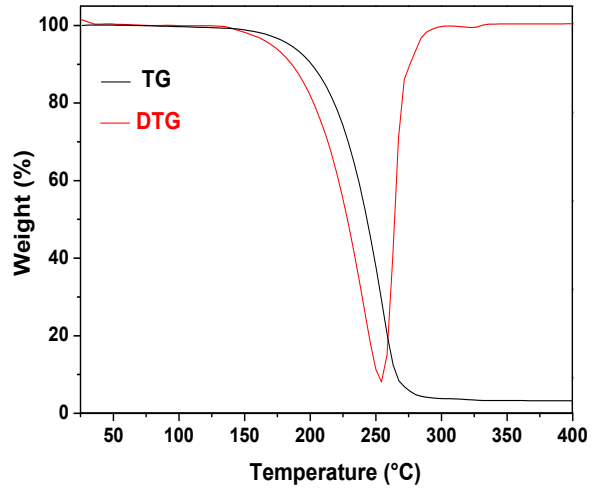

Fig 2.1.3.2 TG and DTG profiles of $Sr(hfa)_2$·tetraglyme under N_2 flow at atmospheric pressure in the 30–400 ˚C temperature range.

The IR and TG data of the raw and sublimed adduct are in very good agreement with the characterization reported in literature.[3]

2.2 Applications of Ni precursors to NiO films growth

In this thesis, a Metal Organic Chemical Vapor Deposition approach is used to the fabrication of $BaNiF_4$ phases (par. 3.1). To this aim, fluorinated β-diketonate Ni(II) complexes may be envisaged as Ni-F single sources for the fabrication of Ni-F based phases as thin films.

In addition, a reproducible MOCVD process requires thermally stable and volatile enough single sources to provide molecular integrity during the mass transport. Low-melting architectures are also desired to allow constant evaporation from the liquid phase for long time intervals.

To date, β-diketonate complexes with 2,2,6,6-tetramethyl-3,5-heptanedione (Hthmd) and acetylacetone (Hacac) ligands have been widely used as MOCVD sources for NiO films.[8] These precursors suffer, however, from some drawbacks associated with their high melting points [228°C for $Ni(tmhd)_2$[9] and 240 °C for $Ni(acac)_2$[10]] and with the presence of H_2O molecules in the coordination sphere. In addition, they do not have F atoms in their structures, thus they can not be applied as fluorine sources to the synthesis of nickel fluoride phases.

Therefore, two fluorinated precursors have been tested: the $Ni(hfa)_2$tmeda and the $Ni(tta)_2$tmeda[11] [(H-hfa =1,1,1,5,5,5-hexafluoro-2,4-pentandione, Htta = 2-thenoyltrifluoroacetone, tmeda = N,N,N',N'-tetramethylethylendiamine)]. In particular, the synthesis and characterization of the transport properties of both precursors are reported in the following.

A comprehensive systematic study for the MOCVD deposition of NiO films relating the use of the two precursors on the structural, morphological and functional properties of the deposited layers has been assessed. The correlation between the nature of the nickel β-diketonate precursor and the properties of the NiO film has been addressed.

The Nickel oxide (NiO) is among the most widely investigated transition metal oxides (TMOs), and its properties and applications deserve a more detailed description. Nickel oxide actually represents a model compound for TMOs with the sodium chloride structure.[12] It exhibits only a very small

deviation from the ideal stoichiometry, at difference with the cobalt oxide (CoO) and especially the wüstite iron oxide (FeO) phase.

NiO has also drawn much attention due to its utilization for several applications, such as gas sensors,[13,14] catalysts,[15,16] and electrochromic devices.[17-20] Other applications regard its use as transparent conducting oxide (TCO) films. TCO films such as indium oxide, tin oxide and zinc oxide, are of practical use as transparent electrodes and window coatings, but they are all n-type semiconductors. A desirable hole injecting contact would be based on the injection into the valence band of a p-type semiconducting oxide. NiO films is one of the potential candidates for p-type TCO. Nickel oxide is known to become a p-type semiconductor when its composition deviates from stoichiometry or when monovalent atoms, such as Li^+,[21,22] are added, while pure stoichiometric NiO is an insulator with high resistivity ($\rho > 10^{13}$ Ω·cm) at room temperature. Due to their electric properties, p-type semiconducting nickel oxide films have been used as efficient-enhancing anode interfacial layers in polymer bulk-heterojunction,[23-25] and dye-sensitized solar cell[21,26-29] and as hole transporting[30] or as electron blocking[31] layer in light-emitting devices.

Thin films of NiO, due to their antiferromagnetic properties with a Néel point (T_N) of 523 K, are also very useful as the antiferromagnetic layer of spin-valve superlattice films. Pure nickel oxide exhibits antiferromagnetic ordering, with planes of opposite spins being repeated in alternating order along the [111] direction. Below the Néel temperature, the magnetic ordering in NiO is accompanied by a slight rhombohedral distortion (at 20°C, a =2.9518 Å, α=60.42°).[32] Magnon excitations in pure NiO nanoparticles and single crystals have been successfully studied by Raman spectroscopy:[33-35] the strong magnetic Raman response is caused by the Ni-O superexchange mechanism.

2.2.1 Impact of precursors and substrate on NiO film properties

Two different nickel sources have been synthesized and applied: $Ni(tta)_2$•tmeda and $Ni(hfa)_2$•tmeda. The synthesis and characterization of $Ni(tta)_2$•tmeda have been reported elsewhere.[11] Herein, it is presented a new strategy for the synthesis of $Ni(hfa)_2$•tmeda, whose synthesis had been previously reported.[36] The volatile and thermally stable $Ni(hfa)_2$•tmeda complex was prepared by the reaction of $Ni(CH_3COO)_2$•$4H_2O$ (1.932 g, 7.763 mmol) suspended in dicloromethane (50 ml) with tmeda (0.821 g, 7.065 mmol) and H-hfa (2.940 g, 14.130 mmol). The mixture was refluxed, under stirring, for 1 h. The solution was collected by filtration under vacuum and the excess of $Ni(CH_3COO)_2$•$4H_2O$ was filtered off. Green-emerald crystals were obtained upon evaporation of the solvent and were washed two times in pentane. Upon filtration, green emerald crystals were recovered. The reaction yield was 88 %. The melting point of the crude product was 103-107 °C/760 Torr. The thermal behavior of the present $Ni(tta)_2$•tmeda and $Ni(hfa)_2$•tmeda precursors has been investigated by thermogravimetric (TG) analyses at atmospheric pressure in a purified nitrogen flow (Fig. 2.2.1.1). The thermogravimetric first derivative (DTG) of $Ni(tta)_2$•tmeda consists of a single peak, thus indicating that the precursor evaporates quantitatively in the 200-330°C range, with a residue left at 350°C lower than 2%. Same behaviour can be observed for $Ni(hfa)_2$•tmeda whose evaporation occurs in the temperature range 120-200 °C, with a residue left of about 2% at 350 °C. It can be concluded that both $Ni(tta)_2$•tmeda and $Ni(hfa)_2$•tmeda precursors show a clean vaporization with a low residue, as required for MOCVD applications.

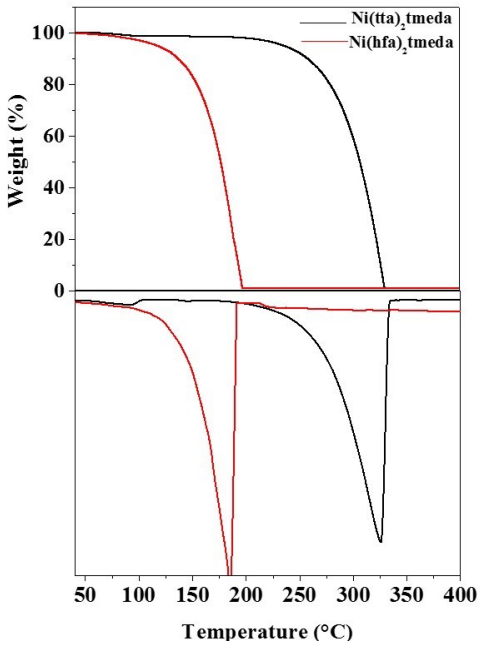

Fig. 2.2.1.1 TG and DTG profiles of Ni(hfa)$_2$•tmeda and Ni(tta)$_2$•tmeda complexes under N_2 flow at atmospheric pressure in the temperature range 30-400°C.

In figure 2.2.1.2, the differential scanning calorimetry (DSC) curves of the Ni(tta)$_2$•tmeda and Ni(hfa)$_2$•tmeda are reported. The DSC scans show evidence of the endothermic peaks due to melting at 151.3 °C and 106.7 °C respectively for Ni(tta)$_2$•tmeda and Ni(hfa)$_2$•tmeda. Both precursors evaporate from melts in the temperature ranges 300-330 °C and 125-195 °C, respectively.

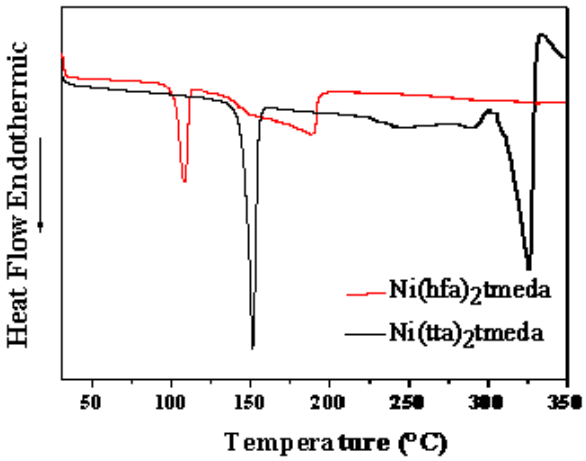

Fig. 2.2.1.2 DSC curves of Ni(hfa)$_2$•tmeda and Ni(tta)$_2$•tmeda complexes under N_2 flow.

NiO films were prepared in a reduced-pressure, horizontal, hot-wall MOCVD reactor from the $Ni(tta)_2$•tmeda and $Ni(hfa)_2$•tmeda sources contained in a resistively heated alumina boat.

Quartz and $LaAlO_3$ (001) substrates were used for the depositions. In this study, the precursor evaporation temperature was kept at 170 °C for $Ni(tta)_2$•tmeda and 90°C for $Ni(hfa)_2$•tmeda, whereas the reactor temperature was kept in the 350-550 °C range. Ar (150 standard cubic centimetres per min, sccm) and O_2 (50, 200 or 600 sccm) flows were used as carrier and reaction gases, respectively. Depositions were carried out for 60 min, yielding films of thickness in the range 170-250 nm depending on the deposition temperature and precursor nature. The total pressure in the reactor was about 2-6 Torr.

Quartz and $LaAlO_3$ (001) single crystal substrates have been chosen in view of specific applications. In particular, quartz has been used to test the optical properties, while the $LaAlO_3$ substrate is interesting to test the antiferromagnetic properties, since a very important issue in the fabrication of magnetic thin films is to find a substrate with a good lattice match vs. the growing film. The structure of films, as determined by XRD, is summarised for deposition on quartz substrates in figure 2.2.1.3.

Specifically, figures 2.2.1.3a and 2.2.1.3b show the XRD patterns of NiO films deposited on quartz substrates in the temperature range 350-550°C with an oxygen flow of 200 sccm from the $Ni(tta)_2$•tmeda and $Ni(hfa)_2$•tmeda precursors, respectively. For both the precursors, 350°C yields amorphous NiO films, while at higher temperatures of 450°C and 550°C, the films are polycrystalline, as inferred by the 2θ peaks at 37.30, 43.35 and 62.90° corresponding to the 111, 200 and 220 reflections, respectively. Note that only the reflection with hkl all odd or all even are observed due to the face-centered cubic lattice. In addition, the observed intensities do not always match those found for the polycrystalline powder as reported in the ICDD N. 47-1049. In particular, the I(200)/I(111) ratio (Figure 2.2.1.3c) and the full width at half maximum, FWHM, of the 200 peak, (Figure 2.2.1.3d) as a function of temperature and precursor type, indicate that the

Ni(tta)$_2$•tmeda at 550°C results in NiO films with a slight preferential orientation along the <001> direction.

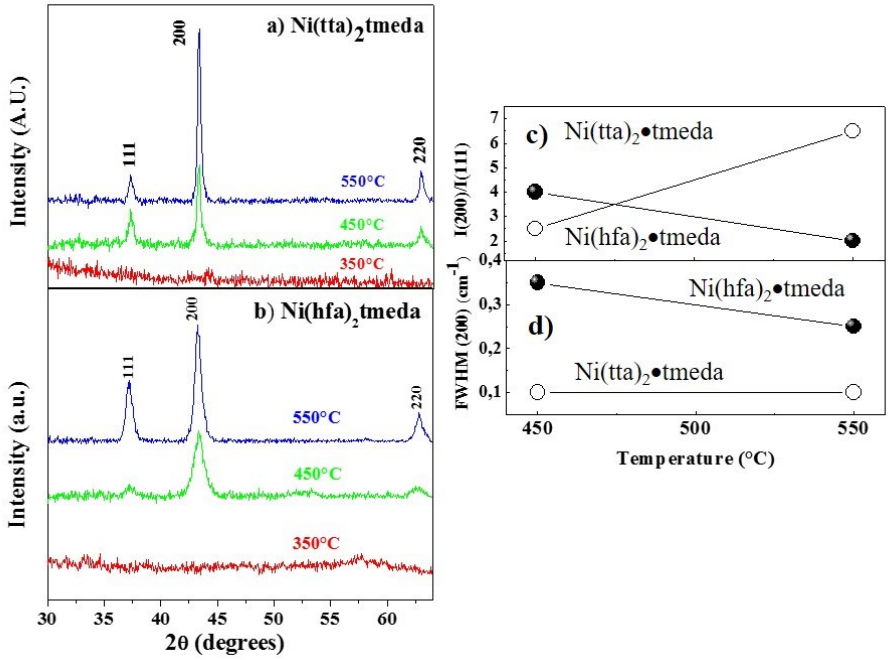

Fig. 2.2.1.3 X-Ray diffraction patterns of NiO films grown on quartz substrate at various temperature using the precursors (a) Ni(tta)$_2$•tmeda and (b) Ni(hfa)$_2$tmeda. (c) The evolution of the I(200)/I111) ratio and FWHM (200) as a function of temperature and precursor type is also shown.

Therefore, considering that XRD data indicate 550°C as the temperature condition to produce NiO films of better crystallinity, the unit cell parameter a has been extrapolated for films grown under these conditions from the two precursors following the diagram reported in figure 2.2.1.4. The extrapolated a-axis value of films grown from the precursor Ni(tta)$_2$•tmeda is 4.1750 Å. On the other hand, the a-axis parameter of films grown from the Ni(hfa)$_2$•tmeda is 4.1883 Å. The axis of the films grown from the Ni(tta)$_2$•tmeda, that compares well with the theoretical one of 4.17710 Å for the bulk NiO phase, indicates that these films are of good quality and stoichiometric compared to the bulk system.

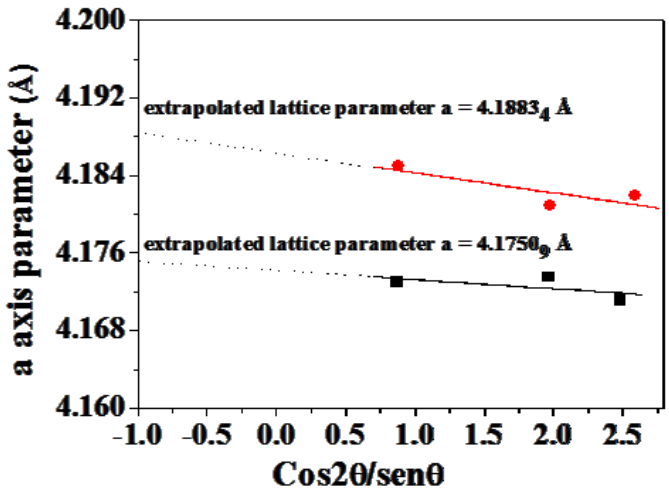

Fig. 2.2.1.4 Diagram for extrapolation of a-axis parameter of NiO phase. Red points refer to the NiO film obtained from Ni(hfa)$_2$•tmeda precursor, black points refer to the NiO film obtained from Ni(tta)$_2$•tmeda.

Therefore, NiO films have been grown on LAO (001) substrate under the optimized conditions obtained for depositions on quartz from the Ni(tta)$_2$•tmeda. The LAO substrate has been chosen to have a good lattice match, because if the lattices are well suited for one another the surface of a thin film appears smooth and flawless. If the spacing between atoms in the substrate is too different from that of the overlying film, however, then the film may exhibit wrinkling, clumping, or other defects and these surface characteristics may affect the magnetic properties. The LAO substrate has a perovskite structure, whose unit cell can be described as pseudo-cubic with a lattice constant aps = 3.792 Å, thus a mismatch of 10.6 % occurs for the NiO/LAO system. Figure 2.2.1.5 presents the XRD diffraction pattern of the sample deposited on LAO (001) at 550 °C and exhibits only the NiO 002 and 004 reflections at 2ϑ=43.30° and 95.35° in addition to the peaks at 2θ = 23.45°, 2θ = 48.15° and 2θ = 75.30° associated with the LAO 001, 002 and 003 reflections, respectively. Therefore, the NiO films grown on LAO (001) are purely <001> oriented. The grains dispersion has been investigated by measuring the rocking curve of the 002 reflection at 43.30° (Figure 2.2.1.5b). The full width at half maximum (FWHM) value of 0.94° indicates a good out-of-plane alignment of NiO films. The in-plane-alignment has been studied by recording the (111) pole figure (2θ = 37.25°) of NiO films (inset in Figure 2.2.15a). The pole figure shows four poles observed at Ψ =

54° every 90° degrees of ϕ, as expected for a cubic symmetry. In addition, the in-plane relationship of NiO films relative to the underlying LAO substrate has been obtained from Φ-scans of the NiO/LAO system (Figure 2.2.1.5c). Φ-scans have been recorded using as poles the NiO 111 reflection (2θ = 37.25°) and the LAO 111 reflection (2θ = 41.20°) at Ψ tilt angles of 54°. The four peaks from the NiO (111) planes are coincident with the (111) LAO Φ positions. This clearly demonstrates that a cube-on-cube growth is observed for the NiO on LAO substrate, thus the [100] and [010] axis directions are aligned for the film and the substrate (i.e. NiO <100>‖LAO <100>).

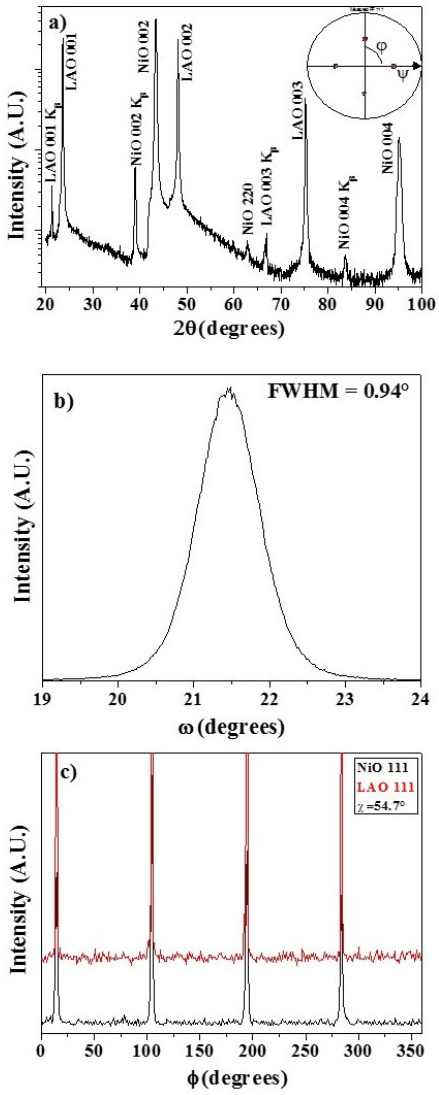

Fig. 2.2.1.5 a) XRD pattern of a film deposited on LAO (001) substrate at 550°C using the Ni(tta)$_2$•tmeda precursor; the inset reports the 111 pole figure (2ϑ= 37.25°) of the NiO film; b) rocking curve of 002 reflection of the epitaxial NiO film; c) Φ-scans using the 111 reflections as poles for the NiO and $LaAlO_3$ substrate.

These findings may be compared with the studies on heteroepitaxial growth of NiO on AlGaN.[37-39] In this case, due to the hexagonal structure of the substrate, an epitaxial growth of the {111} NiO planes on the (0001) substrate plane occurred. The study of the structural properties of the NiO films is corroborated by Raman measurements. Raman spectroscopy has been used as a non-nondestructive investigation of the structure and stoichiometry of NiO films, since NiO electronic structure, captured in its Raman spectrum, clearly evolves with its stoichiometry, quality and antiferromagnetic properties. The vibrational bands corresponding to the one-phonon (1P) longitudinal optical (LO) (at ~570 cm^{-1}) modes, the two-phonon (2P) mode 2TO (~870 cm^{-1}) and 2LO (at ~1100 cm^{-1}) modes, and the band due to a two-magnon (2M) scattering at ~1490 cm^{-1} are observed (Figure 2.2.1.6). The 1P broad band is a disorder-induced band that originates by Ni vacancies and its intensity has been related[40] to the film quality, i.e., the lower the intensity, the better the film quality, because of a lower density of Ni-vacancies and, consequently, a better stoichiometry. The intensity of the 1P band measured for films of comparable thickness under the same Raman acquisition conditions (measured also the same day) plotted in figure 2.2.1.6e shows that the film quality (in terms of Ni-vacancies) is significantly better for the $Ni(tta)_2$•tmeda precursor. Another important difference between films grown from the two precursors comes out by analyzing the region around 1490 cm^{-1} of the characteristic two-magnon (2M) scattering band; its presence for the films from $Ni(tta)_2$•tmeda indicates that films are in the antiferromagnetic phase. Conversely, bands at 1350 cm^{-1} and 1600 cm^{-1} (Figure 2.2.1.6a, b) indicates carbon contamination for NiO films deposited from $Ni(hfa)_2$•tmeda.

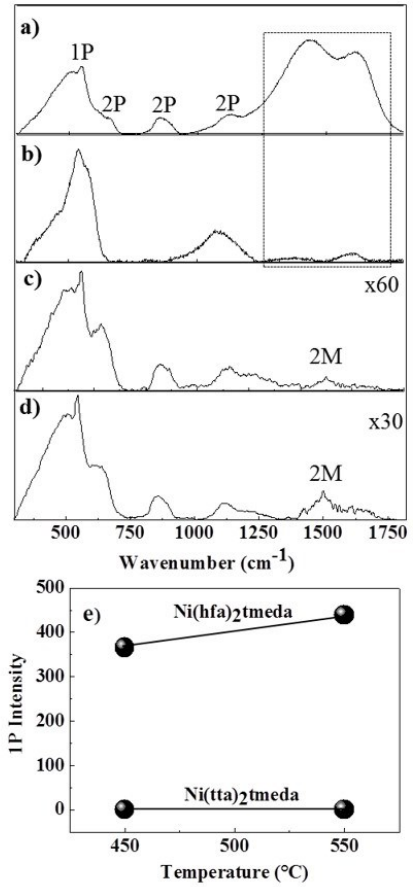

Fig. 2.2.1.6. Raman Spectra of NiO films on quartz from Ni(hfa)$_2$• tmeda at (a) 450°C and (b) 550°C and from Ni(tta)$_2$• tmeda at (c) 450°C and (d) 550°C. (e) Evolution of the 1P intensity as a function of temperature and precursor.

The NiO films have mirror-like surfaces and are homogeneous also in terms of morphology, over the whole area, as indicated by FE-SEM and AFM images, shown in figure 2.2.1.7. For both precursors, the grain size increases with the increase of deposition temperature. At the lowest temperature of 350°C, the surfaces of films deposited from both precursors are very smooth and very small grains of about 50 nm are found (Figure 2.2.1.7a and b). This is in accordance with the amorphous nature of the films. At higher temperature, films grown from the Ni(tta)$_2$•tmeda show homogeneous surfaces with cubic grain dimensions going from about 90 nm at 450°C (Figure 2.2.1.7c) to 130 nm at 550 °C (Figure 2.2.1.7e). In the case of films deposited from the Ni(hfa)$_2$•tmeda, a flat, homogeneous surface with small grains of 100 nm is observed at 450°C

(Figure 2.2.1.7d), while large structured leaf-like grains of 250-300 nm are found at 550°C (Figure 2.2.1.7f). The increases of the grain size with temperature is expected, since higher temperatures give rise to higher mobility of the atoms/molecules on the surface, thus favoring growth vs. nucleation and producing films with larger grains. The morphology of films deposited at 550 °C on LAO (001) substrate (Figure 2.2.1.7g) exhibits a smooth surface with crystalline cubic grains of about 70-80 nm.

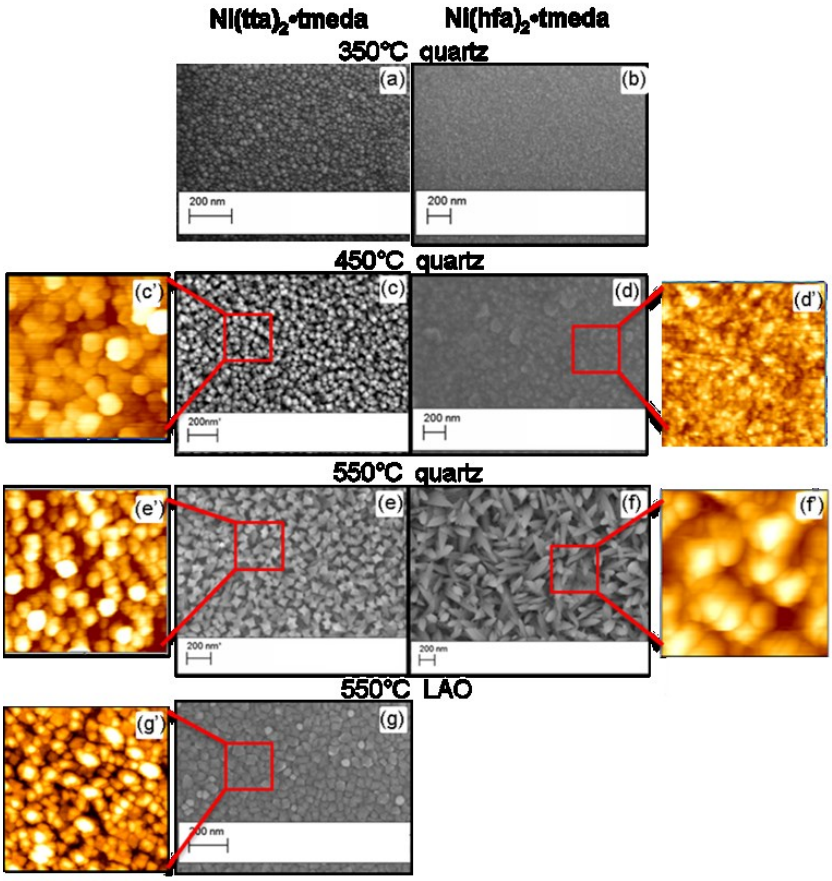

Fig. 2.2.1.7 FE-SEM images of NiO films deposited on (a-f) quartz substrate and (g) on LAO from (a, c, e, g) $Ni(tta)_2$•tmeda and (b, d, f) $Ni(hfa)_2$•tmeda. The corresponding 1μmx1μm AFM topographical images (c', d', e', f' and g') are also shown.

Dependence of grain size on temperature is reported in figure 2.2.1.8a. AFM images, reported as appended figures, confirm the FE-SEM morphology giving quantitative information on the root mean square (RMS) roughness. Indeed, results, summarized in figure 2.2.1.8b, show a smoother morphology for films from $Ni(tta)_2$•tmeda on both quartz and LAO substrates with a RMS

roughness going from 3 to 5 nm, while an increase of roughness with temperature from 2.5 nm to 45 nm is observed for films from $Ni(hfa)_2$•tmeda.

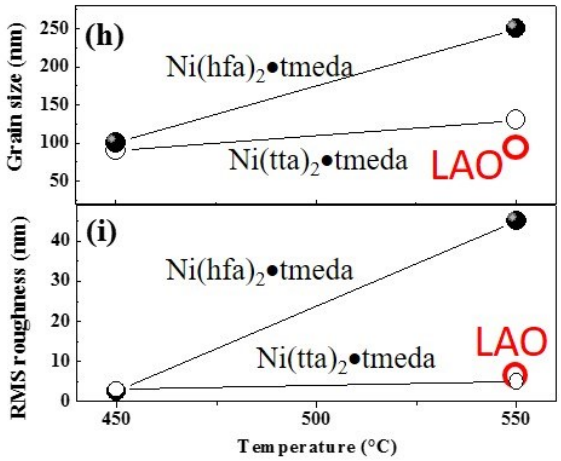

Fig. 2.2.1.8 Evolution of the (a) grain size and (b) roughness (RMS) as a function of temperature, precursor and substrate.

The optical properties have been tested through UV-Vis and ellipsometric measurements. The transmittance spectra show that the NiO films from $Ni(tta)_2$•tmeda (Figure 2.2.1.9a) are highly transparent in the visible region with optical transmission nearly 90% between 450 nm and 800 nm for the amorphous layer grown at 350°C. On increasing the deposition temperature the optical transmission is approximately 80% between 550 and 800 nm. The optical transmittances of films grown from the $Ni(hfa)_2$•tmeda, reported in figure 2.2.1.9b, result to be worse than those observed for films obtained from $Ni(tta)_2$•tmeda.

Therefore, the UV-Vis spectral data point to better transparent properties for the NiO films grown at 450°C from the $Ni(tta)_2$•tmeda.

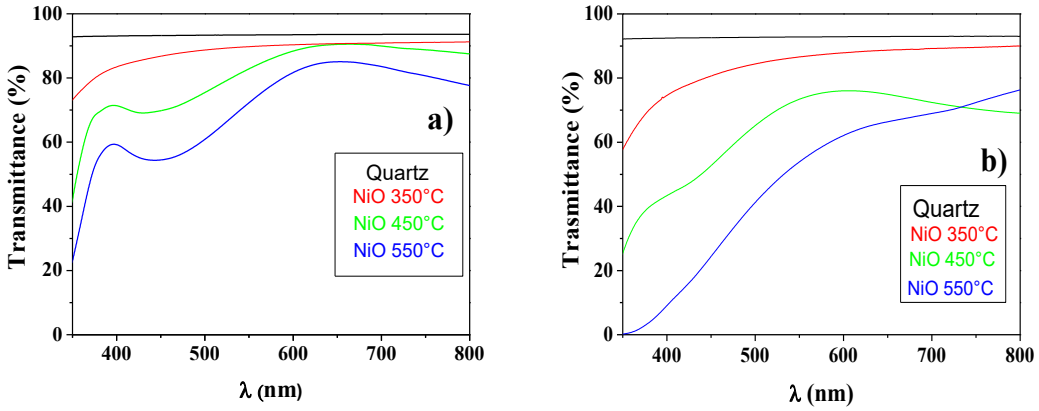

Fig. 2.2.1.9 Transmittance spectra of NiO films on quartz from (a) $Ni(tta)_2$•tmeda and (b) $Ni(hfa)_2$•tmeda as a function of temperature.

Figure 2.2.1.10a shows the spectra of the refractive and extinction coefficient derived by the ellipsometric analysis for the NiO film grown at 450°C from the $Ni(tta)_2$•tmeda. The comparison of the spectra of the absorption coefficient also shows a good agreement with the NiO single crystal. The observed slight difference is due to a lower density of the films due to their polycrystalline structure.[41]

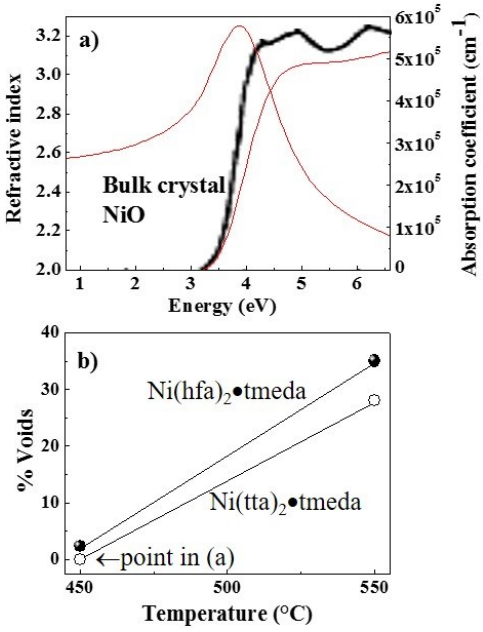

Fig. 2.2.1.10 (a) Spectra of the refractive index and absorption coefficient, derived by the ellipsometric analysis, of the NiO film on quartz.; (b) Evolution of the % voids (measure of the film density) as a function of temperature and precursor.

The densest film is deposited at 450°C from $Ni(tta)_2$•tmeda; the increasing of voids fraction in figure 2.2.1.10b indicates that the density of the NiO films decreases with the $Ni(hfa)_2$•tmeda precursor and with the increase of the temperature, consistently with the change in morphology seen in Figure 2.2.1.7 (larger grains and less compact microstructure observed with the increase in temperature). From the $(\alpha E)^2$ vs. energy, E, plot, a direct optical gap of 3.7 eV has been estimated that compares well with the value of 3.8-4.0 eV of the single crystal NiO.[42] As for the role of the O_2 flow, previous studies indicated[43] that the quality of NiO also depends on the O_2 quantity.

Therefore, using the $Ni(tta)_2$•tmeda precursor, NiO films have been deposited at 450°C under three different O_2 flows of 50, 200 and 600 sccm. Figure 2.2.1.11 shows the optical properties, in the region of the absorption edge, of the NiO films derived by the ellipsometric analysis as a function of O_2 flow on quartz substrate.

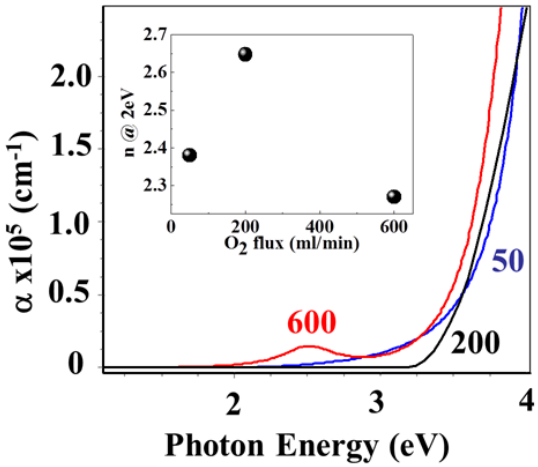

Figure 2.2.1.11 Absorption coefficient around the fundamental absorption edge of NiO films grown on quartz at different O_2 fluxes of 50, 200 and 600 sccm. The inset shows the corresponding value of the refractive index, n, at the photon energy of 2 eV.

The higher refractive index and density and the sharper absorption edge indicate that the optimal O_2 flow is 200 sccm. Specifically, for excess of O_2 flow (e.g. 600 sccm), nickel vacancies alter the band structure[44] and result in a low energy (2-3 eV) absorption peak correlated to nickel $3d^8$-$3d^{8*}$ transitions. Conversely, at lower O_2 flow (e.g 50 sccm) O^{2-} vacancies inhibit the previous peak, but defects result in a band tail absorption.

To summarize, the present results indicate that NiO films obtained from $Ni(tta)_2$•tmeda precursor show both morphological and optical properties better than those found for samples grown from $Ni(hfa)_2$•tmeda, thus indicating that the former precursor is more suitable to the MOCVD growth of high quality NiO films. Note that the transparency of the layer and the very low interface and surface roughness make these films potentially interesting for applications in light-emitting devices[30] or photovoltaics.[45,46]

2.2.2 MOCVD fabrication of NiO dielectrics

Depending on the targeted application, the NiO thin films are grown on different substrates and with a specific stoichiometry, in order to obtain the desired electrical characteristics. In particular, the stoichiometric NiO can be considered an intrinsic semiconductor (thus a semi-insulating material), which by heating treatments at high temperatures can combine with atmospheric oxygen becoming a fairly good electrical conductor (NiO_x).[47,48] This behavior has been also shown by other transition metal compounds containing the metal in two oxidation states.[49,50] In the case of NiO_x ($x>1$), the Ni cations possess +2 and +3 oxidation states and the excess of oxygen anions creates vacant sites normally occupied by nickel ions. In order to maintain the electrical neutrality inside the crystal, Ni^{2+} slightly oxidizes to Ni^{3+}, thus electrons can be transferred from Ni^{2+} ions to the adjacent Ni^{3+} ions through a mechanism of "electronic jumping" which leaves behind a gap.[51,52]

Therefore, NiO can be used either as insulator or as p-type semiconductor, both characteristics make it an appealing material for microelectronics applications. A growing field inmicroelectronics is the development ofwide band gap semiconductor devices and in particular those based on AlGaN/GaN heterostructures.[53-55] In this context, one of the main issues to be addressed is the growth of a suitable dielectric to optimize the critical device parameters, such as channel mobility, parasitic capacitance and gate leakage current. Some oxides, for instance SiO_2, Al_2O_3, Ga_2O_3, HfO_2, and Sc_2O_3, have been tested as potential dielectrics but some drawbacks are still present.[56-60]

Here, NiO thin films are proposed because of their potentially low lattice mismatch if epitaxially grown on AlGaN/GaN heterostructures and because of their high permittivity value (11.9).[61]

Metal Organic Chemical Vapor Deposition (MOCVD) approach is used, since among the different fabrication methods, it represents a reliable and reproducible technique for large-scale production of highly uniform films in both thickness and composition. Moreover, it is noteworthy that it is the dominant technique for the commercial production of GaN-based materials. Hence, the possibility to grow also the gate dielectric by MOCVD could be a driving force to establish this technology in nitride-based devices.[38,39]

Several depositions have been conducted to verify the possible use of NiO thin films in GaN-based transistors. The experimental parameters have been appropriately varied in order to optimize the film growth conditions and to investigate their effects on the electrical properties. Firstly, the deposition temperature has been varied during the growth. In particular, depositions of NiO thin films have been carried out at both low (500 °C) and high (750 °C) temperatures and with a constant oxygen flow (200 sccm), in order to study the influence of deposition temperature on the structural properties of the obtained films. Fig. 2.2.2.1a shows the XRD patterns of NiO films deposited under the two temperatures. In both cases, the obtained NiO showed a preferential <111> growth direction since, apart from the peaks due to the AlGaN/GaN system in the 30–36.5° and 69–79° 2θ ranges, the other two peaks at 37.4° and 79.8° can be related to the 111 and 222 reflections of the NiO phase (ICDD card # 47-1049). In order to complete the XRD investigation, the grain dispersion along the c-axis has been evaluated by recording the rocking curves around the 111 NiO reflection. The fullwidth at halfmaximum (FWHM) of the peaks is similar for both films deposited at different temperatures, i.e., 0.35° (500 °C) and 0.3° (750 °C), thus indicating an excellent out-of-the plane alignment of the NiO films (Fig. 2.2.2.1b). Thus, it can be concluded that the deposition temperature does not significantly affect the structural properties of the deposited films, which in any case are [111] oriented. In addition to the studies on the structural properties, morphological characterization has been performed using FE-SEM and TEM investigations.

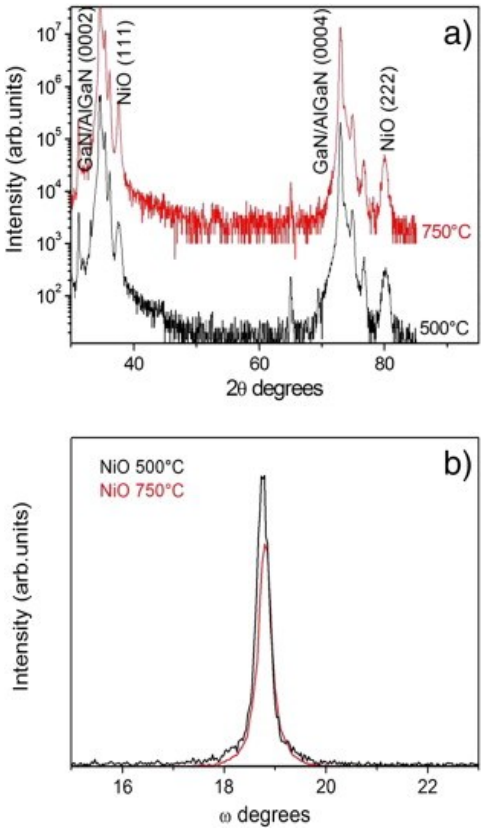

Fig. 2.2.2.1 XRD patterns (a) of NiO films deposited at 500 °C and 750 °C. Rocking curves (b) using the (111) NiO reflection.

Fig. 2.2.2.2 shows the FE-SEM images of the surface morphology of samples deposited at low and high temperatures and using oxygen flows of 200 and 500 sccm. These two oxygen flow values have been used as representatives for the samples deposited in the 50–200 sccm and 300–500 sccm ranges, respectively. In low temperature deposited samples (Fig. 2.2.2.2a and b) the formation of small grains has been observed. The sample deposited using a 200 sccm O_2 flow does not show defined grains, which in turn are quite visible in the sample obtained with a 500 sccm O_2 flow. However, in both films the presence of surface cracking has been observed. The FE-SEM images of samples deposited at 750 °C with oxygen flows of 200 and 500 sccm are shown in Fig. 2.2.2.2c and d. In both cases, larger grains are formed with respect to the case of depositions carried out at 500 °C and also in this case a higher O_2 flow provided more defined grains. In order to improve the morphological characteristics and to avoid the surface cracking, further depositions have been carried out on 45° tilted substrate and setting a very slow (1 °C/min) cooling rate down to room

temperature after the deposition. In fact, the observed cracks could be due to the different thermal expansion coefficients for the NiO film (14.5×10^{-6} K^{-1}) and the substrate (3.17×10^{-6} K^{-1}).

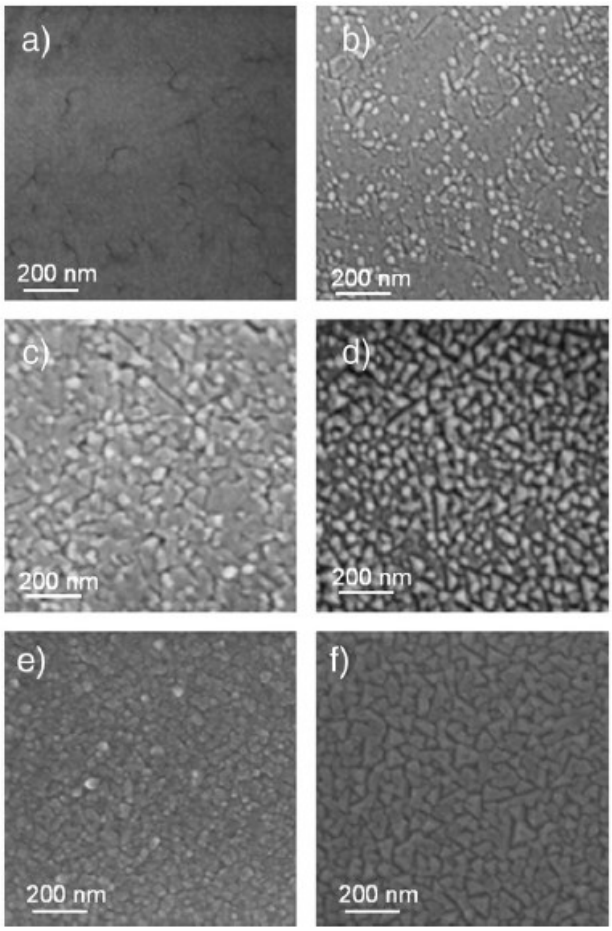

Fig. 2.2.2.2 FE-SEM micrographs of NiO films deposited: (a) at 500 °C with 200 sccm oxygen flow, (b) at 500 °C with 500 sccm oxygen flow; (c) at 750 °C with 200 sccm oxygen flow, (d) at 750 °C with 500 sccm oxygen flow, (e) at 500 °C with 200 sccm oxygen flowand tilted substrate, (f) at 750 °C with 200 sccm oxygen flow and tilted substrate.

In Fig. 2.2.2.2e and f samples deposited at 500 °C and 750 °C, with substrate tilting and using a 200 sccm oxygen flow are shown. All the films obtained under these conditions show a compact grain distribution and the absence of surface cracking. Moreover, for applications in microelectronics two important parameters have to be considered in order to get the improved performances: the dielectric thickness should not exceed a few tens of nanometers and the quality of the dielectric/substrate interface should be free from intermediate layers and/or defects. In this context, films obtained without surface cracking have been investigated through cross-section TEM analysis

to evaluate the thickness and the interface quality. Fig. 2.2.2.3 shows the cross-sectional TEM images of both films deposited at low (500 °C) and high (750 °C) deposition temperatures. The sample obtained at low temperature (Fig. 2.2.2.3a) shows very compact grains, forming a continuous layer with a thickness of about 15 nm. The sample obtained at high temperature (Fig. 2.2.2.3b) shows a completely different morphological profile, as previously evidenced by FE-SEM surface images. In fact, in this case the film thickness is about 30 nm, and the grains have pyramidal shape, thus resulting in a remarkable surface roughness. The film/substrate interface quality has been studied by high resolution TEM images. As can be seen in Fig. 2.2.2.3c, no intermediate layers are visible at the interface, thus ruling out any interaction and/or oxidation of the substrate. Moreover, the Fast Fourier Transform (FFT) image (Fig. 2.2.2.3d), collected at the interface, clearly points out the epitaxial growth of the NiO films. In fact, the external spots related to the NiO are perfectly aligned to the internal ones from the AlGaN, indicating that the NiO lattice is not rotated with respect to the underlying substrate lattice. In particular, the spots related to the [111] NiO direction are aligned and almost overlapped to the spots from [001] AlGaN/GaN direction, and the NiO [110] and [311] directions are parallel to the [110] and [112] directions of the AlGaN/GaN substrate. Moreover, to complete the structural investigation, in-plane TEM image and electron diffraction data have been recorded on NiO films grown at 500 °C. The in-plane TEM image (Fig. 2.2.2.3e) shows small grains of about 20 nm wide. The related electron diffraction pattern (Fig. 2.2.2.3f) consisted of spots forming two hexagonal patterns (white circles) at 2.77 Å and 1.59 Å plane distances which can be related to (100) and to the (110) AlGaN/GaN planes, while spots forming the hexagonal pattern (red circles) at 1.47 Å can be related to the (220) NiO planes. The NiO spots are perfectly aligned to the AlGaN/GaN spots at 1.59 Å. Hence, it is possible to conclude that an epitaxial growth of the {111} NiO planes on the (0001) substrate plane occurred and the following relationships are present:

$$[111]\text{NiO} \parallel [0001]\ \text{AlGaN/GaN}$$

$$[110]\text{NiO} \parallel [11{-}20]\ \text{AlGaN/GaN}.$$

Finally, additional morphological information on the low temperature deposited NiO films has been attained by AFM. In particular, the root-mean-square roughness of the height distribution (RMS or surface roughness), measured on a scanned area of 2μm^2, was 2.77 nm on NiO films, i.e., only slightly higher than the one measured on AlGaN bare substrate before the deposition (2.01 nm).

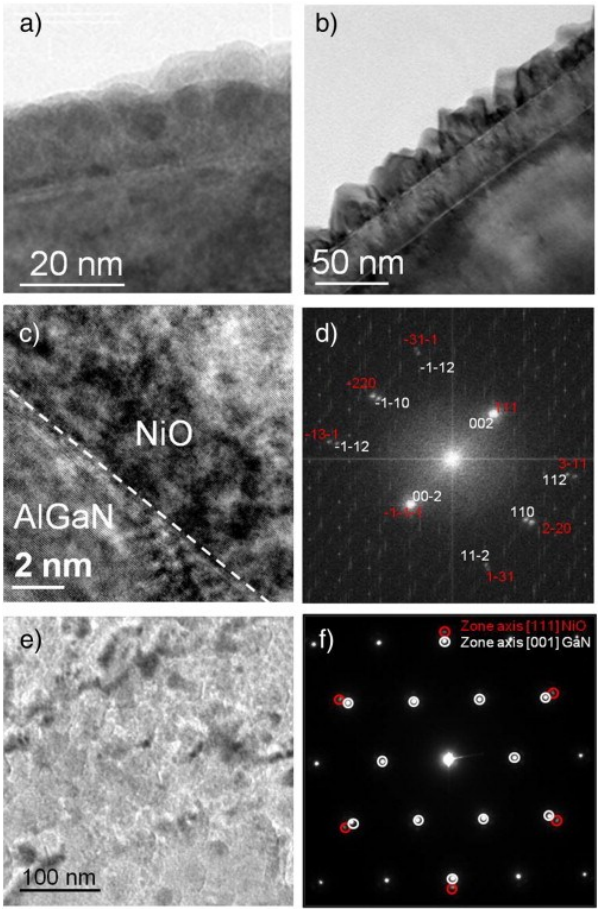

Fig. 2.2.2.3 TEM cross-sections of NiO films deposited at (a) 500 °C and (b) 750 °C. High resolution TEM image (c) of the NiO/AlGaN interface and its relative Fast Fourier Transform image (d). TEM in-plane image (e) of the NiO film deposited at 500 °C and the relative electron diffraction patterns (f) from the substrate (white circles) and from the NiO film (red circles).

Hence, although both low and high temperature deposited samples are epitaxial and possess excellent quality of the interface, it has been concluded that the best suited samples to be investigated for the electrical characteristics are those deposited at low temperature because of the lower roughness and the presence of more compact grains.

The dielectric properties of the NiO thin films have been evaluated by the characterization of electrical test-patterns fabricated on AlGaN/GaN substrates.[62] Firstly, the deposited NiO film has

been patterned by photolithography and wet-etched, to define a circular geometry for metal–insulator–semiconductor Schottky diodes (MIS-Schottky). A metal multilayer Ti/Al/Ni/Au stack has been deposited by sputtering on theNiO surface and annealed in Ar at 850 °C to create ohmic contacts.[63,64]

Finally, Ni/Au metal electrodes have been defined by lift-off, onto the NiO circular islands. Moreover, conventional Schottky diodes, with the Ni/Au gate electrode contacting directly the AlGaN surface, have been fabricated on the same sample as a reference. C–V measurements have been carried out to investigate the semiconductor or insulating nature of the NiO deposited films and to determine their permittivity. Fig. 2.2.2.4a shows the C–V measurements at a frequency of 1 MHz of the NiO/AlGaN/GaN diode and of the AlGaN/GaN reference device.

Clearly, a decrease of the accumulation capacitance in the NiO/AlGaN diodes with respect to the reference device occurs, accompanied by a shift of the C–V curve towards amore negative bias. This latter is the usual behavior expected in the presence of an insulating gate. The measured capacitance in the C–V curves of theMIS diode (CMIS) can be considered as the series capacitance of the reference AlGaN barrier layer (CAlGaN) and of the NiO insulating layer, i.e.,

$$1/C_{MIS} = 1/C_{AlGaN} + 1/C_{NiO} \qquad (1)$$

By applying Eq. (1) to the experimental data reported in Fig. 2.2.2.4a and considering the decrease of the accumulation capacitance in the MIS diodes with respect to the reference diode (from $C_{AlGaN} = 1.95 \times 10^{-7}$ F/cm^2 to $C_{MIS} = 1.52 \times 10^{-7}$ F/cm^2) the capacitance of the NiO layer ($C_{NiO}=6.89\times10^{-7}$ F/cm^2) has been calculated and consequently, the NiO permittivity has been estimated to be 11.7. This value is in good agreement with the NiO bulk permittivity and properly higher than that of AlGaN alloys.[54] Finally, the I–V characteristics (Fig. 2.2.2.4b) measured on the same diodes showed a reduction of the leakage current of more than a factor of 100 (at bias= −1 V) by the introduction of the NiO layer.

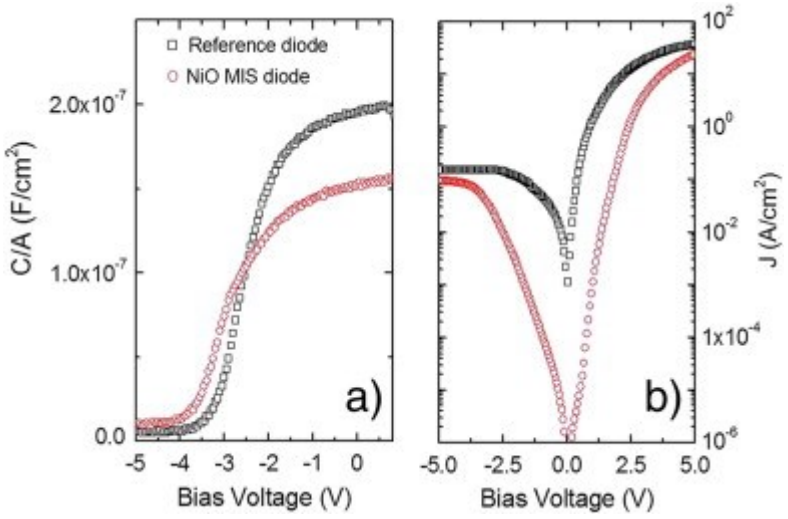

Fig. 2.2.2.4 C–V (a) and I–V (b) curves of AlGaN/GaN diodes as reference (squares) and of NiO/AlGaN/GaN diodes (circles).

In conclusion, the deposited films are adherent, have uniform thickness and smooth surfaces. Morphological differences have been observed by varying deposition temperature and the oxygen flow values. The best suited deposition conditions demonstrated to be T_{dep}= 500 °C, 200 sccm oxygen flow, 45° tilted substrate position and slow cooling rate (1 °C/min) after deposition. XRD and TEM analyses demonstrated that the films are epitaxial and that the film/substrate interface has a good quality. The epitaxial films have a permittivity of 11.7, very close to the NiO bulk value, as evaluated through capacitance–voltage (C–V) measurements on insulated Schottky devices on AlGaN/GaN heterostructures and comparing the obtained data with the C–V of a non-insulated diode. Furthermore, the leakage current in NiO/AlGaN metal–insulator–semiconductor Schottky diodes was reduced by 2–3 orders of magnitude. These results indicated that the NiO films are promising insulators for GaN devices.

2.3 Synthesis of new heterobimetallic β–diketonate sodium-yttrium and sodium- gadolinium precursors

During last years, upconversion materials have attracted a raising interest: their applications space from photovoltaic, due to their unique capacity to improve the energy conversion efficiency of solar cells,[65] to biological field, because the excitation and emitted radiations derived from upconversion are in the 700−1000 nm spectral range, i.e., in the transparent transmission window of biological fluids.[66]

Notably, $NaREF_4$ (RE = Gd, Y, Lu) sodium lanthanide tetrafluorides have been reported to be the ideal UC host for Ln^{3+} activators such as Yb^{3+}/Er^{3+} (Tm^{3+}, Ho^{3+}).[67-75]

$NaREF_4$ exists in two polymorphic forms at ambient pressure and temperature: the cubic (α) and the hexagonal (β), the latter phase being the most efficient host matrix for UC emission.

As a consequence, hexagonal β-$NaREF_4$ phases co-doped with Yb^{3+}/Er^{3+}(Tm^{3+}, Ho^{3+}) have been widely studied, and up to date are considered the most efficient upconverters.[76-80]

Up to now, a lot of effort has been made on the synthesis and applications of $NaYF_4$:Yb,Er crystals or powders.[81-83]

Different groups have reported the synthesis of lanthanide co-doped hexagonal $NaYF_4$ nano-crystal by hydro- and solvo-thermal methods.[84-86]

However, the above methods suffered from different drawbacks ranging from unfriendly experimental conditions, such as dealing with highly corrosive and toxic reagents, high reaction temperature, requirement of specialized reaction vessels, etc, to undesired forms of materials like large particle size, getting cubic phase alone and particle aggregation. A soft chemical approach is an alternate route to solid-state materials where a molecular compound containing the component element(s) is used in a chemical vapor deposition (CVD), Metal–Organic Decomposition (MOD) or sol–gel process to obtain high-purity films or powders.[87] These chemical routes overcome many of

the drawbacks of the physical methods listed above and facilitate a better control over the composition, structure and morphology of the nanomaterials.

So far, synthesis of Er^{3+}/Yb^{3+} co-doped $NaYF_4$ material in thin film form has been scarcely investigated.[19]

$NaGdF_4$ nanocrystals are considered among the most efficient host materials for bright upconversion luminescence. Furthermore, these compounds are very suitable for creating multifunctional materials owing to their unusual magnetic and optical properties.[88,89] They have been recently emerged as optical imaging nanoprobes and magnetic resonance image contrast agents for magnetic/optical bimodal detection.[90-93]

The $NaGdF_4$ host lattice doped with lanthanide combinations of Yb^{3+} and Er^{3+} has been considered as a bifunctional material combining with upconversion emission and magnetic properties.

Recently, the synthesis of highly efficient $NaGdF_4$ nanocrystals doped with lanthanide ions through solution procedures has been well developed.[94,95] However, for photonic applications, the upconversion materials have to be preferably made with thin films or be embedded into a transparent matrix. Up do date, there is only one report of $NaGdF_4$ synthesis as thin film.[96]

A sol–gel method and pulsed laser deposition (PLD) are the most commonly reported methods used to synthesize UC films.[97-99]

However, the sol–gel method requires post-deposition heat treatment, which may induce reactions between the phosphors and the gel, leading to the luminescence properties of the prepared film being uncontrollable. Although PLD can fabricate films with good optical properties, it is a relatively expensive and complex technique.

Compared to conventional physical vapor deposition techniques, the MOCVD takes advantage of simpler, less costly equipment, ready scalability, and higher throughput.

The success of a MOCVD technique relies upon the availability of monomeric, thermally stable, highly volatile, and low melting adducts. All these properties are of relevance and, in particular, liquid or low melting precursors represent the most desirable sources because of the greater and

stable vapor pressure, the absence of any effects of crystallite size on the evaporation rate, and hence, on the film growth rate. Therefore, an accurate knowledge of the physical properties and thermal behaviour of precursors is of fundamental relevance for the optimization of processes in the perspective of achieving uniform and reproducible film growth. Several precursors such as metal alkyls and alkoxides have been used for their volatility but their toxicity and poor stability toward temperature, moisture and other chemicals limited wider uses. On the other hand, metal β-diketonate complexes show better stability toward hydrolysis and temperature, and they have a discrete volatility and are non toxic. Up to date, the β-diketonate of second generation, in which the coordination sphere is completed by various Lewis base ligands, such as polyamine or polyglymes, represent the most desirable sources due to their excellent mass transport properties.

In the perspective of the synthesis of multicomponent films, the availability of suitable precursors is of crucial importance. In conventional MOCVD, the metal sources of multimetal films such as $NaREF_4$ must be compatible in term of volatility to make easier the control of stoichiometry in films. In this context, it is more desirable the availability of a single source heterometallic precursor, containing all the required elements (Na,Y,F) in a single molecule, which would not only ensure greater homogeneity at atomic levels and the absence of unnecessary contaminating ions but also make it easy to control the process.

So far, Mishra et al. reported[100,101] the synthesis of different heterometallic single source precursors for the solution synthesis of $NaREF_4$ nanomaterials $[NaLn(TFA)_4(diglyme)]$, $YNa(TFA)_4(diglyme)$, $[Na(triglyme)_2][Y_2(TFA)_7(THF)_2]$ and $Na_2Y(TFA)_5$-(tetraglyme).

However, all the reported precursors showed a multistep TG and decomposition at low temperature, in the range of 250-300°C. The thermal behaviour found for these complexes is an important issue for their application into CVD processes, since thermal stability is a fundamental requirement.

2.3.1 Synthesis and characterization of a new β–diketonate heterobimetallic sodium-yttrium precursor

In early papers, it has been proved the favorable properties of a large family of single-source precursors to fabricate high quality films of alkaline-[102] and rare-earth fluorides.[103] These sources are based on molecular architectures consisting of a fluorinated β-diketonate metal array whose coordinative deficiency was saturated by various Lewis base ligands, such as polyethers.[104] The ancillary polyethers coordination was proved to strongly stabilize the metal center and to preclude oligomerization, thus resulting in monomeric, thermally stable, highly volatile, and low melting adducts. All these properties are of relevance and, in particular, liquid or low melting precursors represent the most desirable sources because of the greater and stable vapor pressure, the absence of any effects of crystallite size on the evaporation rate, and hence, on the film growth rate. In this work, a synthetic strategy for the synthesis of a new heterobimetallic precursor of formula $NaY(hfa)_4$·tetraglyme [Hhfa=1,1,1,5,5,5-hexafluoro-2,4-pentanedione and tetraglyme= bis[2-(2-methoxyethoxy)ethyl] ether] is reported.

The adduct has been prepared through a one-pot reaction from yttrium nitrate source, sodium hydroxide, hexafluoroacetylacetone and tetraglyme in dichlorometane (eq.1)

$$Y(NO_3)_3\cdot 6H_2O + 4Hhfa + 4NaOH + tetraglyme \rightarrow NaY(hfa)_4\cdot tetraglyme + 10H_2O + 3NaNO_3$$

Experimentally, the $Y(NO_3)_3\cdot 6H_2O$ (0.674 gr, 1.76 mmol) was first suspended in dichloromethane (40 mL). Tetraglyme (0.392 g, 1.76 mmol) was added to the suspension. NaOH (0.310g, 7.7 mmol) and Hhfa (1.47 g, 7.0 mmol) were added under vigorous stirring after 10 min and the mixture was refluxed under stirring for 1 h. Colorless crystals precipitated after partial evaporation of the solvent. The crystals were collected, washed with pentane, filtered, and dried under a vacuum.

A slight eccess of NaOH (10%) has been used. NaOH exerts a double effect: it serves as a base able to deprotonate the acidic hydrogen of Hhfa and it is the source of the sodium. The procedure yields reproducibly, under open bench manipulations, a clean source adduct. It has a very low melting point and evaporates quantitatively at low temperature under vacuum and even under atmospheric pressure. The composition of the present precursor has been investigated by energy dispersive X-ray analysis (EDX). The EDX spectrum, reported in Figure 2.3.1.1, shows the presence of the Yttrium L peak at about 1.9 KeV. The peaks at 0.67 keV and 1.04 keV are due to the F Kα and Na Kα peaks, respectively, whereas the peak at 2.120 KeV is due to the Au sputtered on the sample. In addition, note that the quantitative analysis allowed to define the ratio between Na:Y in the complex, being approximately 1:1. Note that the value of light elements may not be quantitatively correct, since no particular attention has been paid to quantify them.

a)

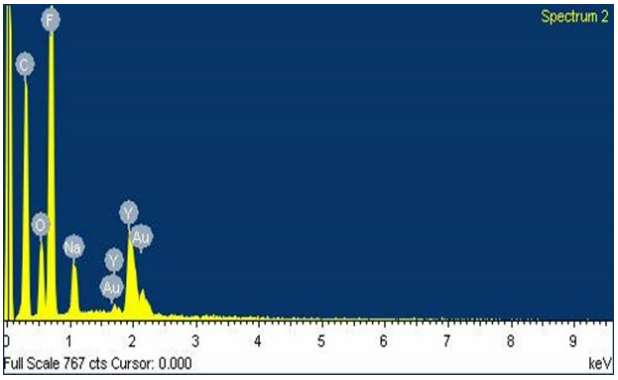

b)

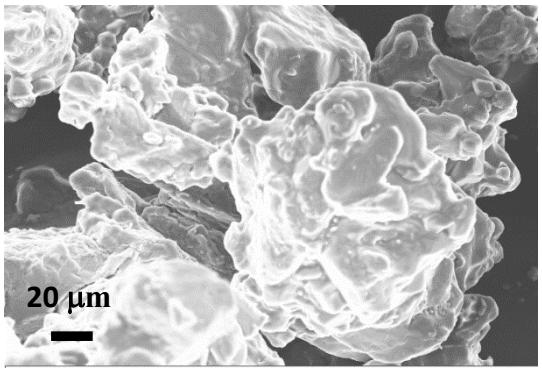

c)

Element	Weight%	Atomic%
C K	33.09	47.08
O K	14.90	15.92
F K	37.22	33.49
Na K	2.03	1.51
Y L	8.56	1.64
Au M	4.20	0.36
Totals	100.00	

Fig. 2.3.1.1 FE-SEM image (a), EDX spectrum (b) and quantitative analysis (c) of NaY(hfa)$_4$·tetraglyme.

The identity of complex was further established by single crystal X-ray diffraction study. X-ray grade single crystal of $[Y(hfa)_4]^-[Na*tetraglyme]^+$ was grown from a mixture of pentane/dichlorometane.

The structure can be described as $[Y(hfa)_4]^-[Na•tetraglyme]^+$. The ionic complex crystallizes in the monoclinic space group Cc with one unit in a cell of dimension a= 22.6674(9) Å, b = 9.0585(3) Å; β = 116.034(5)c = 23.4672(9) Å (Table 2.3.1.1). A view of the complex is given in figure 2.3.1.2. In this ionic structure, the Na atom is five-coordinated by oxygen atoms of tetraglyme, while Y cation is octa-coordinated by the oxygens of the 4 hfa anions.

Table 2.3.1.1. Crystal data and refinement of the $[Y(hfa)_4]^-[Na•tetraglyme]^+$ complex.

Formula	$[Na(C_{10}H_{22}O_5)][Y(C_5HO_2F_6)_4]$
M	1162.41
Sistema cristallino, gruppo spaziale	Monoclino, Cc
Parametri di cella (Å, °)	a = 22.6674(9)
	b = 9.0585(3); β = 116.034(5)
	c = 23.4672(9)
V (Å^3)	4329.7(3)
Z	4
λ (Å)	0.71073
T (K)	120
D_{calc}	1.738
μ (mm^{-1})	1.518
Riflessi raccolti/unici	45326/13779(R int = 0.0654)
Riflessi con I>2σ	8870
Rapporto dati/parametri	13779/948
Valori finali di R	0.0551, 0.0917
	0.1036, 0.1082

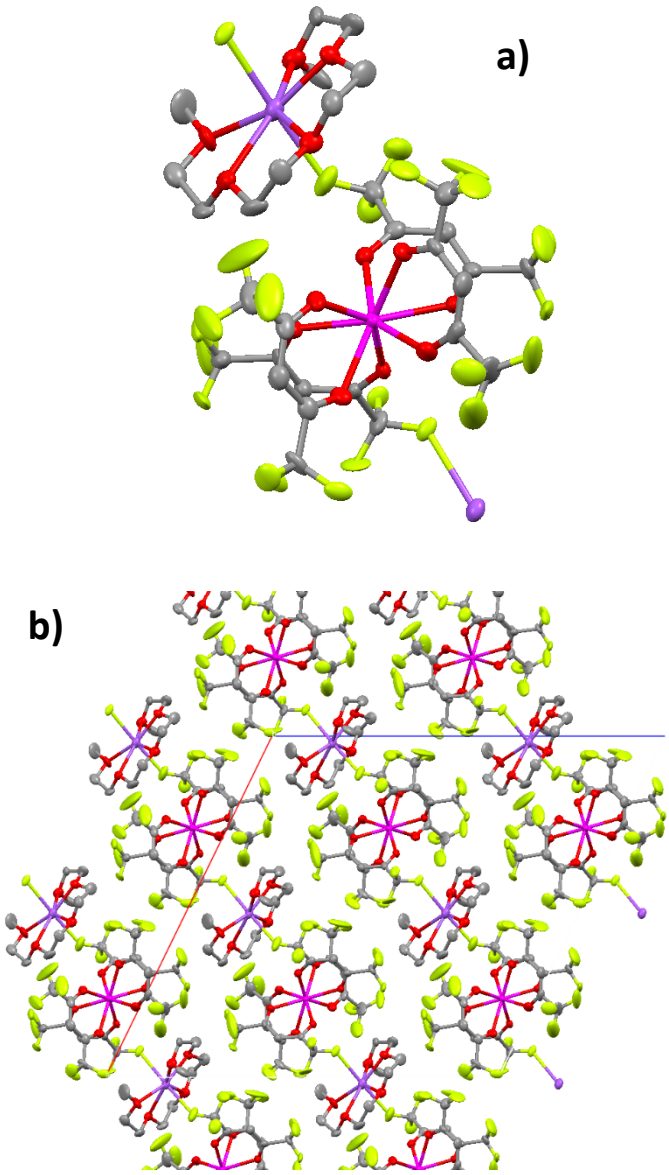

Fig. 2.3.1.2 a) Ball and stick representation of the complex $[Y(hfa)_4]^-[Na•tetraglyme]^+$. Atom colours: C in grey, O in red, Y in purple, Na in blue, F in yellow. b) Crystal packing of the $[Y(hfa)_4]^-[Na•tetraglyme]^+$.

Further information about the complex structure was given by infrared spectroscopy. The FT-IR transmittance spectrum of the complex $[Y(hfa)_4]^-[Na•tetraglyme]^+$ adduct (Fig. 2.3.1.3) shows the absence of OH stretching around 3500 cm^{-1}, thus confirming the anhydrous nature of the complex. The carbonyl stretching frequency appears at 1657 cm^{-1}, whereas peaks at 1557 and 1530 cm^{-1} are associated with C=O stretching and with C=C stretching vibrations, respectively, and are typical of the β-diketonate framework.

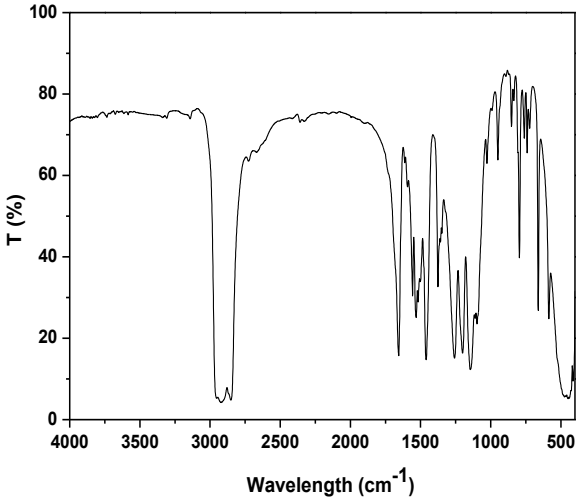

Fig. 2.3.1.3 FT-IR spectrum of complex $[Y(hfa)_4]^-[Na•tetraglyme]^+$

Peaks observed in the 1000-1300 cm^{-1} range are characteristic of the polyether C-O bending and/or stretching overlapped with the C-F stretching features.

In addition, the glyme modes appear at 953, 842 and 797 cm^{-1}. In the spectral range of 2800-3000 cm^{-1} it is possible to find the C-H glyme stretching modes overlapped with nujol features. The nujol shows also peaks at 1461 and 1377 cm^{-1}.

The study of the thermal properties of the Na-Y adduct is a crucial step for a successful MOCVD process. The thermogravimetric (TG) measurement of the complex $[Y(hfa)_4]^-[Na•tetraglyme]^+$ has been carried out at atmospheric pressure under purified nitrogen flow. The TG curve (Fig. 2.3.1.4) indicates that the β-diketonate adduct evaporates quantitatively in the 180-300°C temperature range, with a 8% residue left at 350°C, thus indicating a clean vaporization of the precursor.

The derivative curve of TG (DTG) consists of a single peak thus indicating that the complex evaporation occurs in a single step, without any-side decomposition. From thermal analysis it can be concluded that the heterobimetallic precursor $[Y(hfa)_4]^-[Na•tetraglyme]^+$ shows good mass transport properties as requested for MOCVD applications.

All the investigations clearly indicate that $[Y(hfa)_4]^-[Na•tetraglyme]^+$ is thermally stable and volatile, therefore, this new synthesized heterometallic adduct is expected to be a good precursor for the deposition of sodium and yttrium containing films.

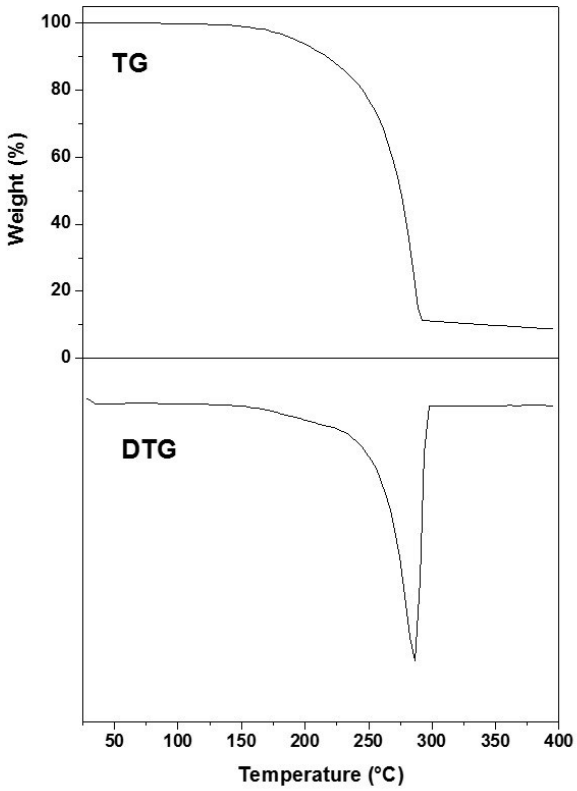

Fig 2.3.1.4 TG and DTG profiles of the $[Y(hfa)_4]^-[Na•tetraglyme]^+$ complex under N_2 flow at atmospheric pressure in the 25-400° °C temperature range.

Hence, the validation of the precursor to MOCVD synthesis of sodium-yttrium containing films has been investigated. MOCVD depositions have been attempted on silicon substrates. Experiments to grow $NaYF_4$ films were attempted at 500 °C substrate temperature and 160 °C precursor vaporization temperature. The vaporized sources were transported to the deposition zone by Ar (150 sccm) as a carrier gas, while oxygen flow (150 sccm) was used as reaction gas. Film were deposited on silicon (100) single crystals substrates. The range of deposition temperature was 400-600°C, the run time was 1 h and the total pressure 6 Torr.

Film characterization from a structural point of view has been assessed by XRD analysis. In fig. 2.3.1.5a is reported the XRD pattern of the $NaYF_4$ film grown at 500°C.

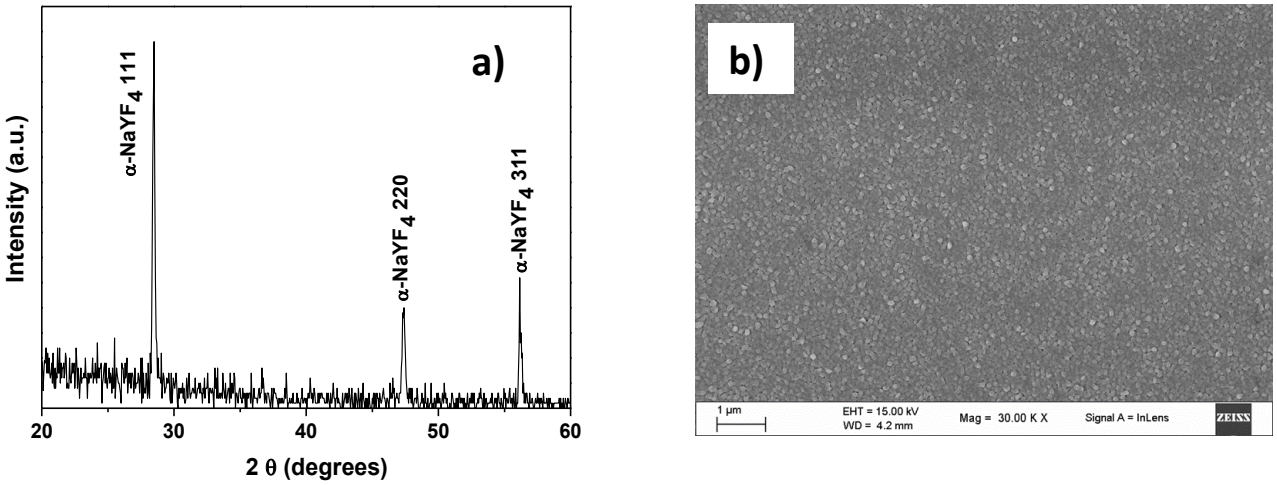

Fig 2.3.1.5 XRD pattern (a) and FE-SEM image (b) of the $NaYF_4$ film deposited with MOCVD at 500°C from $[Y(hfa)_4]^-[Na•tetraglyme]^+$ source.

The peaks at 2θ = 28.50°, 47.36° and 56.12° are easily attributed to 111, 220 and 311 reflections of the cubic phase of $NaYF_4$. No differences were found at different deposition temperatures.

The film morphology was investigated by means of FE-SEM (Fig. 2.3.1.5). The micrography found for a film grown at 500°C evidences a good homogeneity of grains having dimensions of few hundreds of nanometers.

Films composition has been determined by EDX. The spectrum riported in fig 2.3.1.6 shows the presence of yttrium signal arising from L lines spread in the range of 1.8-2.2 keV, sodium Kα peak at 1.06 keV and fluorine Kα peak at 0.65 keV. A small signal of oxygen is visible, arising from the silicon oxide layer of the substrate. In fact, the peak is not detected anymore using a lower acceleration voltage of 5 kV of electron beam. It is worthy to note that Na:Y ratio is about 1:1.

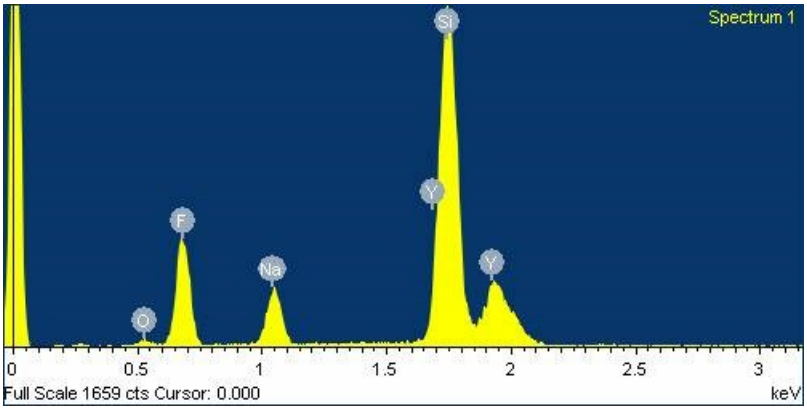

Fig 2.3.1.6 EDX spectrum of $NaYF_4$ thin film deposited from $[Y(hfa)_4]^-[Na•tetraglyme]^+$ source.

2.3.2 Synthesis and characterization of a new β–diketonate heterobimetallic sodium-gadolinium precursor

The availability of heterometallic precursors could represent an important advance in materials synthesis, and for this reason it represents a great challenge. So far, no sodium and gadolinium heterobimetallic precursors have been reported in the literature.

In this study, a novel heterobimetallic sodium and gadolinium based precursor has been synthesized and fully investigated. The attention has been devoted to the synthesis of a new single precursor, the $NaGd(hfa)_4$·tetraglyme [Hhfa=1,1,1,5,5,5-hexafluoro-2,4-pentanedione and tetraglyme= bis[2-(2-methoxyethoxy)ethyl] ether].

The reaction can be conducted in a single step under simple laboratory conditions. The hexahydrate gadolinium nitrate $Gd(NO_3)_3·6H_2O$ (1.035 gr, 2.29 mmol) was first suspended in dichloromethane (40 mL). Tetraglyme (0.392 g, 1.76 mmol) was added to the suspension. NaOH (0.381g, 9.5 mmol) and Hhfa (1.47 g, 7.0 mmol) were added under vigorous stirring after 10 min and the mixture was refluxed under stirring for 1 h. The excess of gadolinium nitrate was filtered off.

The colorless crystals precipitated after partial evaporation of the solvent. The crystals were collected, washed with pentane, filtered, and dried under vacuum.

The reaction yields the water-free adduct $NaGd(hfa)_4 \cdot$tetraglyme, as schematized in the following eqn. (1):

$$Gd(NO_3)_3 \cdot 6H_2O + 4Hhfa + 4NaOH + tetraglyme \rightarrow NaGd(hfa)_4 \cdot tetraglyme + 10H_2O + 3NaNO_3 \quad (1)$$

To establish the presence of both metals Na and Gd in the structure, EDX area and point analyses (Fig 2.3.2.1) have been carried out on powders, previously metallized by a gold sputtered thin layer.

a)

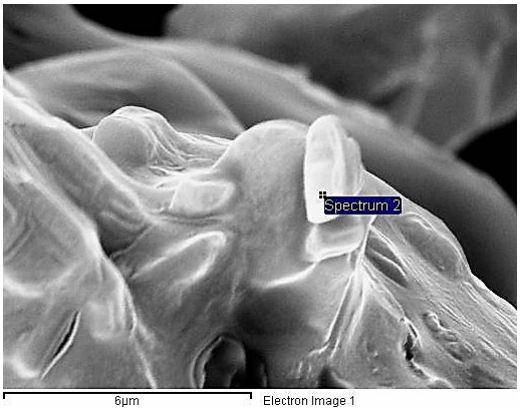

b)

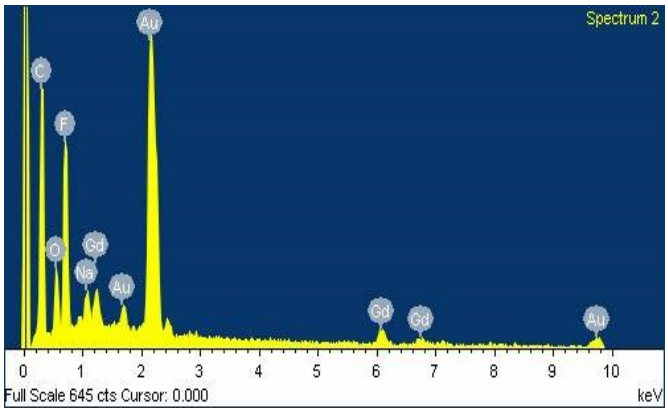

c)

	Weight%	Atomic%
C K	32.53	64.71
O K	5.96	8.90
F K	15.27	19.21
Na K	1.44	1.49
Gd L	8.33	1.27
Au M	36.47	4.42
Totals	100.00	

Fig. 2.3.2.1 FE-SEM image (a), EDX spectrum (b) and quantitative analysis (c) of $NaGd(hfa)_4 \cdot$tetraglyme.

In addition to the elements C, F and O, the EDX data show the presence of Gd L lines observed in the 6-7 keV range, while the Na K_α peak is found at at 1.04 keV. The precursor has almost ideal stoichiometry, namely the Na-Gd ratio is approximately 1:1. Note that the value of light elements may not be quantitatively correct, since no particular attention has been paid to quantify them.

Sodium-gadolinium precursor single crystals were grown from a mixture of pentane/dichlorometane. The solid state crystal structure of the present precursor, determined by mean of X-ray single-crystal diffraction, confirmed the EDX evidences, i.e. the heterobimetallic nature of the adduct. A view of the complex is given in figure 2.3.2.2. In the ionic structure of formula $[Gd(hfa)_4]^-[Na•tetraglyme]^+$, the gadolinium cation is coordinated by the eight oxygen atoms of four hfa anions, while the coordination sphere of sodium is fulfilled by the oxygen atoms of one tetraglyme molecule, giving rise to a pentacoordination. It is worthly to note that no water molecules take part to the coordination sphere, as also noticed by FT-IR (see below). The used crystals are slightly twinned, so the structure is only partially refined, giving the monoclinic space group Ia, with cell parameters a = 21.719(2), b = 15.341(7), c = 17.319(2) Å, β = 120.19(1)°, V = 4987.7(6) $Å^3$.

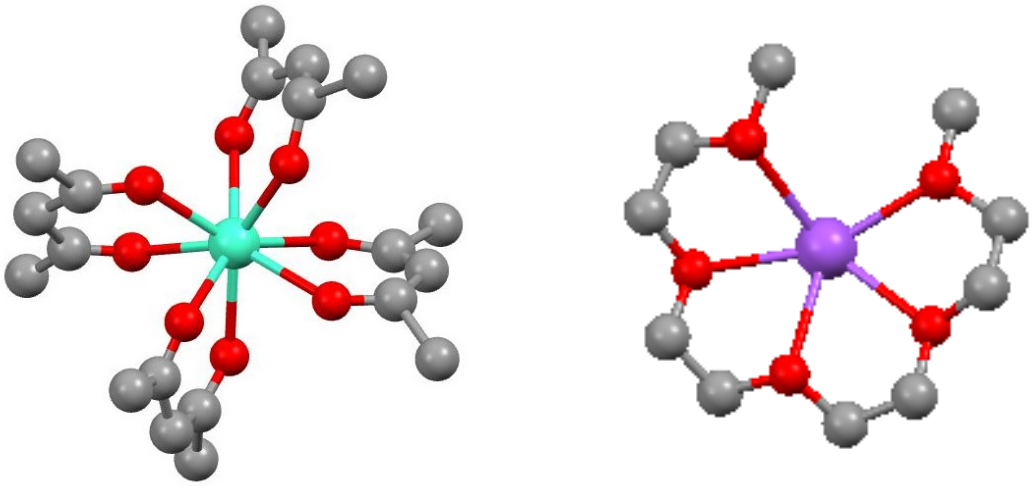

Fig. 2.3.2.2 Ball and stick representation of the adduct $[Gd(hfa)_4]^-[Na•tetraglyme]^+$. Colours of atoms: C in grey, O in red, Gd in green, Na in purple.

The complex structure was further investigated by FT-IR analysis. The FT-IR transmittance spectrum of the complex $[Gd(hfa)_4]^-[Na\bullet tetraglyme]^+$ adduct (Fig. 2.3.2.3) does not show any band in the 3500-3600 cm^{-1} interval as expected for a water-free species. The carbonyl stretching frequency appears at 1654 cm^{-1}, whereas peaks at 1556 and 1531 cm^{-1} are associated with C=O stretching and with C=C stretching vibrations, respectively. The bands observed in the 1000-1300 cm^{-1} range may be associated with absorptions of the polyether C-O bending and/or stretching and the C-F stretching. In addition, bands at 948, 848 and 796 cm^{-1} can be associated with glyme modes. The C-H glyme stretching modes, lying in the 2800-3000 cm^{-1} range, overlap with nujol features. In fact, the nujol shows peaks at 2918, 1425, and 1365 cm^{-1}.

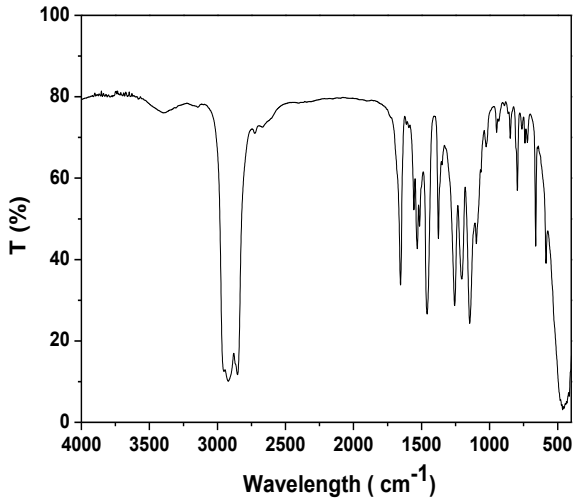

Fig. 2.3.2.3 FT-IR spectrum of $[Gd(hfa)_4]^-[Na\bullet tetraglyme]^+$.

The thermal properties of the $[Gd(hfa)_4]^-[Na\bullet tetraglyme]^+$ complex have been tested by dynamic thermogravimetric analyses at atmospheric pressure under purified nitrogen flow. The adduct evaporates in a single step in a narrow temperature range (190–290 °C) with a low residue (≈18%) left at 350 °C (Fig. 2.3.2.4). The derivative curve of TG (DTG) consists of a single peak thus indicating that the complex evaporation occurs in a single step, without any-side decomposition.

Fig. 2.3.2.4 TG and DTG profiles of the $[Gd(hfa)_4]^-[Na•tetraglyme]^+$ complex under N_2 flow at atmospheric pressure in the 30-400° °C temperature range.

The termogravimetric analysis show that the present heterobimetallic complex possesses good thermal stability, and demonstrates great advantages for practical applications in depositing Na-Gd containing films in MOCVD processes under vacuum.

The final assessment of a potential precursor for MOCVD processes may be only obtained by applying it to the fabrication of the films of interest. In the present case, the $[Gd(hfa)_4]^-[Na•tetraglyme]^+$ precursor has been validated as a single source through its successful application to the fabrication of $NaGdF_4$ films. Several depositions have been carried out in order to find the optimal parameters to synthetize $NaGdF_4$ thin films. Low-pressure MOCVD depositions were performed using a horizontal hot-wall reactor from the $[Gd(hfa)_4]^-[Na•tetraglyme]^+$ single source contained in a resistively heated alumina boat at 160 °C. The volatile precursor was transported to the deposition zone by Ar (150 sccm) as a carrier gas, while oxygen flow (150 sccm) was used as reaction gas. Silicon (100) single crystals were used as substrates. The range of deposition

temperature was 400-600°C, the run time was 1 h and the total pressure 6 Torr. Film structural properties were studied with means of XRD analysis. The θ–2θ pattern of the $NaGdF_4$ film deposited at 500°C is reported in figure 2.3.2.5. The peaks at 2θ = 28.06°, 32.68° and 46.70° and 55.40° can be safely attributed to 111, 200 and 220 and 311 reflections of the cubic phase of $NaGdF_4$. S indicate the peaks of silicon substrate. No differences were found changing deposition temperature. In regard to morphology, the FE-SEM image (Fig. 2.3.2.5b) shows a homogenous smooth surface with 100 nm grains; moreover, the presence on the top surface of 'plate-like' grains of about 800 nm in dimensions can be observed.

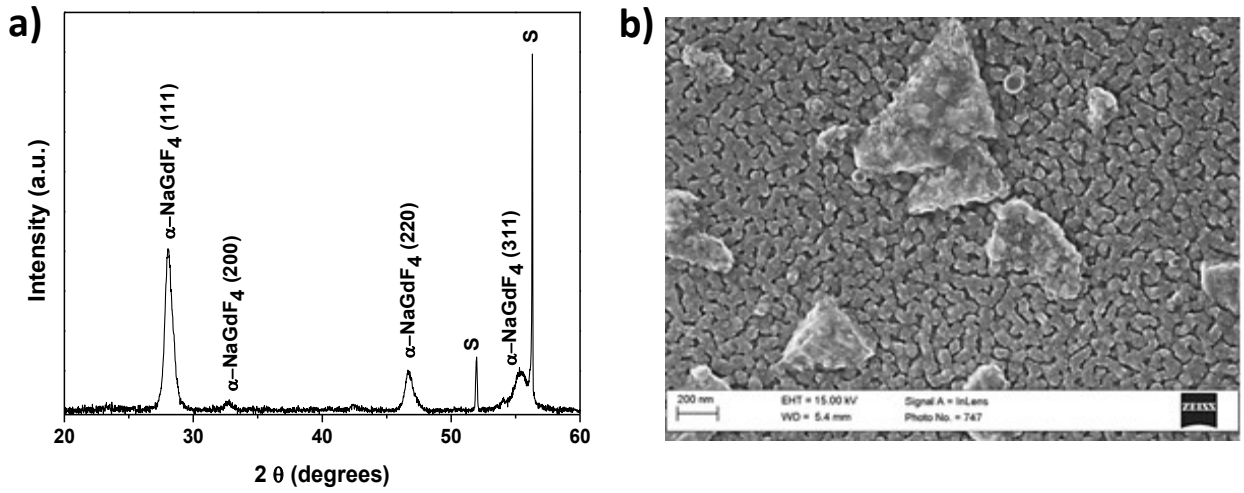

Fig. 2.3.2.5 XRD pattern (a) and FE- SEM image (b) of the $NaGdF_4$ film deposited from $[Gd(hfa)_4]^-$ $[Na•tetraglyme]^+$ source at 500°C.

EDX analysis is reported in Fig. 2.3.2.6. The Gadolinium L lines are spread in the range 6-7 keV. In addition, the windowless EDX detector allowed to detect the F K_α peak at 0.670 keV, and to exclude any O contamination, since no peak is observed at 0.520 keV. The films do not contain O within the detectability limit of the EDX technique (~1%). These data are in agreement with those found in XRD investigation. The atomic % ratio between Na and Gd is approximately 1.

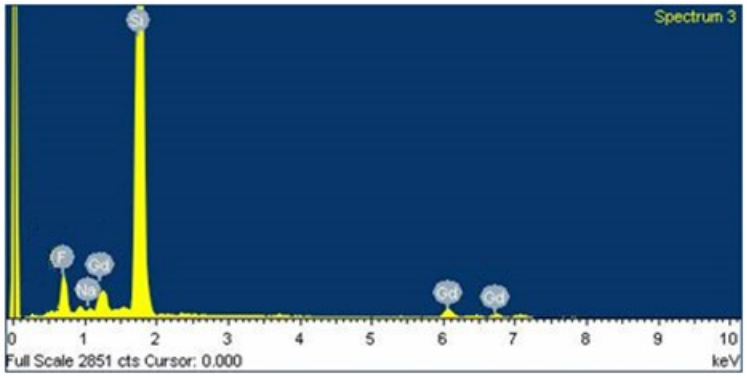

Fig 2.3.2.6 EDX spectrum of $NaGdF_4$ thin film deposited from $[Gd(hfa)_4]^-[Na•tetraglyme]^+$ source.

References

[1] G. G. Condorelli, G. Malandrino and I. L. Fragalà, *Coord. Chem. Rev.*, 2007, **251**, 1931–1950.

[2] G. Malandrino, D.S. Richeson, T.J. Marks, D. C. DeGroot, J. L. Schindler and C. R. Kannewurf, *Applied Physics Letters*, 1991, **58**, 182-4.

[3] G. Malandrino, F. Castelli and I. L. Fragala, *Inorganica Chimica Acta*, 1994, **224**, 203-7.

[4] M. E. Fragala, R. G. Toro, S. Privitera and G. Malandrino, *Chemical Vapor Deposition*, 2011, **17**, 80-87.

[5] M. E. Fragala, R. G. Toro, P. Rossi, P. Dapporto and G. Malandrino*, Chemistry of Materials*, 2009, **21**, 2062-2069.

[6] A. Gulino, F. Castelli, P. Dapporto, P. Rossi, and I. Fragala`, *Chem. Mater.*, 2000, **12**, 548.

[7] G. G. Condorelli, S. Gennaro and I. L. Fragala`, *Chem. Vap. Deposition*, 2001, **7**, 151.

[8] A.Wang, O. A. Belot and T. J. Marks, *J.Mater. Res.*, 1999, **14**, 1132–1136.

[9] F. Emmenegger, C. W. Schlaepfer, H. Stoeckli-Evans, M. Piccand and H. Piekarski, *Inorg. Chem.*, 2001, **40**, 3884**–**3888.

[10] A. Pande, *Synlett*, 2005, **6**, 1042**–**1043.

[11] G. Malandrino, L. M. S. Perdicaro, G. Condorelli, I. L. Fragala, P. Rossi and P. Dapporto, *Dalton Trans.*, 2006, 1101–1106.

[12] D. P. Woodruff, *Chem. Rev*. 2013, **113**, 3863−3886.

[13] M. Kandyla, C. Chatzimanolis-Moustakas, E. P. Koumoulos, C. Charitidis and M. Kompitsas, M*ater. Res. Bulletin,* 2014, **49**, 552-559.

[14] A. M. Soleimanpour, Y. Hou and A. Jayatissa, *Sensors Actuators, B: Chemical*, 2013, **182**, 125-133.

[15] A. Cimino, M. Lo Jacono and M. Schiavello, *J. Phys. Chem.*, 1971, **75***,* 1044–1050.

[16] F. Arena, A. Licciardello and A. Parmaliana, *Catal. Lett.,* 1990, **6**, 139-149.

[17] D. T. Gillaspie, R. C. Tenent and A.C. Dillon, *J. Mater. Chem*., 2010, **20**, 9585-9592.

[18] K.-K. Chiang and J.-J. Wu, *ACS Appl. Mater. Interfaces*, 2013, **5**, 6502-6507.

[19] S. Pereira, A. Goncalves, N. Correia, J. Pinto, L. Pereira, R. Martins and E. Fortunato, *Solar Energy Mater. Solar Cells*, 2014, **120**, 109-115.

[20] R.-T. Wen, G. A. Niklasson and C. G. Granqvist, *ACS Appl. Mater. Interfaces*, 2015, **7**, 9319−9322.

[21] J. W. Shim, C. Fuentes-Hernandez, A. Dindar, Y. Zhou, T. M. Khan and B. Kippelen, *Organic Electronics*, 2013, **14**, 2802-2808.

[22] I. Sta, M. Jlassi, M.Hajji and H. Ezzaouia, *Thin Solid Films*, 2014, **555***,* 131–137.

[23] M. D. Irwin, D. B. Buchholz, A.W. Hains, R. P. H. Chang and T.J. Marks, *PNAS*, 2008**,** **105**, 2783–2787.

[24] M. D. Irwin, , J. D. Servaites, D. B. Buchholz, B. J. Leever, J. Liu, J. D. Emery, M. Zhang, J.-H. Song, M. F. Durstock, A. J. Freeman, M. J. Bedzyk, M. C. Hersam, R. P. H. Chang, M. A. Ratner and T. J. Marks, *Chem Mater.,* 2011, **23**, 2218–2226.

[25] T. Ripolles-Sanchis, A. Guerrero, E. Azaceta,; R. Tena-Zaera and G. Garcia-Belmonte, *Solar Energy Materials & Solar Cells*, 2013, **117**, 564-568.

[26] F. Odobel, L. Le Pleux, Y. Pellegrin and E. Blart, *Acc. Chem. Res.*,2010**, 43**, 1063-1071.

[27] D. Ameline, S. Diring, Y. Farre, Y. Pellegrin, G. Naponiello, E. Blart, B. Charrier, D. Dini, D. Jacquemin and F. Odobel, *RSC Advances,* **2015**, Ahead of Print.

[28] F. Odobel, Y. Pellegrin, E. A. Gibson, A. Hagfeldt, A. L. Smeigh and L. Hammarstrom, *Coord. Chem. Rev.*, 2012, **256**, 2414-2423.

[29] T. J. Macdonald, Y. J. Mange, M. R. Dewi, H. U. Islam, I. P. Parkin, W. M. Skinner, T. Nann, *J. Mater. Chem. A*, 2015, **3**, 13324-13331.

[30] J. –M. Caruge, J. E. Halpert, V. Bulovic´and M. G. Bawendi, *Nano Lett*., 2006, **6**, 2991-2994.

[31] H. Wang, Y. Zhao, C. Wu, X. Dong, B. Zhang, G. Wu, Y.Ma and G. Du, *J. Luminescence,* 2015, **158**, 6-10.

[32] H. P. Rooksby, Nature, 1943, **152**, 304.

[33] N. Mironova-Ulmane, A. Kuzmin, I. Steins, J .Grabis, I. Sildos, M. Pärs, *J. Physics: Conf. Series*, 2007, **93**, 012039/1-012039/5.

[34] A. C. Gandhi, J. Pant, S. D. Pandit, S. K. Dalimbkar, T.–S. Chan, C.–L. Cheng, Y.-R. Ma and S. Y. Wu, *J. Phys. Chem. C,* 2013, **117**, 18666−18674.

[35] A. C. Gandhi, C.-Y. Huang, C. C. Yang, T. S. Chan, C.-L. Cheng, Y.-R. Ma, S. Y. Wu, *Nanoscale Res. Lett.,* 2011, **6**, 485-497.

[36] T. Yoshida, M. Oguni, Y. Mori and Y. Fukuda, *Solid State Comm.*, 1995, **93**, 159-162.

[37] F. Roccaforte, G. Greco, P. Fiorenza, V. Raineri, G. Malandrino and R. Lo Nigro, *Appl. Phys. Lett.*, 2012, **100**, 063511/1-063511/4.

[38] R. Lo Nigro, S. Battiato, G. Greco, P. Fiorenza, F. Roccaforte and G. Malandrino, *Thin Solid Films*, 2014, **563**, 50–55.

[39] R. Lo Nigro, G. Fisichella, S. Battiato, G. Greco, P. Fiorenza, F. Roccaforte and G. Malandrino, *Mater. Chem. Phys*., 2015, **162**, 461-468.

[40] S. H. Lee, H. M. Cheong, N. G. Park, C. E. Tracy, A. Mascarenhas, D.K. Benson and S.K. Deb, *Solid State Ionics*, 2001, **140***,* 135.

[41] D. Franta, B. Negulescu, L. Thomas, P. R. Dahoo, M. Guyot, I. Ohlidal, J. Mistrik and T. Yamaguchi, *Appl. Surf. Sci.*, 2005, **244**, 426-430.

[42] D. Franta, B. Negulescu, L. Thomas, P.R. Dahoo, M. Guyot, I.Ohlidal, J. Mistrik and T. Yamaguchi, *Appl. Surf. Sci.*, 2005, **244**, 426-430.

[43] J.W. Park, K.N. Choi, S.H. Baek, K.S. Chung and H.Lee, *J. Korean Phys. Soc.*, 2008, **52**, 1868-1876.

[44] H. Y. Peng, Y. F. Li, W. N. Lin, Y. Z. Wang, X. Y. Gao and T. Wu, *Sci. Reports*, 2012, 442.

[45] Q. Liu, L. Wei, S. Yuan, X. Ren, Y. Zhao, Z. Wang, M. Zhang, L. Shi, D. Li and A. Li, *RSC Advances*, 2015, **5**, 71778-71784.

[46] J. Y. Park, B. Y. Jang, C. H. Lee, H. J. Yun and J. H. Kim, *RSC Advances*, 2014, **4** , 61248-61255.

[47] A. Wang, J. A. Belot, T. J. Marks, *J. Mater. Res.*, 1999, **14**, 1132.

[48] E. Thimsen, A. B. F. Martinson, J. W. Elam and M. J. Pellin, *J. Phys. Chem. C*, 2012, **116**, 16830.

[49] H. Shima, F. Takano, H. Muramatsu, H. Akinaga, I. H. Inoue and H. Takagi, *Appl. Phys. Lett.*, 2008, **92**, 043510.

[50] A. Chen, S. Haddad, Y. C. Wu, Z. Lan, T. N. Fang and S. Kaza, Appl. Phys. Lett., 2007, **91**, 123517.

[51] S. Seo, M. J. Lee, D.H. Seo, E. J. Jeoung, D.-S. Suh, Y. S. Joung, I. K. Yoo, I. R. Hwang, S. H. Kim, I. S. Byun, J.-S. Kim, J. S. Choi and B. H. Park, *Appl. Phys. Lett.*, 2004, **85**, 5655.

[52] F. Arena, A. Licciardello, A. Parmaliana, *Catal. Lett.*, 1990, **6**, 139.

[53] C. R. Abernathy and B.P. Gila, *Wide Band Gap Electronic Devices*, 2003, 217.

[54] O. Ambacher, J. Smart, J. R. Shealy, N. G. Weimann, K. Chu, M. Murphy,W. J. Schaff, L. F. Eastman, R. Dimitrov, L. Wittmer, M. Stutzmann, W. Rieger and J. Hilsenbeck, *J. Appl. Phys.*, 1999, **85**, 3222.

[55] M. Yanagihara, Y. Uemoto, T. Ueda, T. Tanaka and D. Ueda, *Phys. Status Solidi A*, 2009, **206**, 1221.

[56] R. Suri, C. J. Kirkpatrick, D. J. Lichtenwalmer, V. Misra, *Appl. Phys. Lett.*, 2010, **96**, 042903.

[57] P. Kordos, R. Stoklas, D. Gregusova, J. Novac, Appl. Phys. Lett. 94 (2009) 223512.

[58] Y. C. Chang, W. H. Chang, Y. H. Chang, J. Kwo, Y. S. Lin, S. H. Hsu, J. M. Hong, C. C. Tsai and M. Hong, *Microelectron. Eng.*, 2010, **87**, 2042.

[59] W. H. Chang, C. H. Lee, Y. C. Chang, P. Chang, M. L. Huang, Y. J. Lee, C.-H. Hsu, J. M. Hong and C.C. Tsai, *Adv. Mater.*, 2009, **21**, 4970.

[60] B. Luo, J. W. Johnson, J. Kim, R. M. Mehandru, F. Ren, B. P. Gila, A. H. Onstine, C. R. Abernathy, S. J. Pearton, A. G. Baca, R. D. Briggs, R. J. Shul, C. Monier and J. Han, *Appl. Phys. Lett.*, 2002, **80**, 1661.

[61] J.-K. Ho, C.-S. Jong, C. C. Chiu, C.-N. Huang, K.-K. Shin, L.-C. Chen, F.-R. Chen and J.-J. Kai, *J. Appl. Phys.*, 1999, **86**, 4491.

[62] P. Fiorenza, G. Greco, G. Giannazzo, R. Lo Nigro and F. Roccaforte, *Appl. Phys. Lett.*, 2012, **101**, 172901.

[63] F. Roccaforte, G. Greco, P. Fiorenza, V. Raineri, G. Malandrino and R. Lo Nigro, *Appl. Phys. Lett.*, 2012, **100**, 063511.

[64] R. Lo Nigro, P. Fiorenza, M. R. Catalano, G. Fisichella, F. Roccaforte and G. Malandrino, *Surf. Coat. Technol.*, 2013, **230**, 152.

[65] C.Wang and X. Cheng, *RSC Adv.*, 2015, **5**, 94980–94985.

[66] M. Pedroni, F. Piccinelli, T. Passuello, S. Polizzi, J. Ueda, P. Haro-González, L. Martinez Maestro, D. Jaque, J. García-Solé, M. Bettinelli and A. Speghini, *Cryst. Growth Des.*, 2013, **13**, 4906−4913.

[67] X.Y. Huang, *J. Alloys Comp.*, 2015, **628**, 240.

[68] A. Aebischer, M. Hostettler, J. Hauser, K. Krämer, T. Weber, H. U. Güdel and H. B. Bürgi, *Angew. Chem. Int. Ed.*, 2006, **45**, 2802.

[69] K. Krämer, D. Biner, G. Frei, H. U. Güdel, M.P. Hehlen and S.R. Lüthi, *Chem. Mater.*, 2004, **16**,1244.

[70] P. Ptacek, H. Schäfer, K. Kömpe and M. Haase, *Adv. Funct. Mater.*, 2007, **17**, 3843.

[71] D. Q. Chen and P. Huang, *Dalton Trans.*, 2014, **43**, 11299.

[72] Q. Liu, Y. Sun, T. Yang, W. Feng, C. Li and F. Li, *J. Am. Chem. Soc.*, 2011, **133**, 17122.

[73] P. Ghosh and A. Patra, *J. Phys. Chem. C*, 2008, **112**, 3223.

[74] P. Ghosh and A. Patra, *J. Phys. Chem. C*, 2008, **112**, 19283.

[75] F. Liu, E. Ma, D. Q. Chen, Y. L. Yu and Y. S. Wang, *J. Phys. Chem. B*, 2006, **110**, 20843.

[76] D. K. Chatteriee, A. J. Rufalhah and Y. Zhang, *Biomaterials* , 2007, **29**, 937−943.

[77] J. C. Boyer, C. J. Carling, B. D. Gates and N. R. Branda, *J. Am. Chem. Soc.*, 2010, **132**, 15766−15772.

[78] N. Erathodiyil and J. Y. Ying, *Acc. Chem. Res.*, 2011, **44**, 925−935.

[79] F. Wang, Y. Han, C. S. Lim, Y. Lu, J. Wang, J. Xu, H. Chen, C. Zhang, M. Hong, and X. Liu, *Nature*, 2010, **463**, 1061−1065.

[80] W. Zou, C. Visser, J. A. Maduro; M. S. Pshenichnikov and J. C. Hummelen, *Nat. Photon*, 2012, **6**, 560−564.

[81] M. Liu, Y. Ye, C. Yao, W. Zhao and X. Huang, *J. Mater. Chem. B*, 2014, **2**, 6626–6633.

[82] L. Li, K. Green, H. Hallen and S. F. Lim, *Nanotechnology*, 2015, **26**, 025101.

[83] P. Yuan, Y. H. Lee, M. K. Gnanasammandhan, Z. P. Guan, Y. Zhang and Q. H. Xu, *Nanoscale*, 2012, **4**, 5132–5137.

[84] J. Jhuang, J. Wang, X. Yang, I. D. Williams, W. Zhang, Q. Zhang, Z. Feng, Z. Yang, C. Liang, M. Wu and Q. Su, *Chem. Mater.*, 2009, **21**, 160; C. Li, C. Zhang, Z. Hou, L.Wang, Z. Quan, H. Lian and J. Lin, *J.Phys. Chem. C*, 2009, **113**, 2332; L. Wang and Y. Li, *Chem. Commun.*, 2006, 2557; J. Zeng, J. Su, Z. Li, R. Yan and Y. Li, *Adv. Mater.*, 2005, **17**, 2119; L.Wang, R. Yan, Z. Huo, L.Wang, J. Zeng, J. Bao, X.Wang, Q. Peng and Y. Li, *Angew. Chem., Int. Ed.*, 2005, **44**, 6054.

[85] C. Liu, H. Wang, X. Li and D. Chen, *J. Mater. Chem.*, 2009, **19**, 3546; Y. Wei, F. Q. Lu, X. R. Zhang and D. Chen, *Chem. Mater.*, 2006, **18**,5733.

[86] L. Wang and Y. Li, *Chem. Mater.*, 2007, **19**, 727; L. Wang and Y. Li, *Nano Lett.*, 2006, **6**, 1645.

[87] S. Mishra, E. Jeanneau, M. H. Berger, J.-F. Hochepied and S. Daniele, *Inorg. Chem.*, 2010, **49**, 11184; S. Mishra, E. Jeanneau and S. Daniele, *Polyhedron*, 2010, **29**, 500; S. Mishra, S. Daniele, S.

Petit, E. Jeanneau and M. Rolland, *Dalton Trans.*, 2009, 2569; S. Mishra, S. Daniele and L. G. Hubert-Pfalzgraf, *Chem. Soc. Rev.*, 2007, **36**, 1770; L. G. Hubert-Pfalzgraf, *Inorg. Chem. Commun.*, 2003, **6**, 102.

[88] G. Ren, S. Zeng and J. Hao, *J. Phys. Chem. C*, 2011, **115**, 20141−20147.

[89] C. Liu, Z. Gao, J. Zeng, Y. Hou, F. Fang, Y. Li, R. Qiao, L. Shen, H. Lei, W. Yang and M. Gao, *ACS Nano*, 2013, **7**, 7227−7240.

[90] R. Lv, P. Yang, F. He, S. Gai, C. Li, Y. Dai, G.Yang and J.A. Lin, *ACS Nano*, 2015, 9, 1630−1647.

[91] G. Ajithkumar, B. Yoo, D. E. Goral, P. J.mHornsby, A.-L. Lin, U. Ladiwala, V. P. Dravid and D. K. Sardar, *J. Mater. Chem. B*, 2013, **1**, 1561−1572.

[92] S. Zeng, H. Wang, W. Lu, Z. Yi, L. Rao, H. Liu and J. Hao, *Biomaterials*, 2014, **35**, 2934−2941.

[93] S. Zeng, Z. Yi, W. Lu, C. Qian, H. Wang, L. Rao, T. Zeng, H. Liu, B. Fei and J. Hao, *Adv. Funct. Mater.*, 2014, **24**, 4051−4059.

[94] P. Qiu, R. Sun, G. Gao, C. Zhang, B. Chen, N. Yan, T. Yin, Y. Liu, J. Zhang, Y. Yang and D. Cui, *Theranostics*, 2015, **5**, 456-468.

[95] C. Xiaohong, G. Xingyuan, L. Xiaohui, H. Guanghui, Z. Kezhi, H. Chunfeng and Q. Weiping, *Optical Materials*, 2015, **44**, 13–17.

[96] T. Linlin, W. Ping, W. Hui and L. Run, *RSC Adv.*, 2014, **4**, 19896–19899.

[97] Q. Tang, H. Shen, J. Jiao and W. Chen, *Opt. Mater.*, 2015, **39**, 218–223.

[98] F. Stokker-Cheregi, A. Matei, M. Dinescu, C. Secu and M. Secu, *J. Phys. D: Appl. Phys.*, 2014, **47**, 45304.

[99] G. Qin, W. Qin, C. Wu, S. Huang, J. Zhang, S. Lu, D. Zhao and H. Liu, *J. Appl. Phys.*, 2003, **93**, 4328–4330.

[100] M. Shashank, L. Gilles, J. Erwann, D. Stephane and J. Marie-France, *Dalton Trans.*, 2012, **41**, 1490.

[101] M. Shashank, D. Stephane, L. Gilles, J. Erwann and J. Marie-Franc, *Chem. Commun.*, 2010, **46**, 3756–3758.

[102] G. Malandrino, F. Castelli, I. L. Fragala`, *Inorg. Chim. Acta*, 1994, **224**, 203.

[103] (a) G. Malandrino, L. M. S. Perdicaro and I. L. Fragala`, *Chem. Vap. Deposition*, 2006, **12**, 736. (b) R. Lo Nigro, R. Toro, G. Malandrino, I. L. Fragala`, P. Rossi and P. Dapporto, *J. Electrochem. Soc*., 2004, **151**, F206. (c) R. Lo Nigro, G. Malandrino, I. L. Fragala`, M. Bettinelli and A. Speghini, *J. Mater. Chem.*, 2002, **12**, 2816. (d) G. Malandrino, C. Benelli, F. Castelli and I. L. Fragala, *Chem. Mater.*, 1998, **10**, 3434. (e) G. Malandrino, I. L. Fragala`, S. Aime, W. Dastru`, R. Gobetto and C. Benelli, *J. Chem. Soc., Dalton Trans.*, 1998, 1509. (f) G. Malandrino, O. Incontro, F. Castelli, I. L. Fragala` and C. Benelli, *Chem. Mater.*, 1996, **8**, 1292.

[104] G. Malandrino and I. L Fragala`, *Coord. Chem. ReV.*, 2006, **250**, 1605, and references therein.

Chapter 3: Ferroelectric and multiferroic fluoride materials

3.1 Study of the $BaNiF_4$ film growth

The $BaMF_4$ materials have attracted an increasing attention, since they are known to be ferroelectric compounds. $BaNiF_4$ is representative of this family, and it is ferroelectric. In addition, Ederer et al. have demonstrated the presence of a magnetic order in this compound, thus allowing to define it a multiferroic system.

So far, this class of materials has been synthesized by solid state reactions at high temperature.[1] Nevertheless, this synthetic process requires a complex apparatus. Other synthetic routes include hydrothermal process.[2]

The availability of ferroelectrics and multiferroics in thin film form makes it easier to tailor their properties through epitaxial strain, atomic-level engineering of chemistry and interfacial coupling, and is a prerequisite for their incorporation into practical devices. Hence, the development of low cost and efficient techniques to fabricate thin film ferroelectric fluoride materials represent a challenging goal.

Up to date, there is just one report on the synthesis of $BaMF_4$ fluorides as thin films, and specifically no data are reported for $BaNiF_4$.

In this work, a Metal Organic Chemical Vapor Deposition approach is used to deposit the $BaNiF_4$ phases.

The $Ba(hfa)_2$tetraglyme and $Ni(tta)_2$tmeda have been applied as Ba and Ni single sources. Evaporation/sublimation have been achieved at a constant temperature of 150°C. $BaNiF_4$ films have been deposited on silicon substrates at deposition temperatures ranging from 600 to 700°C.

Argon was used as a carrier gas (flow = 150 sccm), while the reactant gas (O_2 = 150 sccm) was introduced into the main flow in the vicinity of the reaction zone. The nature of deposited films has been investigated by XRD. The XRD studies performed on films deposited at different temperatures

point to the formation of BaF_2 phases, together with the formation of the NiO polycrystalline phase. In fact, the XRD of a sample deposited at 600°C (Fig 3.1.1a) shows the peaks at $2\theta = 37.40°$ and 43.32° related to the 111 and 200 reflections of the NiO phase, respectively, in addition to the peaks at $2\theta = 24.96°$, 28.82°, 41.40°, 48.78° associated with the 111, 200, 220 and 311 reflections of BaF_2 phase, respectively. Characterization showed similar results for films deposited at higher temperature. The films composition has been assessed through EDX qualitative and quantitative analysis. For films deposited at 600°C with oxygen flow, the O K_α peak is clearly visible in the EDX spectrum (Fig 3.1.1b), thus confirming the formation of oxide phases, in agreement with XRD data. Hence, under these experimental conditions the greater stability of the nickel oxide phase with respect to the fluoride one, does not allow the formation of the mixed-fluoride phase $BaNiF_4$.

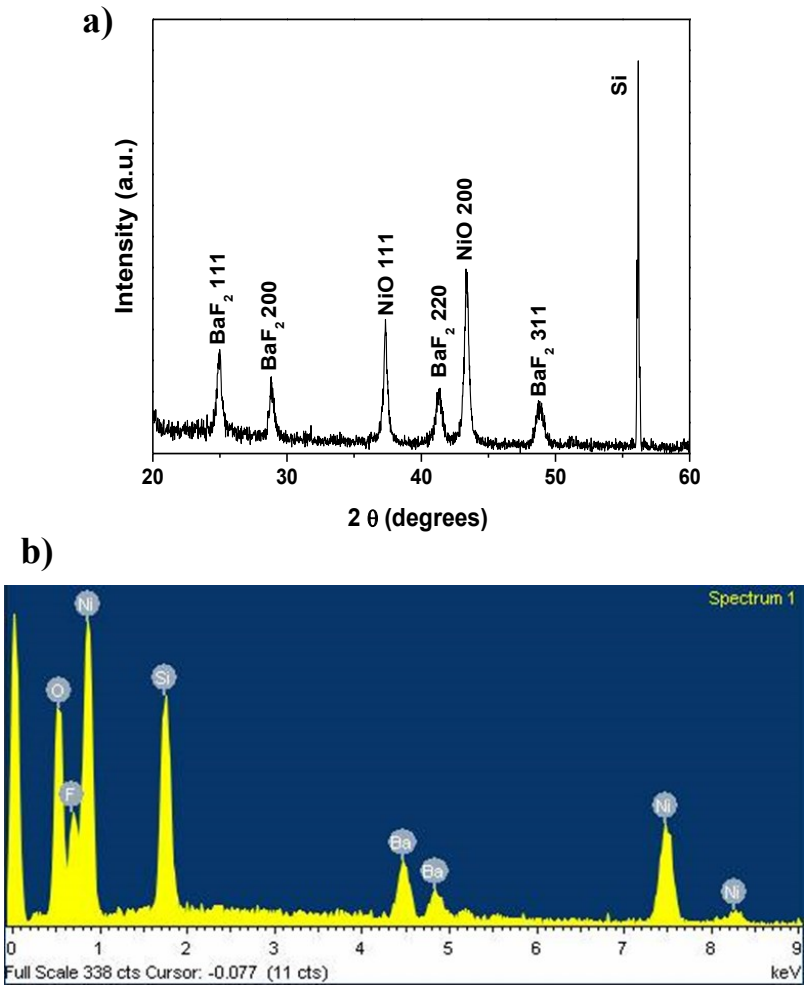

Fig. 3.1.1 XRD pattern (a) and EDX spectrum (b) of a $BaNiF_4$ film deposited at 600°C with oxygen flow.

Further attempts were done to avoid the formation of NiO films. To this aim, depositions without oxygen flow were carried out. Nevertheless, the samples deposited using a zero oxygen flow did not show any peaks related to Ni containing phases (Fig 3.1.2a), thus suggesting the lack of precursor decomposition. This hypothesis has been corroborated by energy dispersive X-ray analysis, which revealed the absence of Ni deposition on the substrate (Fig 3.1.2b). This is in accordance with a previous report in literature,[3] i.e. the formation of the nickel oxide phase has not been observed without using oxygen reaction gas.

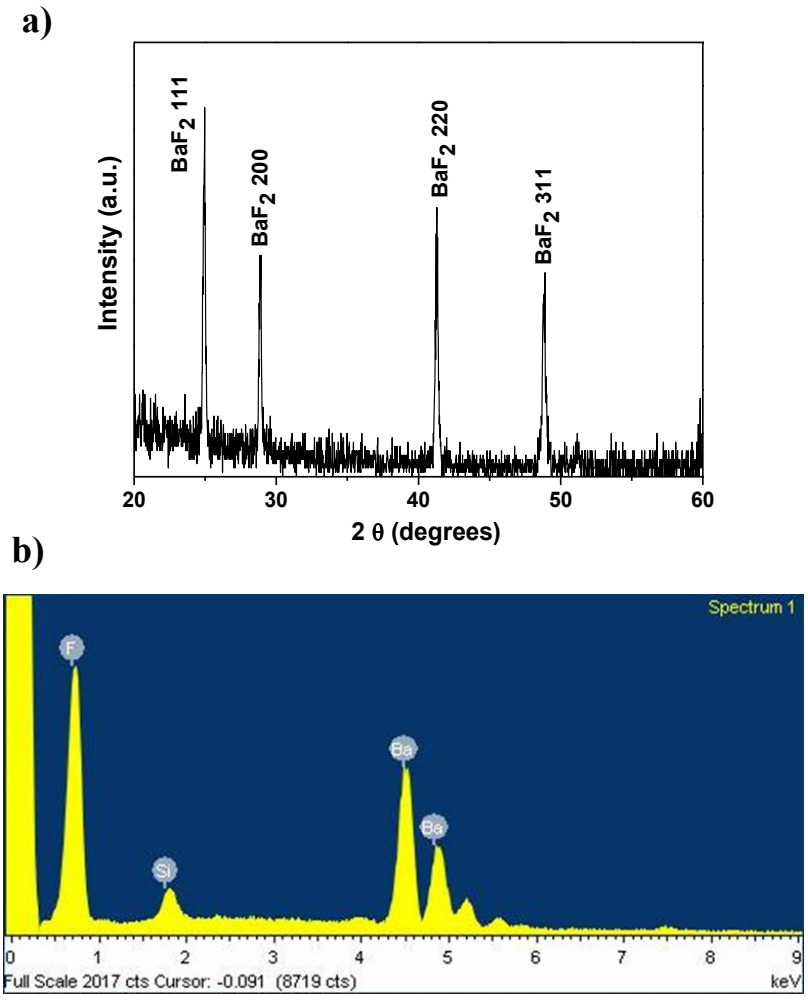

Fig. 3.1.2 XRD pattern (a) and EDX spectrum (b) of $BaNiF_4$ film deposited at 600°C without oxygen flow.

3.2 MOCVD growth of $BaMgF_4$ thin films

The mixed-metal fluoride $BaMgF_4$ (BMF), belonging to the class of $BaMF_4$ isostructural fluorides, has caught substantial attention in view of its interesting and multifunctional properties. BMF compound crystallizes in a base-centered orthorhombic structure with a C*mc2₁* space group and the lattice constants are a=4.126 Å, b=14.518 Å, c=5.821 Å. The Mg cations are octahedrally coordinated by the fluorine anions and four of the fluorine ions of these octahedra are shared with neighbouring octahedra while the barium ions are ordered in BaF_8 polyhedra.[4] BMF is one of the few known ferroelectric fluoride crystals.[5-6] $BaMgF_4$ exhibits room temperature ferroelectric and diamagnetic properties, where the electric polarization in the system is solely due to geometrical distortion and is directed along the c-axis. In particular, both rotational motions of the MgF_6 octahedra and displacements of the Ba cations due to relative ionic size effects and geometrical constraints result in the spontaneous ferroelectric polarization. In addition, the ferroelectric fluoride $BaMgF_4$ has attracted a great attention also due to its wide transparency range and good nonlinear optical properties.[7] Thus BMF crystals have been studied as new solid-state laser materials in the UV region.[8-13]

These properties make BMF a good candidate for integrated optical devices. Although the pure compound doesn't exhibit ferromagnetism, it has been recently demonstrated that this property can be induced by substitutional doping of Mg by a transitional metal ion, e.g. Mn,[14-16] thus realizing a multiferroic material, where ferro/antiferroelectric and ferro/antiferromagnetic properties coexist simultaneously exhibiting electromagnetic coupling. These materials are considered as key components in the development of future technology, for example, in memories and read-write electronic devices.[17]

To date, BMF phases have been synthesized as bulk single crystals by Bridgman method,[18] Czochralski-based growth[19-21] and hydrothermal synthesis[11,12,22-24], or as nanocrystalline material.[25]

Sol-gel techniques to synthesize polycrystalline BMF have also been reported: however, in these reports BaF_2 and/or MgF_2 impurities were found.[26-27]

Nevertheless, for some applications of interest the BMF material is needed in thin film form. In this regard, various physical methods such as molecular beam epitaxy,[28-29] radio frequency magnetron sputtering[30] and sol-gel[31] have been applied. So far, there is only one report on the use of metalorganic chemical vapor deposition (MOCVD) for the growth of BMF films.[32]

In the present work, a synthetic route to produce high quality BMF material in thin film form is reported, comparing two different approaches, Conventional MOCVD (C-MOCVD) and Liquid Injection MOCVD (LI-MOCVD). Both approaches represent chemical, large-area deposition techniques allowing the control over film composition, microstructure and morphology through a suitable choice of substrate, precursor and reactant, as well as deposition parameters. To this aim the $Ba(hfa)_2$tetraglyme and $Mg(hfa)_2(H_2O)_2$diglyme adducts (Hfa=1,1,1,5,5,5-hexafluoroacetylacetone; tetraglyme= 2,5,8,11,14-Pentaoxapentadecane; diglyme= (bis(2-methoxyethyl)ether) have been applied as metal/fluorine single sources, since previous studies have shown that both precursors act as single source for the deposition of BaF_2 and MgF_2, respectively.[33,34] In the conventional system, Ba and Mg precursors are vaporized from the neat sources, while in the injection system the precursors are diluted in a common solvent.

The effect of deposition conditions on the film structural and morphological properties has been investigated by X-Ray diffraction (XRD), field emission scanning electron microscopy (FE-SEM) and transmission electron microscopy (TEM) techniques. In addition, composition and purity has been assessed through energy dispersive X-Ray (EDX) analysis.

3.2.1 Conventional MOCVD synthesis and characterization of $BaMgF_4$ thin films

$BaMgF_4$ films were deposited on $SrTiO_3$ (001) single crystalline substrates and on Si (001) for complementary compositional information. In this study, the precursor evaporation temperature was kept at 150 °C for Ba precursor and 70°C for Mg precursor, whereas the reactor temperature was kept in the 600-700 °C range. The vaporized source materials were transported by a 150 sccm argon gas flow to the deposition zone, while an oxygen flow (150, 550 and 900 sccm) was used as reaction gas. Depositions were carried out for 20 min. The total pressure in the reactor varied between 5 and 11 Torr, depending on the oxygen flow rate. The resulting P_{O_2} was about 2-8 Torr.

The effect of deposition temperature was studied for a constant oxygen partial pressure (2.5 Torr). The structure of films deposited at various temperatures as determined by XRD is summarized in Fig. 3.2.1.1. The θ-2θ diffraction pattern of films deposited on STO (001) in the range 600-650°C indicates the formation of the BMF phase. The pattern of a film obtained at 650°C is reported in fig. 3.2.1.1a. All the peaks in the pattern can be attributed to a polycrystalline BMF phase (ICDD database N° 080-5189) except those due to the STO 001, 002 and 003 reflections observed at 22.82, 46.52 and 72.60° respectively.

The sample peak intensities do not exactly match those reported in the database. Nevertheless, there are not preponderant peaks to assess a preferential growth. Increasing the deposition temperature to 675°C, a significant variation of the films orientation occurs, as it is evident in the pattern reported in Fig. 3.2.1.1b. In addition to the reflections previously found for the films deposited at 650°C, there are intense peaks at 12.26 24.58, 37.18, 50.96, 64.12 and 78.08°, relative to the 0k0 BMF reflections.

The intensity of these peaks becomes greater at 700°C; indeed, the XRD analysis (Fig. 3.2.1.1c) shows the exclusive presence of peaks associated with the 0k0 reflections of the BMF phase, thus

indicating that at this temperature highly oriented films are obtained. The out-of-plane orientation of this film has been determined through ω-scan on the 060 BMF reflection (inset in Fig. 3.2.1.1c).

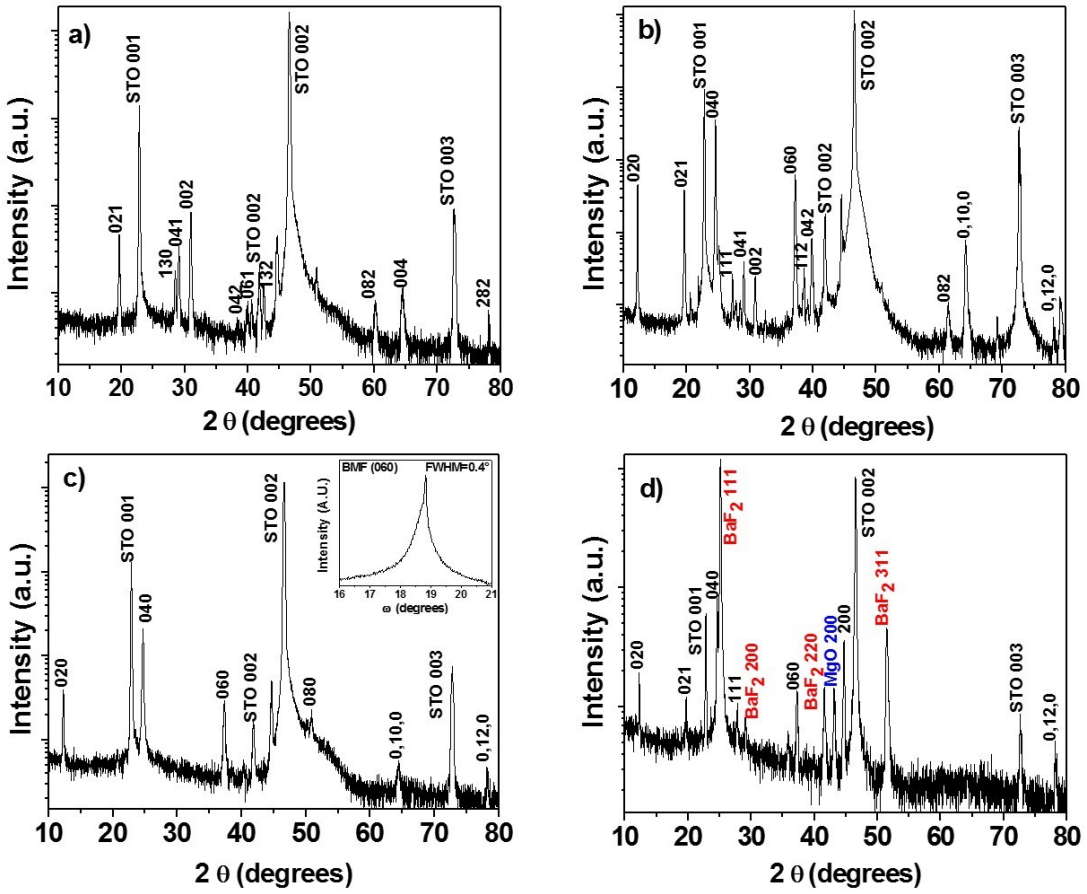

Fig. 3.2.1.1 XRD patterns of BMF films grown with C-MOCVD system on STO (001) substrates with a P_{O_2} of 2.5 Torr at various temperatures: a) 650 °C, b) 675 °C and c) 700 °C. Fig 1d shows the XRD pattern of a BMF film deposited at 700°C with a P_{O_2} of 5.6 Torr.

The full width at half maximum (FWHM) value of 0.4° indicates an excellent out-of-plane alignment of the BMF films deposited at 700°C, indicating a high degree of texturing.

At 700°C and higher oxygen partial pressure (P_{O_2}>5 Torr), the θ–2θ pattern changes completely (Fig. 3.2.1.1d). Reflections attributed to BaF_2 and MgO phase impurities are found, compatible with the oxygen peak detected by EDX (vide infra). These data indicate that at high temperature and for high P_{O_2} a stabilization of the magnesium oxide and barium fluoride phases occurs, thus avoiding the formation of pure mixed metal fluoride phase. To confirm these findings, the atomic

composition of deposited films has been evaluated by Energy Dispersive X-Ray analyses (EDX) on films obtained on silicon substrates. The spectra of films deposited at 600-700 °C with an oxygen partial pressure of 2.5 Torr show the Ba L peaks in the range of 4.5-5.5 keV and the peak due to Mg Kα at 1.3 keV, while no oxygen signal is visible. A typical EDX spectrum representative of a BMF film deposited at 700°C with a P_{O_2} of 2.5 Torr is reported in Fig. 3.2.1.2a. The EDX spectra of samples deposited at 675°C with a P_{O_2} of 8.4 Torr and at 700°C with a P_{O_2} of 5.6 Torr (Fig. 3.2.1.2b) show the presence of the oxygen Kα peak at 0.52 keV. These results are highly reproducible, each experiment being duplicated at least twice.

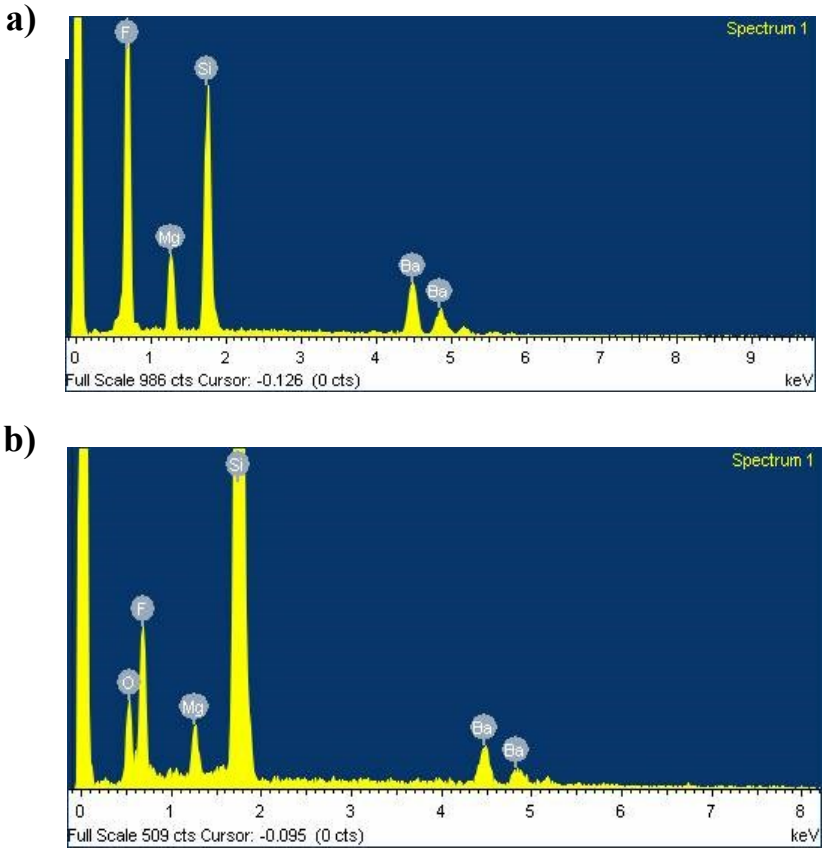

Fig. 3.2.1.2. EDX spectrum of BMF film deposited with C-MOCVD at 700°C with: a) P_{O_2} of 2.5 Torr and b) P_{O_2} of 5.6 Torr.

It can be reasonably considered that film composition is not influenced by the substrates and thus the Ba/Mg ratio obtained from the analysis of films on silicon can be considered representative of

the films deposited on STO. On the other hand, the use of Si vs. STO substrate is mandatory to accurately determine the film composition, due to the presence of oxygen in the STO substrate and to the potential overlap between Ba L lines and Ti K lines deriving from the substrate. To investigate the film morphology, FE-SEM observations have been carried out at the samples surfaces. The images recorded for the samples deposited at 650, 675 and 700°C and P_{O_2} of 2.5 Torr on STO substrates are reported in Fig. 3.2.1.3.

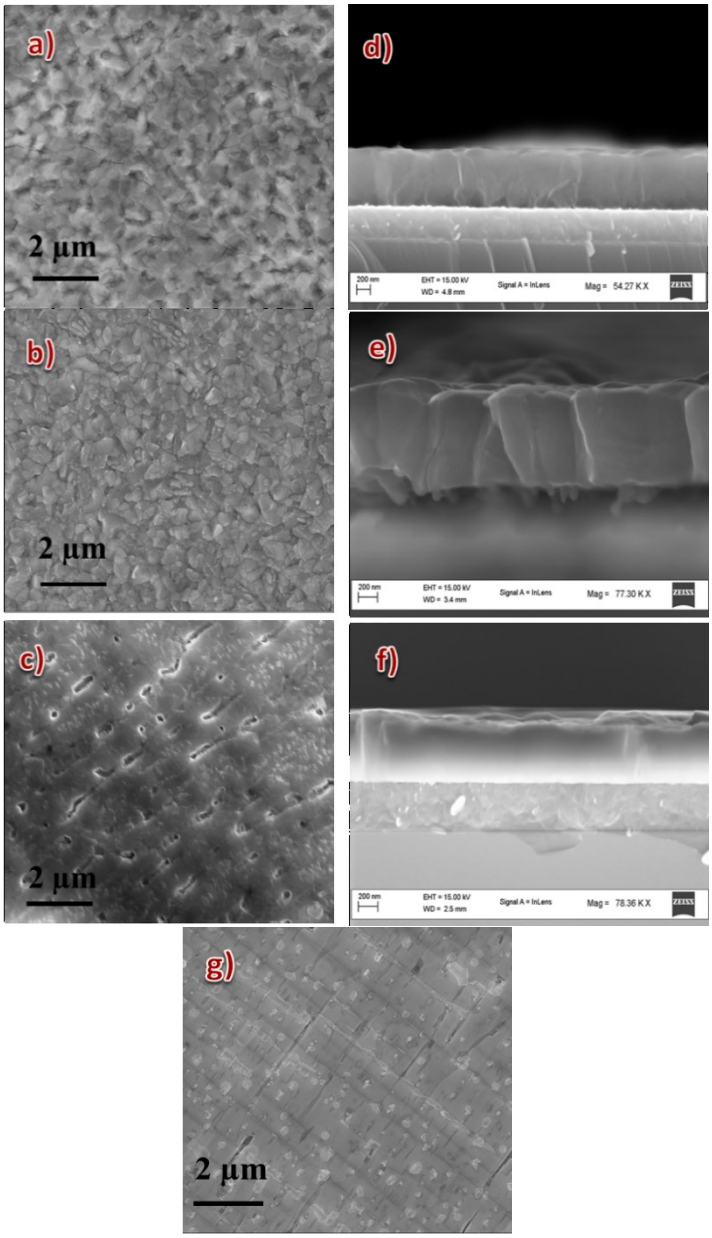

Fig. 3.2.1.3 FE-SEM micrographs of BMF films deposited with C-MOCVD at a) 650, b) 675 and c) 700°C at 2.5 Torr. FE-SEM Cross-section images of films deposited at d) 650, e) 675 and f) 700°C. Fig. g shows the micrography of a BMF film deposited at 700°C with a P_{O_2} of 5.6 Torr.

As can be observed in figure 3.2.1.3a, at lower temperature the grains 400 nm wide are quite disordered, thus suggesting the formation of randomly oriented films. Upon increasing the temperature to 675 (Fig. 3.2.1.3b) and 700 °C (Fig.3.2.1.3c), a significant variation of film topography is observed. In particular, at 700°C a more homogeneous and flat surface has been found, with very large grains of a few microns likely arising from coalescence of smaller grains. FE-SEM cross-section images (Fig. 3.2.1.3d, e and f) allowed to evaluate the thickness of the samples, showing values around 650-700 nm, with a small dependence on the deposition temperature. The sample deposited at 700 °C and P_{O_2} of 5.6 Torr (Fig. 3.2.1.3g) shows an homogeneous, flat surface with rounded outgrowth grains of about 100-200 nm.

3.2.2 Liquid Injection MOCVD synthesis and characterization of $BaMgF_4$ thin films

Deposition of BMF films with the LI-MOCVD has been carried out under similar processing conditions to conventional process in regards to deposition temperature and oxygen partial pressure. The XRD data of films deposited at various temperatures and P_{O_2} = 3.0 Torr are summarized in Fig. 3.2.2.1. A typical θ-2θ XRD pattern obtained for films deposited at 650°C is reported in Fig. 3.2.2.1a. Analogously to the already reported pattern of films deposited using a conventional MOCVD process at the same temperature, many reflections of the BMF phase are present, thus confirming the polycrystalline nature of films deposited at this temperature.

Increasing the temperature to 675°C the XRD data (Fig. 3.2.2.1b) point to the formation of the BMF phase with a slight degree of preferential orientation along the <021> at 19.70° and the <002> at 30.94° directions. Upon increasing the temperature to 700°C, the pattern, shown in Fig. 3.2.2.1c, reveals the presence of a mixture of different phases: $BaMgF_4$, BaF_2 and MgO. At the same temperature and higher P_{O_2} of 7.1 Torr the BMF phase is unstable and only decomposition products BaF_2 and MgO are found. These data are essentially in agreement with those found for films grown with C-MOCVD at 700°C and high P_{O_2}. The small variation could be due to locally altered P_{O_2}

values arising from the different reactor geometries. These data confirm the crucial effect of deposition temperature and P_{O_2} on the phase purity.

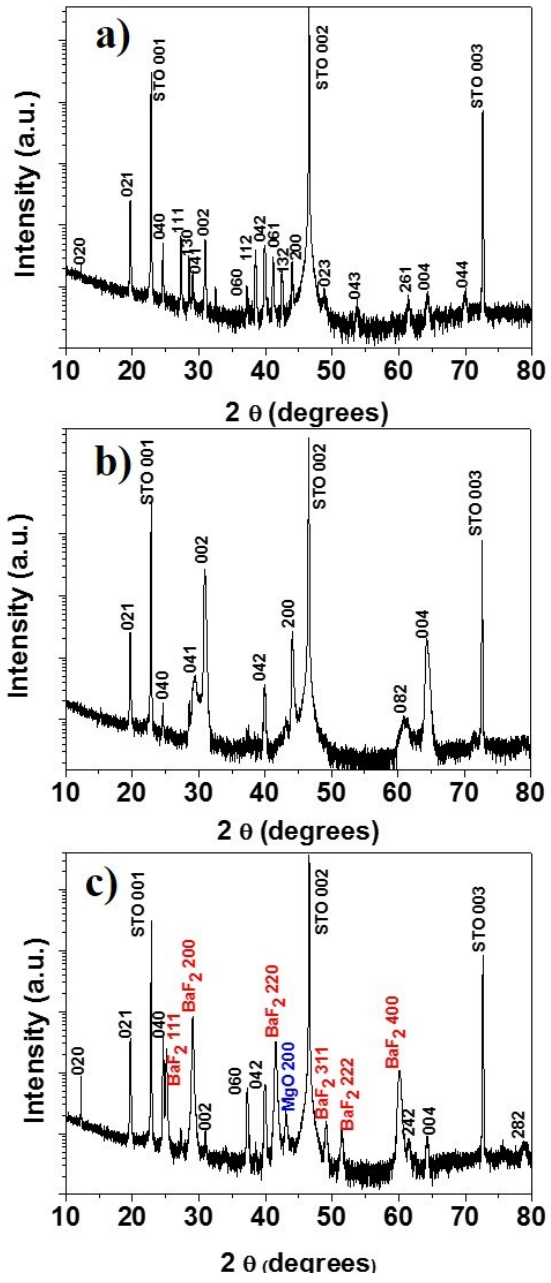

Fig. 3.2.2.1 XRD patterns of BMF films grown with LI-MOCVD on STO (001) substrates at various temperatures: a) 650, b) 675°C and c) 700°C with a P_{O_2} of 3.0 Torr.

The films composition has been assessed through EDX and wavelength X-ray (WDX) qualitative and quantitative analysis. For films deposited at 700°C and P_{O_2}= 7.1 Torr, the O K_α peak is clearly visible in the EDX spectrum (Fig. 3.2.2.2a); even at lower P_{O_2} (3.0 Torr) the oxygen signal is

detected; hence, the P_{O_2} and deposition temperature used in these experiments yield the formation of oxide phases.

Upon reducing the temperature to 675°C, the EDX spectral features (Fig. 3.2.2.2b) reveal the absence of oxygen for films deposited at P_{O_2} lower than 5 torr, confirming the formation of pure BMF phase in these conditions.

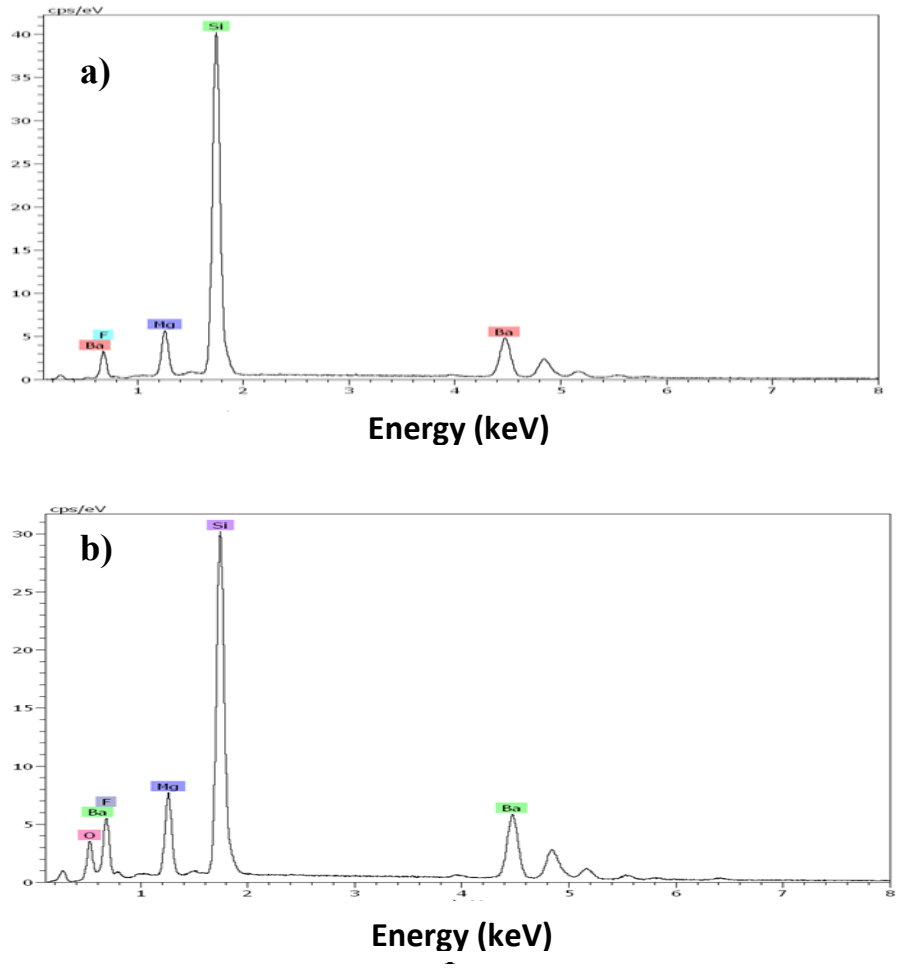

Fig. 3.2.2.2 EDX spectra of BMF film deposited with LI-MOCVD at: a) 675°C and b) 700°C.

FE-SEM investigations, summarized in figure 3.2.2.3, show a changing of surface morphology with deposition temperature. At 650°C (Fig. 3.2.2.3a), analogously to films deposited in the C-MOCVD process, the surface appears quite disordered. The effect of the film orientation upon increasing the temperature is evident in the morphology of BMF films deposited at 675°C (Fig.3.2.2.3b). In this

case, rectangular-shaped grains of about 1 µm in dimension are arranged in a textured fashion on the surface, showing two main different directions.

Finally, the micrograph of films deposited at 700°C is reported in figure 3.2.2.3e. The surface aspect in this case is completely different; this is likely due to the presence of the impurity BaF_2 and MgO phases in the films deposited at this temperature. The thicknesses of the films, measured by FE-SEM cross section analysis, and reported in fig. c and d, are about 400-500 nm for films deposited at 650 and 675°C, respectively.

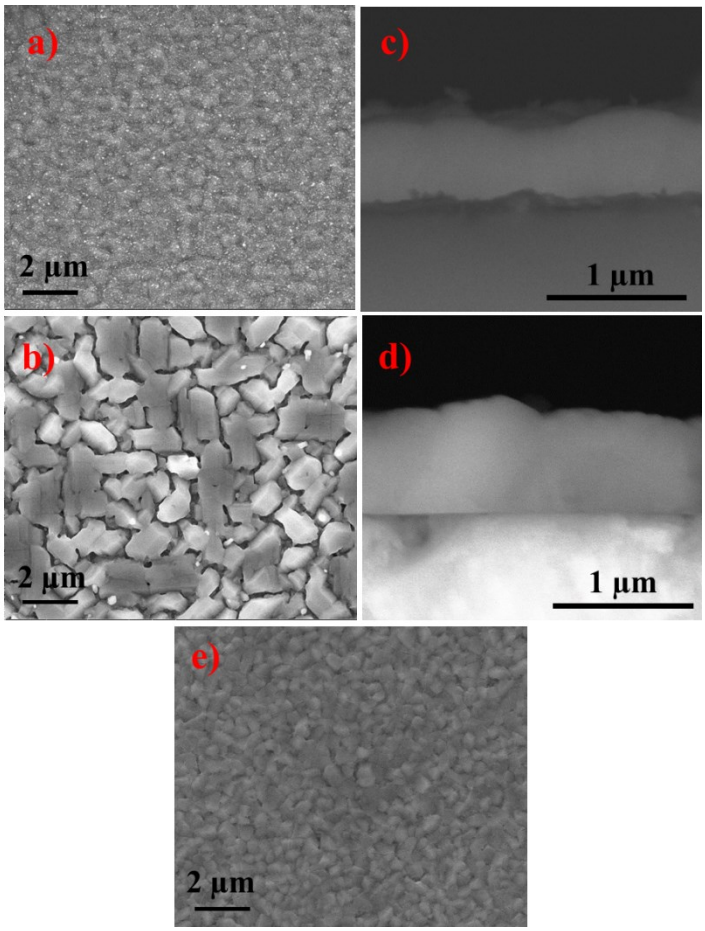

Fig. 3.2.2.3 FE-SEM images of BMF films deposited with LI-MOCVD at a) 650, b) 675°C and e) 700°C with a P_{O_2} of 3.0 Torr. FE-SEM Cross-section images of BMF films deposited at c) 650 and d) 675°C.

To confirm the epitaxial growth of the BMF film deposited at 675°C on STO (001) transmission electron microscopy (TEM) analyses have been carried out. The bright-field cross-section TEM image (Fig.3.2.2.4b) shows a quite sharp film/substrate interface which indicates that no chemical

interaction occurred. Moreover, in the image [100] and [110] zone axis grains can be distinguished. Figures 3.2.2.4a c and 3.2.2.4c show the selected-area electron diffraction (SAED) patterns collected along the [100] and [110] zone axis of BMF film observed with an incident electron beam perpendicular to the sample cross-section.

Both cross-section SAED pattern, taken in an area covering both the substrate and the film, are a simple superposition of the BMF film and STO substrate spots. The STO spots are perfectly coincident with those from the BMF films, indicating that the deposited films possess epitaxial relationship with the substrate plane.

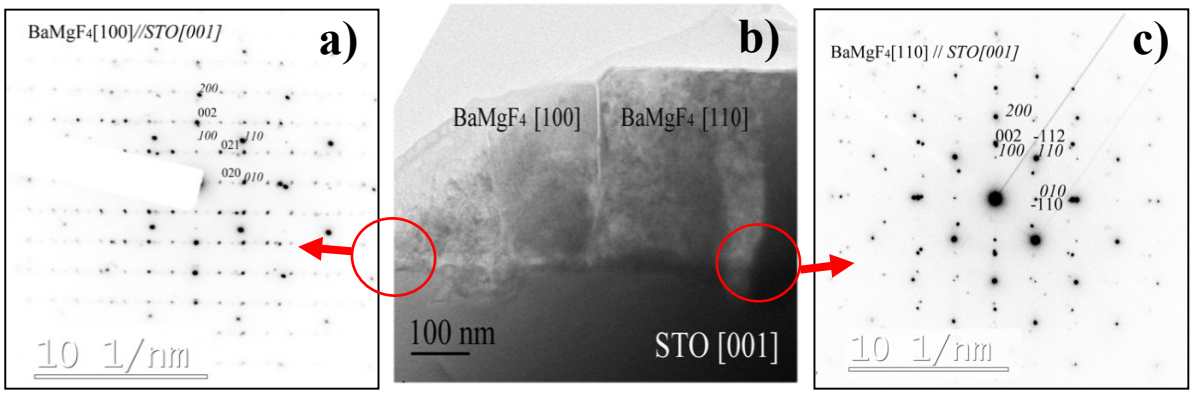

Fig. 3.2.2.4 SAED patterns of the a) BMF [100]/ $SrTiO_3$ [001] substrate and c) BMF [110]/ $SrTiO_3$ [001] substrate; b) bright-field image of the cross-section BMF film/$SrTiO_3$ substrate.

After the standardization of the synthesis of pure BMF films, manganese doped BMF films were grown on Si and STO (001) substrates at 675°C, aiming to synthetize a potential multiferroic system. EDX and WDX measurements were performed to determine the incorporation of manganese in the films and its concentration. Both analyses were conducted on films deposited on silicon substrates; indeed, the strontium titanate is not suited due to the presence of oxygen in the STO substrate and to the potential overlap between Ba L lines and Ti K lines deriving from the substrate. The EDX spectrum, reported in Fig. 3.2.2.5, shows the presence of the Mn peak related to K lines, at 5.9 keV.

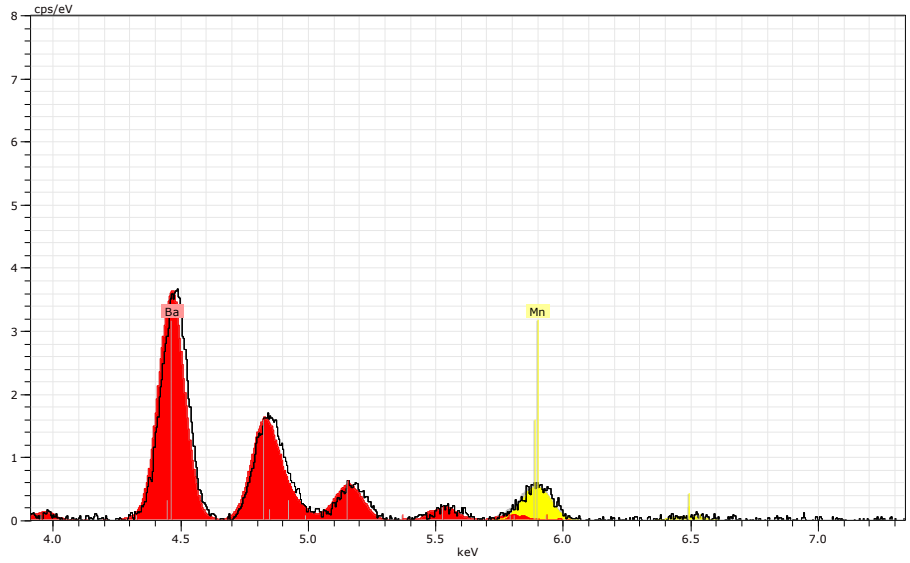

Fig. 3.2.2.5 Zoom in the zone of manganese of EDX spectrum obtained for Mn-doped the BMF film grown on silicon substrate.

The Mg /Mg + Mn ratios in the film, as determined by EDX and WDX, as a function of Mg/Mg+Mn ratio in the solution are depicted in Fig 3.2.2.6. The results indicate the very good control of Mn doping of the films with the molar ratio of $Mn(hfa)_2tmeda/(Mg(hfa)_2(diglyme)_2(H_2O)_2 + Mn(hfa)_2tmeda)$ precursors.

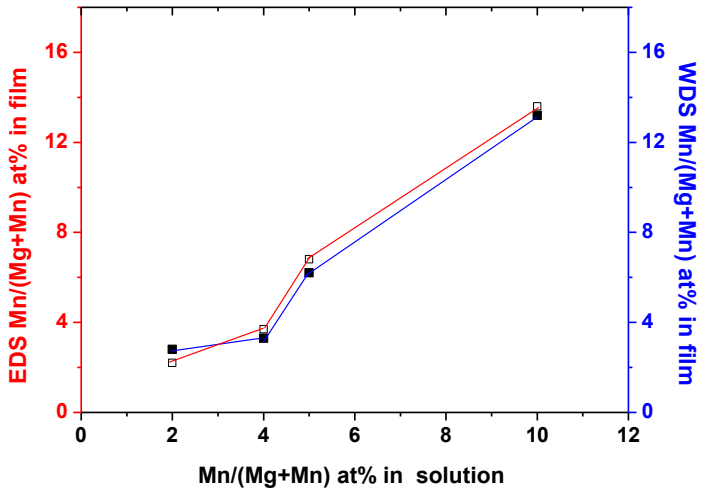

Fig. 3.2.2.6 Mn concentration in the film (Mn/Mg+Mn) for different molar ratio of $Mn(hfa)_2tmeda/(Mg(hfa)_2(diglyme)_2(H_2O)_2 + Mn(hfa)_2tmeda)$.

3.2.3 Effect of the substrate on BMF film properties

BMF films were grown through Liquid-Injection MOCVD on different substrates using the depositions conditions already optimized on STO (001). The aim was to investigate the substrate effect on the film microstructure. BMF films grown on Si (001) have been studied in regard to film structure and its crystallinity by X-Ray diffraction analysis. In Fig. 3.2.3.1a is reported the XRD pattern of the BMF film deposited on Si (001) substrate. The presence of all the BMF reflections, showing intensities that match those reported in the database, clearly points to the polycrystalline nature of the films. The field-emission scanning electron microscopy (FE-SEM) image of the polycrystalline BMF film obtained on Si (001), shows the presence of grains having dimensions of about 1 micron (Fig. 3.2.3.1b).

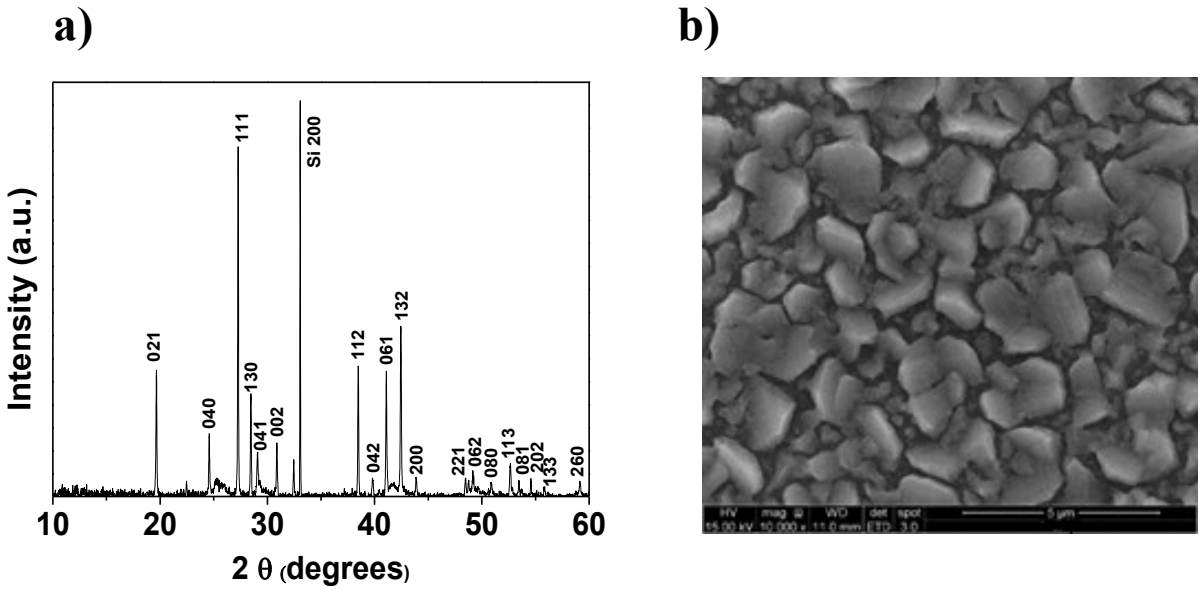

Fig. 3.2.3.1 XRD pattern (a) and FE-SEM image (b) of the BMF film grown on Si (001) substrate.

BMF films were grown on differently oriented $SrTiO_3$ substrates, to investigate the substrate influence on the crystallographic properties. The XRD results are summarized in Fig. 3.2.3.2. The θ–2θ pattern of films obtained on STO (110) exhibit only the diffraction peaks at 12.28, 24.68,

37.22, 50,40, 64.22 and 79.28°, easily assigned to the 020, 040, 060, 080, 0,10,0 and 0,12,0 BMF reflections respectively.

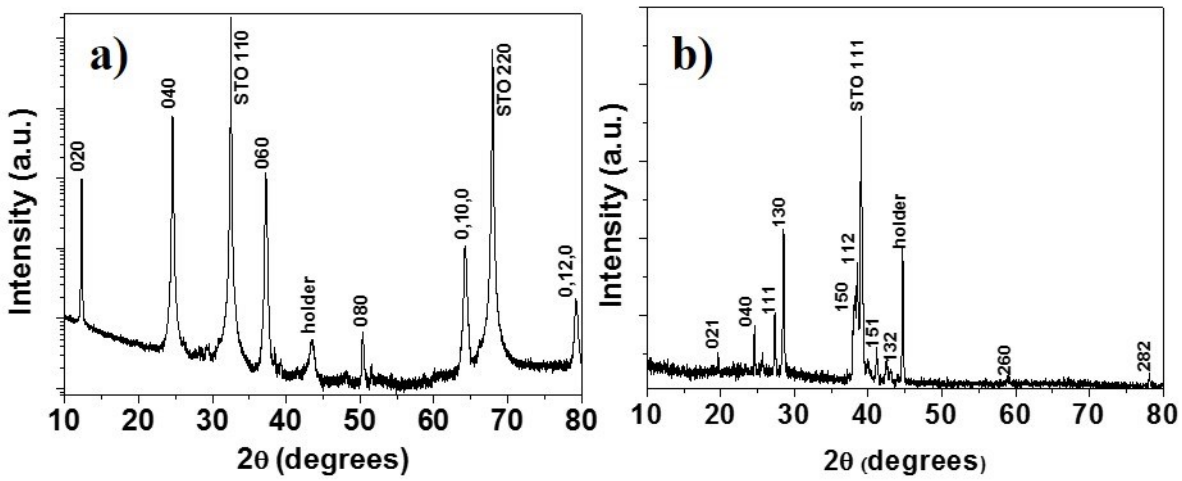

Fig. 3.2.3.2 XRD pattern of BMF films grown on a) STO (110) and b) STO (111).

The peaks at 32.54 and 67.90° are due to STO 110 and STO 220 reflections, respectively. Hence, at this temperature, it is evident the formation of highly b-axis oriented BMF films. The out-of-plane alignment of crystallites has been confirmed by recording the rocking curve of the 040 reflection (Fig. 3.2.3.3). The full width half maximum value of 1.13° indicates a low dispersion of grains.

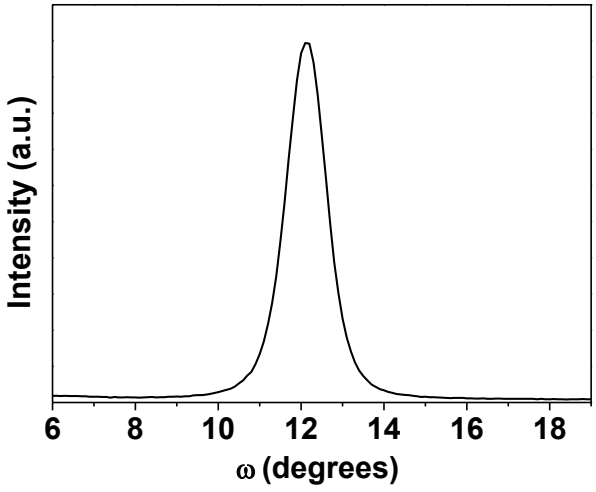

Fig. 3.2.3.3 Rocking curve of the 040 reflection of the BMF film deposited on STO (110).

The structural analysis of a sample grown on STO (111) indicates the presence of different reflections corresponding to BMF phase (Fig. 3.2.3.2b); the intensities of the pattern peaks do not match those reported in the ICDD database, thus indicating that some preferential orientation occurs. These data point to the substrate effect on the films structure. The substrate orientation influences films morphology as well. Thus, different morphology are found for films deposited on STO (110) and STO (111) (Fig. 3.2.3.4). The occurrence of a preferential orientation is evident in the micrograph representative of BMF films deposited on STO (110) (Fig. 3.2.3.4a). In this case, rectangular-shaped grains of hundreds of nanometers show a texture typical of *b*-axis grown films. Conversely, BMF samples grown on STO (111) (Fig. 3.2.3.4b) don't exhibit a texture morphology, according to their polycrystalline nature.

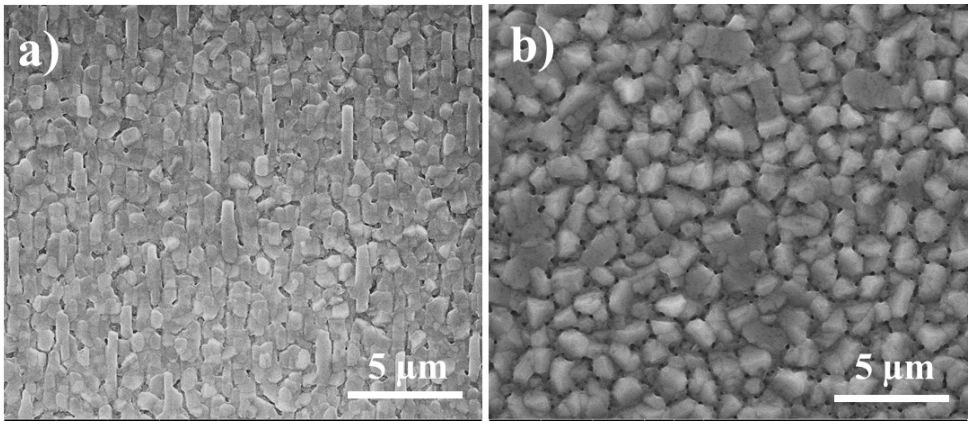

Fig. 3.2.3.4 FE-SEM images of BMF films grown on a) STO (110) and b) STO (111).

3.2.4 Ferroelectrical characterization

The ferroelectric/piezoelectric properties of obtained films have been investigated at the nanoscale level by PFM and single point piezoresponce force spectroscopy (PFS). Both pure and manganese doped samples have been characterized. Fig. 3.2.4.1 shows the images of the topography (a) and of the phase difference between applied oscillating potential Vac and the vertical piezoresponce Zac (b) of pure BMF film deposited at 675 °C. Fig.3.2.3.1 b and e show the topography and the phase

difference of a Mn-doped BMF sample. The atomic ratio % of Mn expresses as Mn/(Mg+Mn) is about 4%. From the comparison between topographic and phase images, it is evident the presence of domains showing different piezoelectric responses (in term of phase difference). Hence, single-point piezoresponce force spectroscopy (Fig 3.2.4.1c) obtained with a round trip of ±7 V tip bias was performed on bright domains. The plot shows that the dependence of the phase difference and, therefore, of the polarization direction upon tip bias follows a hysteresis loop with a coercive voltage of about 1 V. This behavior indicates that it is possible to determine the polarization direction of the ferroelectric domains (writing) by applying a suited potential to the AFM tip. Similar results are found in the Mn-doped samples, since a hysteresis loop is also evident.

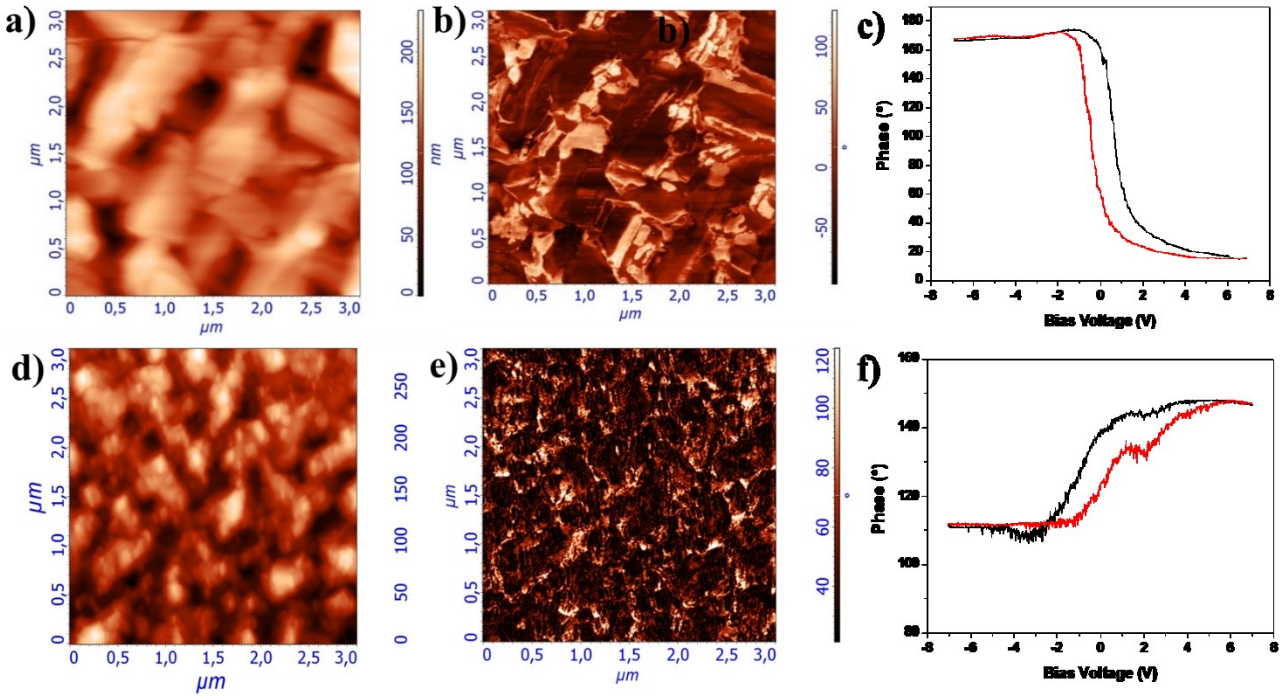

Fig 3.2.4.1 PFM and PFS characterizations of pure and Mn-doped BMF films deposited at 675 °C on Nb-STO (001). a,d) topographic and b,e) vertical PFM phase shift images of the as-grown pure and Mn-doped BMF films, respectively. Single-point PFS hysteresis loop obtained on domain by applying a round trip±8 V tip bias on c) pure BMF films and f) Mn-doped BMF films.

On the basis of the present investigation, it is possible to conclude that Piezoelectric/ferroelectric properties are present in both pure and Mn-doped deposited BMF films.

3.2.5 Comparison between Conventional and Liquid Injection approaches

The deposition of the BMF phase was achieved with the two MOCVD techniques. Herein, a comparison is given to the two different approaches considering the depositions on Si (001) and on single crystal perovskite substrate STO (001). Of all growth parameters studied, the deposition temperature and oxygen partial pressure were demonstrated to have the most crucial effect on the film formation in terms of structure and morphology. The systematic study carried out for both processes allowed to define the stability window of the BMF phase. The results are summarized in figure 3.2.5.1. The points in fig. 3.2.5.1 indicate results obtained in the C-MOCVD process (●) and LI-MOCVD (■) under different temperatures and P_{O_2} values. The oblique line divides the zone of formation of the BMF phase (left, blue points) vs. the zone of BMF decomposition (right, red points). We can summarize that the upper temperature limit is 675-700 °C, with a slight difference between the two processes and the P_{O_2}. These results can be compared with the unique data previously reported for the MOCVD growth of BMF films.[32] Reported that the BMF phase forms in a wider range from 650 °C to 850°C. Nevertheless, there are two issues that need to be considered: 1) the P_{O_2} used in the study of ref. 32 was ≤ 3.0 Torr; 2) the XRD patterns showed some impurity phase not clearly defined.

In summary, the present study indicates that the best conditions to grow crystalline, epitaxial phases are temperatures of 700°C and P_{O_2} values of about 3 Torr for the C-MOCVD, whilst for the LI-MOCVD approach the optimal conditions to synthesize pure and epitaxial films are 675°C and P_{O_2} values lower than 5 Torr. In this context, it is worthy to note that epitaxial layers are highly desirable for device fabrication.

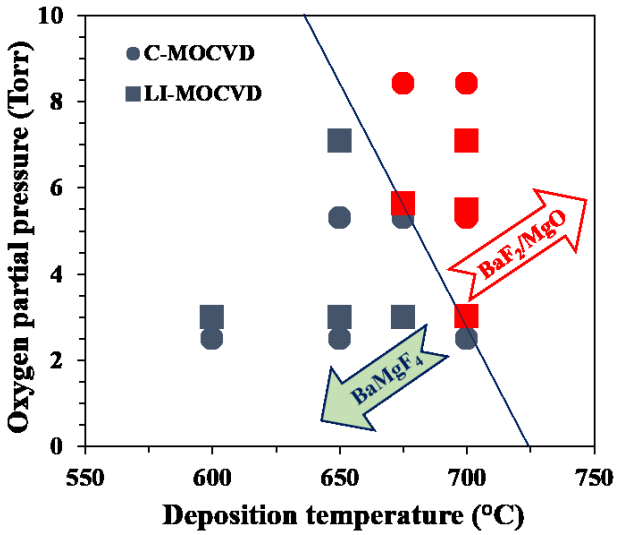

Fig. 3.2.5.1 Dependence of the BMF phase formation from deposition temperature and P_{O_2} partial pressure for C-MOCVD (●) and LI-MOCVD (■). Red points indicate films presenting BaF_2 and MgO phases.

In relation to the crystalline nature of BMF, all the as-deposited films were crystalline in both processes. The BMF films deposited in both systems exhibited polycrystalline random films at 650°C. In the C-MOCVD reactor films deposited at 700°C showed pure (010) orientation. A different situation was observed for films grown in LI-MOCVD at 675°C. In this case, films grew along two preferential directions, <021> and <002>. The different texturing observed for the film growth in the two processes deserves a further comment. To this aim it is interesting to compare the possible film/substrate alignment with the related mismatches, comparing the BMF cell parameters: a_{BMF} = 4.095 Å, b_{BMF} = 14.304 Å, c_{BMF} = 5.754 Å with respect to the substrate. The $SrTiO_3$ substrate possesses a perovskite cubic structure with a unit cell parameter a_s = 3.905 Å (ICDD N° 035-734). Various epitaxial relations can be considered and results with related mismatches are summarized in fig. 3.2.5.2 and Table 3.2.5.1, respectively. The first hypothesis might be that a 0k0 growth of BMF on STO could provide a good lattice match between film and substrate, with 2 unit cells of BMF matching well 3 unit cells of STO. The second possibility may be due to the 00ℓ growth of BMF on STO with 1 unit cell of BMF matching 4 unit cells of STO. The <h00> growth, with the c_{BMF} axis parallel to the $a_s\sqrt{2}$, is the less likely, considering the unfavorable mismatches. Finally, mismatches for the <021> growth have been evaluated. In this

case the a_{BMF} is parallel to the a_s and the (021) plane fits 5 cells of STO. For the <021> oriented growth, the in-plane lattice directions have mismatch of 4.8 and 6.0 % by matching two unit cells of BMF to five unit cells of STO.

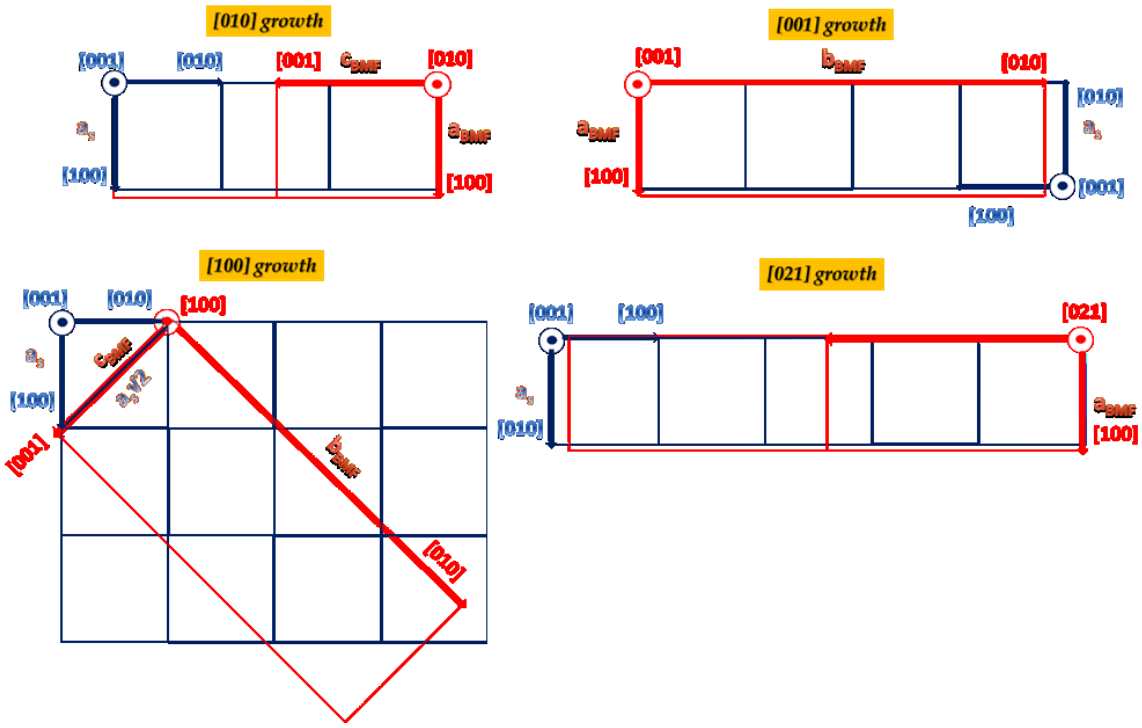

Fig. 3.2.5.2 Scheme of potential direction growths of BMF (red lines) film on STO (001) substrate (blue lines).

Direction growth	Cell relation	Mismatch 1	Mismatch 2
<010>	$a_{BMF} \parallel a_s$	$a_{BMF}/a_s = 4.8\%$	$2c_{BMF}/3a_s = 1.7\ \%$
<001>	$a_{BMF} \parallel a_s$	$a_{BMF}/a_s = 4.8\%$	$b_{BMF}/4a_s = 8.4\%$
<100>	$c_{BMF} \parallel a_s\sqrt{2}$	$c_{BMF}/ a_s\sqrt{2} = 4.2\%$	$b_{BMF}/ 3a_s \sqrt{2}=13.6\%$
<021>	$a_{BMF} \parallel a_s$	$a_{BMF}/a_s = 4.8\%$	$2cell_{BMF}/5a_s = 6.0\%$

Table 3.2.5.1 Direction growth and related mismatches.

As can be seen from the mismatch values, the <010>, <001> and <021> growths have the lower mismatches and thus are favored structures, with a small preference for the <010> direction growth. Actually these are the orientation growth observed in both cases. Furthermore, a kinetic study for the two MOCVD processes has been addressed. Growth rates of about 0,5-1μm/h have been estimated for films deposited on Si (001) and $SrTiO_3$ (001) using FE-SEM or TEM cross-section measurements. The plot of the ln growth rate vs 1000/T for films grown in LI-MOCVD system is represented in figure 3.2.5.3a. The apparent activation energy can be evaluated from data in the same Arrhenius plot. The low value of 2.9 kJ/mol clearly indicates that in the used deposition temperature range BMF film growth occurs in the mass-transport-limited regime. Concerning the films grown in the C-MOCVD reactor, also in this case the kinetic studies (fig. 3.2.5.3b) point to a weak dependence of film growth rate from process temperature. Nevertheless, it is not possible to derive any activation energy, in this case, being the slope of the fitting negative. This result is due to the reactor used for the C-MOCVD, i.e. an hot-wall reactor, and, consequently, the growth rate variation may be due to the depletion wall effect.

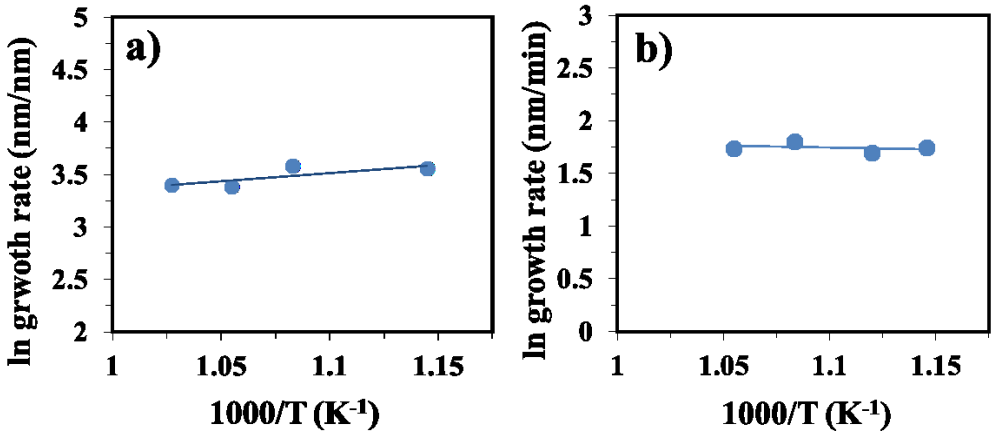

Fig. 3.2.5.3 Plot of ln growth rate vs. 1000/T for BMF films grown from a) C-MOCVD and b) LI-MOCVD.

References

[1] S. J. Patwe, S. N. Achary, A. K. Tyagi and P. N. Moorthy, *Mater. Res. Bull.*, **34**, 761 (1999).

[2] S. Kim, H. Y. Chang and P. S. Halasyamani, *Journal of the American Chemical Society*, 2010, **132**, 17684–17685.

[3] R. Lo Nigro, S. Battiato, G. Greco, P. Fiorenza, F. Roccaforte and G. Malandrino, *Thin Solid Films*, 2014, **563**, 50–55.

[4] C. Ederer and N.A. Spaldin, *Phys. Rev. B*, 2006, **74**, 024102.

[5] M. Eibschutz, H. J. Guggenheim, S. H. Wemple, I. Camlibel and M. DiDomenico, *Phys. Lett.*, 1969, **29A**, 409.

[6] F. N. Sayed, B. P. Mandal, O. D. Jayakumar and A. K. Tyagi, *AIP Advances*, 2013, **3**, 072133.

[7] L. Mateos, M. O. Ramirez, Mariola, I. Carrasco, P. Molina, J. F. Galisteo-Lopez, E. G. Villora, C. de las Heras, K. Shimamura, C. Lopez and L. E. Bausa, *Advanced Functional Materials*, 2014, **24**, 1509-1518.

[8] N. Kodama, T. Hoshino, M. Yamaga, N. Ishizawa, K. Shimamura and T. Fukuda, *Journal of Crystal Growth*, 2001, **229**, 492–496.

[9] A. Wu, Z. Wang, L. Su, D. Jiang, Y. Zou, J. Xu, J. Chen, Y. Ma, X. Chen and Z. Hu, *Optical Materials*, 2014, **38**, 238-241.

[10] X. Zhang, S. Liu, X. Chen and W. Luo, *Solid State Communications*, 2015, 205, 33–38.

[11] T. E. Littleford, R. E. Jackson and Mark S. D. Read, *Phys. Status Solidi C*, 2013, **10** (2), 153-155.

[12] M. Trevisani, K. V. Ivanovskikh, M. O. Ramirez, P. Molina, E. G. Villora, K. Shimamura, L. E. Bausa and M. Bettinelli, *Journal of Luminescence*, 2014, **153**, 136-139.

[13] Y. Ma, J. Chen, Junjie, Y. Zheng and X. Chen, *Applied Optics*, 2012 , **51**(22), 5432-5437.

[14] F. N. Sayed, B. P. Mandal, O. D. Jayakumar, A. Arya, R. M. Kadam, A. Dixit, R. Naik and A. K. Tyagi, *Inorg. Chem.*, 2011, **50**, 11765–11772.

[15] M. Manikandan, A. Muthukumaran and C. Venkateswaran, *Journal of Magnetism and Magnetic Materials*, 2015, **393**, 40–45.

[16] M. Manikandan, A. Muthukumaran and C. Venkateswaran, *Solid State Physics*, 2014, **1**, 1516-1517.

[17] M. Bibes and A. Barthelemy, *Nature Materials*, 2008, **7**, 425-426.

[18] J. Chen, X. Chen, A. Wu, H. Li, Y. Zheng, Z. Ma, L. Jiang and J. Xu, *Applied Physics Letters*, 2011, **98**(19), 191102/1-191102/3.

[19] K. Shimamura and E. G. Villora, *Acta Physica Polonica A*, 2013, **124**, 265-273.

[20] J. V. Garcia-Santizo, B. del Rosal, M. O. Ramirez, L. E. Bausa, E. G. Villora, P. Molina, V. Vasyliev and K. Shimamura, *Journal of Applied Physics*, 2011, **110**(6), 063102/1- 063102/7.

[21] O. Pena-Rodriguez, J. Olivares, E. G. Villora, K. Shimamura and F. Agullo-Lopez, *Journal of Luminescence*, 2013, **136**, 182-185.

[22] Z. Yan, B. Yan and L. –P. Jia, *Materials Research Bulletin*, 2013, **48**, 4402-4405.

[23] S. W. Kim, H. Y. Chang and P. Shiv Halasyamani, *Journal of the American Chemical Society*, 2010, **132**, 17684–17685.

[24] S. Ohmi, E. Tokumitsu and H. Ishiwara, *Journal of Crystal Growth*, 1995, **150**, 1104-1107.

[25] F. Preishuber-Pflügl and M. Wilkening*, Dalton Trans*., 2014, **43**, 9901-9908.

[26] S. Fujihara, S. Ono, Y. Kishiki, M. Tada and T. Kimura, Journal of Fluorine Chemistry, 2000, **105**, 65-70.

[27] U. Gross, S. Rudiger and E. Kemnitz, *Solid State Sci*., 2007, **9**, 838.

[28] S. Sinharoy, H. Buhay, M. G. Burke, D. R. Lampe and T. M. Pollak, *IEEE Transactions on ultrasonics, ferroelectrics, and frequency control,* 1991, 38 (6).

[29] W. A. Gomez-Uribe, M. Rodriguez-Velez, S. Majumder and A. Martinez-Collazo, *Integrated Ferroelectrics*, 2007, **91**, 23-36.

[30] A. Koji, M. Moriwaki, T. Ichiki, E. Tokumitsu and H. Ishiwara, *Jpn. J. Appl. Phys.*, 1997, **36,** L234-L237.

[31] S. Kitta, S. Fujihara and T. Kimura, *J. Sol-Gel Science and Technology*, 2004, **32**(1/2/3), 263-266.

[32] M. Ryazanov, I. Korsakov and N. Kuzmina, *J. Phys. IV France*, 1999, **09**, 471-478.

[33] G. Malandrino, F. Castelli and I. L. Fragala, *Inorganica Chimica Acta*, 1994, **224**, 203-7.

[34] M. E. Fragala, R. G. Toro, S. Privitera and G. Malandrino, *Chemical Vapor Deposition*, 2011, **17**, 80-87.

Chapter 4: Lanthanide-doped fluoride films

In the recent years, research on luminescent materials has shifted towards the nanoscale as an ever-increasing demand for novel, functional, nanomaterials grows, ushering with it a new era of luminescence research. To date, lanthanide (Ln^{3+}) ions doped luminescent upconversion (UC) phosphors have attracted a great interest in view of their potential applications, such as display devices, solid-state lasers, solar cell and biological imaging.[1-4]

Over the past few years, considerable efforts have been devoted to select the ideal host materials.[5,6] The choice of host materials is of great importance in designing lanthanide-based luminescent UC materials for efficient practical applications.[7] Compared with oxides, fluorides are considered to be more efficient hosts for UC luminescence of Ln^{3+} ions in terms of the low phonon energies, that allow to minimize non-radiative relaxations[8],high chemical stability and versatile synthetic strategies.[9-12] Theoretically, the host materials require close lattice matches to the dopant Ln^{3+} ions. In that regard, trivalent lanthanide ions can be successfully incorporated in the crystal structure of alkaline-earth fluorides, such as BaF_2 or SrF_2 due to ionic radius similarity,[13] even if a charge compensation mechanism is necessary to balance the extra charge introduced after substitution of the divalent alkaline earth ions with trivalent Ln^{3+} ions.[14]

Also, BaF_2 and SrF_2 are particularly suitable hosts since they have low reported cut-off phonon energies (241 cm^{-1} and 285 cm^{-1}, respectively)[15] in the same order of magnitude or at even lower energies than the cut-off phonons reported for widely used upconversion hosts such as $NaYF_4$ (360 cm^{-1}) or YF_3 (514 cm^{-1}).[16,17]

Recently, Yb^{3+}/Er^{3+} and Yb^{3+}/Tm^{3+} co-doped strontium fluoride nanoparticles have been prepared by a hydrothermal method[18-21], combustion synthesis[22] and showed unique upconversion luminescence properties.[23-28]

Single doped BaF_2 have been investigated and showed UC luminescence with a green emission dominating the spectrum.[29] So far, there are no reports on the synthesis of lanthanide doped BaF_2 and SrF_2 thin films.

4.1 MOCVD growth of pure and Yb^{3+}/Pr^{3+} co-doped BaF_2 thin films

4.1.1 Thermal characterization of precursors and MOCVD growth process

In the present study, undoped and Yb^{3+}/Pr^{3+} co-doped BaF_2 films have been deposited on silicon and quartz substrates, since for optical characterization a transparent substrate is required.

The present MOCVD process for the fabrication of Yb^{3+}/Pr^{3+} co-doped BaF_2 thin films relies upon a "unique" approach based on the use of a molten multi-component precursor source consisting of a $Ba(hfa)_2$•tetraglyme/$Yb(hfa)_3$diglyme/$Pr(hfa)_3$diglyme mixture in 1:0.6:0.03 molar ratio.

The precursor mixture has been heated at 160°C, a suitable temperature for an efficient vaporization without thermal degradation. Depositions have been carried out for 60 min under reduced pressure (5 torr) at 500° C. Argon was used as a carrier gas (flow = 150 sccm/min), while the reactant gas (oxygen flow = 150 sccm/min) was introduced in the main flow in close proximity of the reaction zone. The thermal behaviour of the mixture of precursors has been characterized by thermogravimetric analyses at atmospheric pressure under nitrogen flow.

The TG curve of the $Ba(hfa)_2$•tetraglyme/$Yb(hfa)_3$diglyme/$Pr(hfa)_3$diglyme mixture, in 1.0:1.0:1.0 molar ratio, shows mainly a single step, indicating that the mixture evaporates without decomposition in the temperature range of 170–300 °C with a low residue (∼11%).

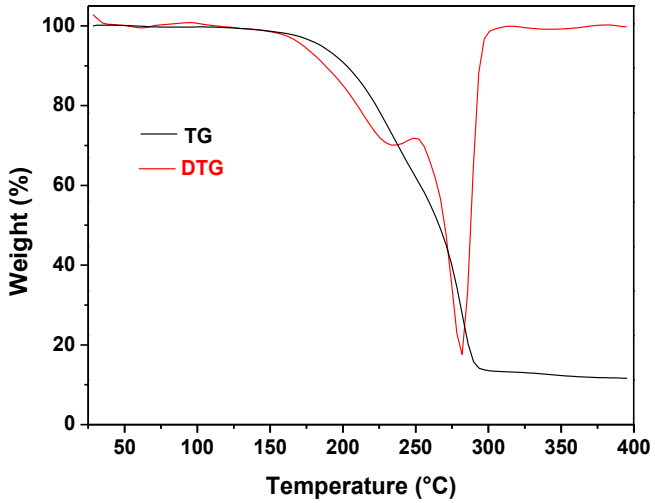

Fig 4.1.1.1 TG and DTG profiles of the multicomponent Ba(hfa)$_2$tetraglyme,Yb(hfa)$_3$diglyme and Pr(hfa)$_3$diglyme mixture.

The termogravimetric analysis shows that the Ba, Yb and Pr mixture possesses good thermal stability, and demonstrates great advantages for practical applications in depositing Yb^{3+}/Pr^{3+} co-doped BaF_2 films in MOCVD processes under vacuum.

4.1.2 Structural, morphological and compositional characterization of films

The structural analysis of deposited films was investigated by XRD measurements. The θ–2θ pattern representative of undoped BaF_2 films (Fig 4.1.2.1) deposited on silicon substrate, indicates the presence of peaks at 2θ= 24.96, 28.90, 41.30, 48.80, 51.18° corresponding to the 111, 200, 220, 311 and 222 reflections characteristics of the BaF_2 phase; the intensities of the pattern peaks match exactly those reported in the ICDD database 04-0452, thus indicating that no preferrential orientation occurs. The absence of any other peaks in the pattern suggests that no other detectable phases are formed, thus confirming the films purity.

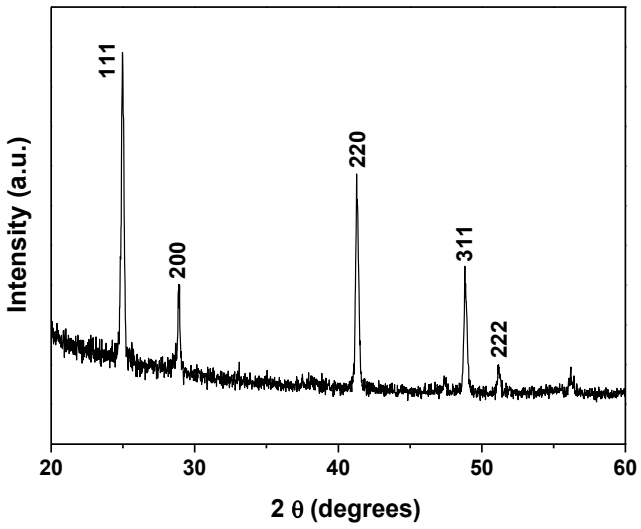

Fig. 4.1.2.1 XRD pattern of the undoped BaF_2 film deposited on Si substrate.

Polycristalline samples were obtained for the doped films, as well. In this case, peaks are found at higher 2θ values than undoped ones (Fig 4.1.2.2). According to the Bragg's law nλ=2dsenθ, at higher angles the spacing d between adjacent planes is lower, i.e. the lattice parameter a is smaller. This evidence can be explained considering the substitution of Ba^{2+} ion (ionic radius 1.42 Å , in 8-fold coordination) by the smaller Yb^{3+} (ionic radius 1.02 Å, 8-fold coordination).[30]

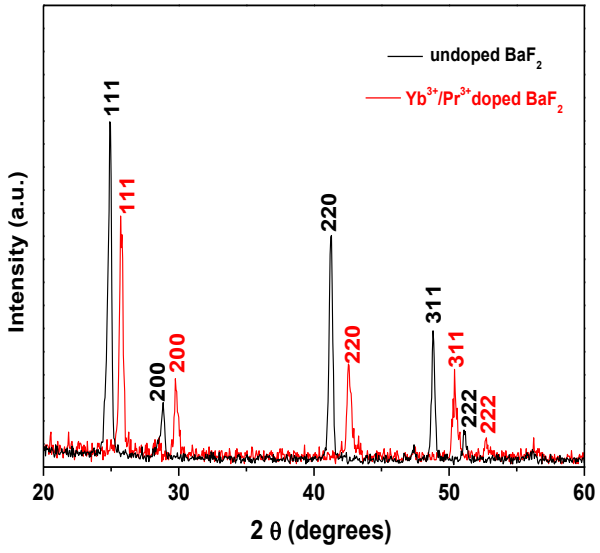

Fig. 4.1.2.2 XRD patterns of undoped and Yb^{3+}/Pr^{3+} doped BaF_2 films.

Depositions carried out on quartz substrates gave the same results. The unit cell parameter *a* has been extrapolated for undoped and doped films grown on quartz substrates following the diagram

reported in figure 4.1.2.3. The extrapolated a-axis value of undoped films is 6.1950_4 Å. On the other hand, the a-axis parameter of doped films is 6.0551_5 Å. Hence, the lattice costant for doped BaF_2 films is significantly smaller than for the undoped BaF_2 ones. The *a* axis parameter of the undoped films, that compares well with the theoretical one of 6.2001_0 Å for the bulk BaF_2 phase, indicates that these films are of good quality and stoichiometric compared to the bulk system.

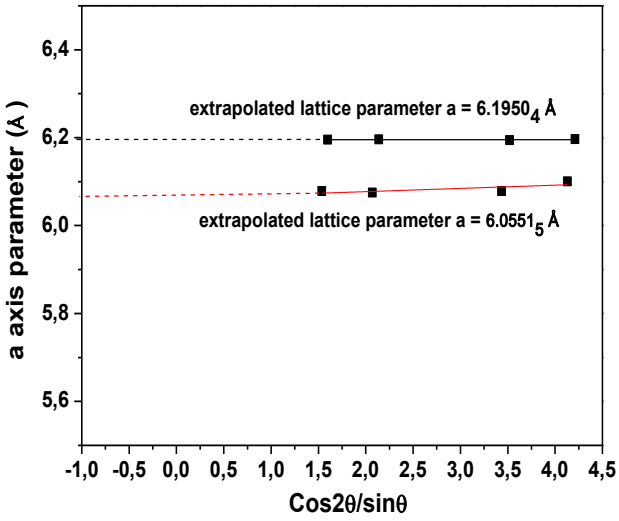

Fig 4.1.2.3 Diagram for extrapolation of a-axis parameter of undoped and doped BaF_2 phases. Red line refers to the Yb^{3+}/Pr^{3+} doped BaF_2 film, black line refers to the undoped BaF_2 film.

The films morphology was investigated by FE-SEM analysis. The micrography of a Yb^{3+}/Pr^{3+} doped BaF_2 film is reported in fig. 4.1.2.4. Film consists of grains quite homogenous of 200 nm in dimensions.

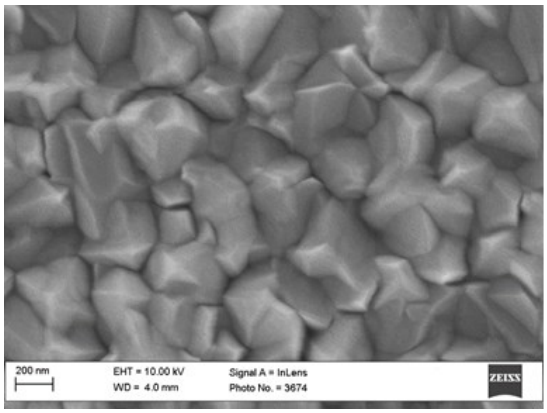

Fig. 4.1.2.4 FE-SEM image of Yb^{3+}/Pr^{3+} doped BaF_2 film.

The film composition was assessed by energy dispersive X-ray analysis. The EDX spectrum (Fig 4.1.2.5) shows, in addition to silicon K peak arising from substrate, the F K_α peaks at 0.65 keV, the Ba L lines span in the 4.3–5.5 keV, while Yb L and M peaks are found in the range of 7-8.5 keV and 1-1.8 keV, respectively.

.

a)

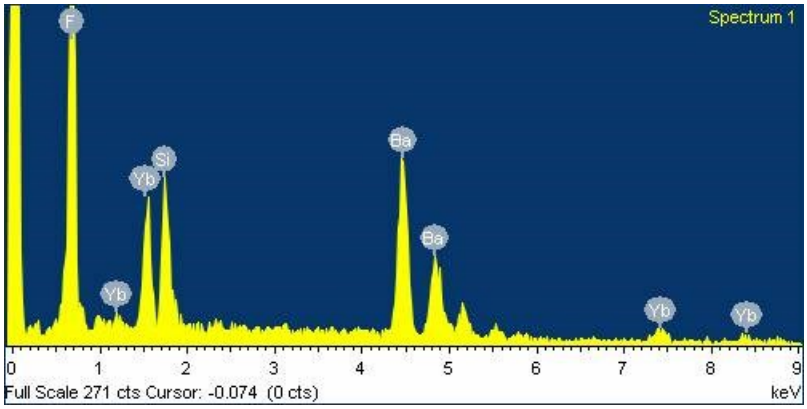

b)

Element	Weight%	Atomic%
F K	25.88	66.55
Si K	6.00	10.44
Ba L	51.44	18.30
Yb L	16.67	4.71
Totals	100.00	

Fig. 4.1.2.5 EDX spectrum (a) and quantitative analysis (b) of Yb^{3+}/Pr^{3+} doped BaF_2 films deposited on quartz substrate.

Concerning Pr, no peaks were found in the spectrum; this is likely due to the low concentration (around 1-2%) in the films. No O peaks were detected in the analysis; this confirms the actual formation of the pure BaF_2 phase and the clean decomposition of the precursors.Quantitative analysis was performed in order to establish the Yb concentration in films. The Yb concentration in films, calculated using the L lines, expressed as Yb/(Yb+Ba) at%, is about 20%, the desirable percentage for the sensitizer ion in systems for near infrared quantum cutting cooperative energy transfer.

4.2 MOCVD growth of pure and Yb^{3+}/Er^{3+} co-doped SrF_2 thin films

4.2.1 Thermal characterization of precursors and MOCVD growth process

The SrF_2 thin films have been deposited in a low pressure, horizontal, hot-wall MOCVD reactor in the 500-600°C range on silicon, MgO and quartz substrates. The choice of MgO is mandatory: indeed, on silicon or quartz substrates a correct quantification would not be possible, due to the partial overlap between Sr and Si peaks. Deposition time was 1 hour. Pure and Yb^{3+}/Er^{3+} co-doped SrF_2 films were deposited using a metal/fluorine single sources consisting of $Sr(hfa)_2$tetraglyme, $Yb(hfa)_3$diglyme and $Er(hfa)_3$diglyme in 1:0.4:0.02 molar ratio. The volatile source mixture containing the metal/fluorine single sources was loaded in a resistively heated alumina boat at 160°C and was transported through the reactor with an argon flow rate of 150 sccm in the presence of a 150 sccm oxygen reaction.

The mixture of precursors was tested at a equimolar ratio of 1.0:1.0:1.0 by thermogravimetric measurements at atmospheric pressure (Fig. 4.2.1.1).

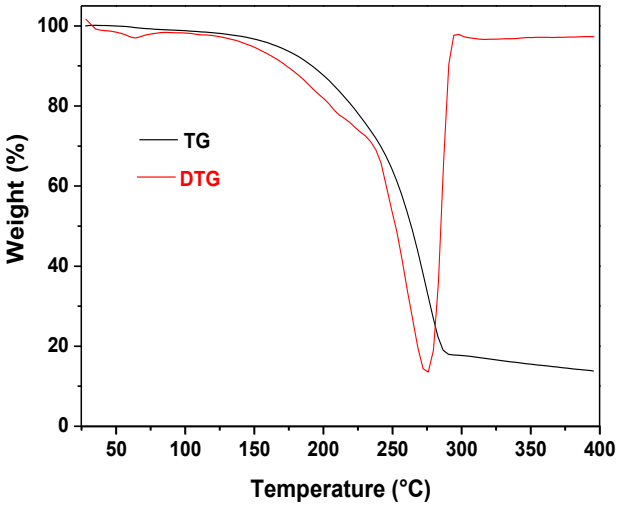

Fig. 4.2.1.1 TG and DTG profiles of the multicomponent $Sr(hfa)_2$tetraglyme,$Yb(hfa)_3$diglyme and $Er(hfa)_3$diglyme mixture.

The thermogravimetric analysis consists of a single step, indicating that the mixture evaporates without decomposition in the temperature range of 175-300°C with a low residue of 13% at 350°C. The thermal analysis indicates that the mixture possesses a good volatility and thermal stability, and therefore, it can be safely applied to MOCVD SrF_2 films growth. It is important to underline that the good thermal properties of the mixture at atmospheric pressure point to an even better behavior in MOCVD processes under vacuum.

4.2.2 Structural, morphological and compositional characterization of films

First attempts were carried out on silicon substrate, in order to find the optimal deposition parameters to grow SrF_2 phases. A typical X-ray diffraction (XRD) pattern of pure SrF_2 films deposited at 550°C is reported in Fig. 4.2.2.1.

The peaks at 26.66, 30.90, 44.20, 52.36 can be safely related to 111, 200, 220, 311 and 222 reflections of polycrystalline SrF_2 phase. No impurity phases were found.

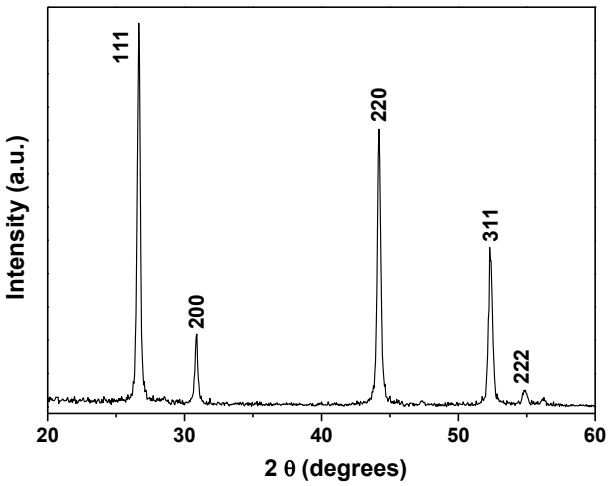

Fig. 4.2.2.1 XRD pattern of the undoped SrF_2 film deposited on Si substrate.

The structural analysis by XRD carried out for Yb^{3+}/Er^{3+} co-doped SrF_2 compared to XRD data of undoped films is reported in Fig 4.2.2.2. Also in this case the θ–2θ pattern points to the formation of the polycrystalline strontium fluoride phase. Analogously to BaF_2 thin films, also in this case a significant shift of the values of 2θ angles in the XRD pattern of doped films is observed. This can be justified by the substitution of Sr^{2+} ion (ionic radius 1.26 Å, in 8-fold coordination) by the smaller Yb^{3+} (ionic radius 1.02 Å, 8-fold coordination) (the amount of Er^{3+} ions in the SrF_2 host is almost negligible with respect to the total metal ions).

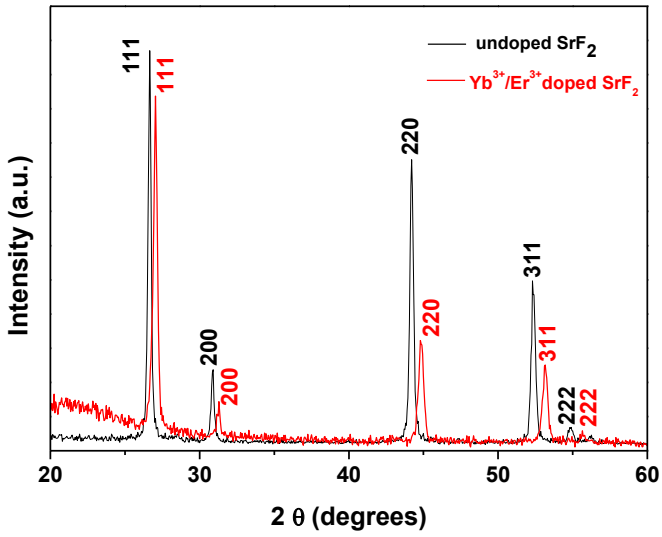

Fig. 4.2.2.2 XRD patterns of undoped and Yb^{3+}/Er^{3+} doped SrF_2 films.

The unit cell parameter *a* has been extrapolated for undoped and doped films grown following the diagram reported in figure 4.2.2.3. The extrapolated *a*-axis value of undoped films is 5.7963_7 Å. On the other hand, the a-axis parameter of doped films is 5.6963_4 Å. Hence, the lattice costant for doped SrF_2 films is significantly smaller than for the undoped SrF_2 ones. The *a* axis parameter of the undoped films, that compares well with the theoretical one of 5.80000 Å for the bulk SrF_2 phase, indicates that these films are of good quality and stoichiometric compared to the bulk system.

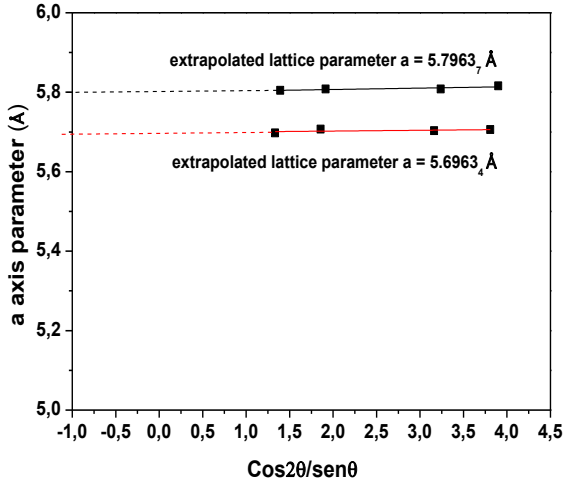

Fig. 4.2.2.3 Diagram for extrapolation of a-axis parameter of undoped and doped SrF_2 phases. Red points refer to the Yb^{3+}/Er^{3+} doped SrF_2 film, black points refer to the undoped SrF_2 film.

EDX analyses were carried out on films deposited on MgO substrate, in order to determine the composition of the SrF_2 films. The EDX spectrum reported in Fig. 4.2.2.4 shows the Sr L peaks in the range of 1.4-2 keV, the F K peak at 0.65 keV and the Yb L and M peaks in the range of 7-8.5 keV and 1-1.8 keV, respectively. In addition, the windowless EDX detector didn't detect the O peaks, thus allowing to confirm the only presence of fluoride phases. The quantitative analysis on Yb L peaks (the quantification using the M lines is not possible due to overlap between Yb M, Mg K and Sr L lines) allowed to define the Yb concentration in films. From the data acquired the ratio Sr/(Yb+Sr) at% is about 20%, the suited ratio for applications. As regards the erbium, from EDX

analysis is not possible to determine its presence, since the concentration of Er^{3+} ions in the SrF_2 host theoretically is 1%, almost negligible and under the 1% technique sensitivity.

a)

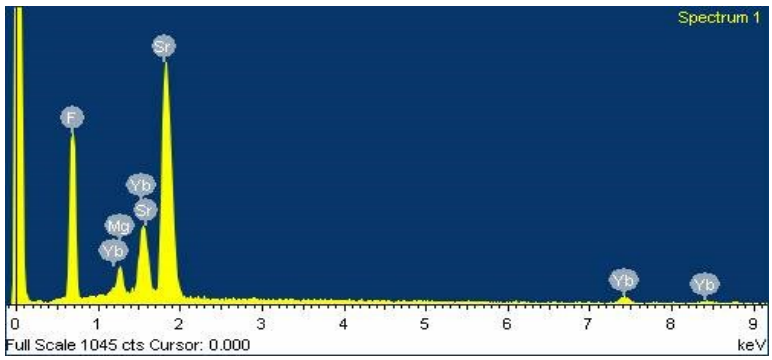

b)

Element	Weight%	Atomic%
F K	29.09	66.84
Mg K	2.20	3.26
Sr L	48.25	24.04
Yb L	20.46	5.86
Totals	100.00	

Fig 4.2.2.4 EDX spectrum (a) and quantitative analysis (b) of Yb^{3+}/Er^{3+} doped SrF_2 film.

The morphology of the films has been analyzed by FE-SEM investigations. Films consist of cubic-like grains having very small diameters of about 100-150 nm (Fig. 4.2.2.5).

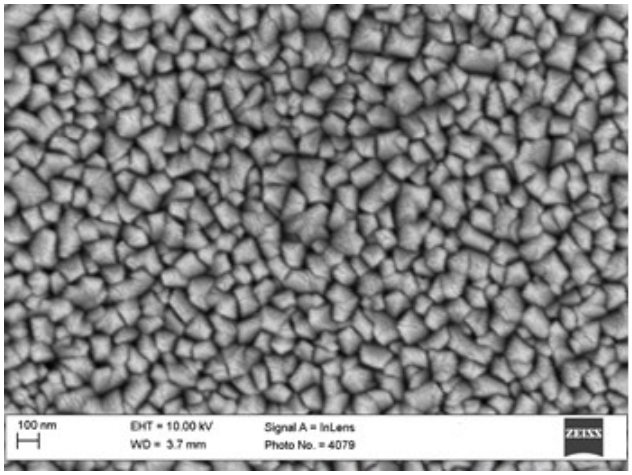

Fig 4.2.2.5 FE-SEM image of Yb^{3+}/Er^{3+} doped SrF_2 film.

References

[1] F. Auzel, *Chem. Rev.*, 2004, **104**, 139-172.

[2] X. Huang, S. Han, W. Huang and X. Liu, *Chem. Soc. Rev.*, 2013, **42**, 173-201.

[3] F. Wang, D. Banerjee, Y. Liu, X. Chen and X. Liu, *Analyst*, 2010, **135**, 1839-1854.

[4] E. Downing, L. Hesselink, J. Ralston and R. Macfarlane, *Science*, 1996, **273**, 1185-1188.

[5] F. Wang and X. Liu, *Acc. Chem. Res.*, 2014, **47**, 1378-1385.

[6] H. Lian, Z. Hou, M. Shang, D. Geng, Y. Zhang and J. Lin, *Energy*, 2013, **57**, 270-283.

[7] X. Zhang, Z. Chen and J. Qiu, *Materials Chemistry and Physics*, 2015, **162**, 76-81.

[8] G. Wang, W. Qin, J. Zhang, L. Wang, G. Wei, P. Zhu and R. Kim, *J. Alloys Compd.*, 2009, **475**, 452-455.

[9] C. X. Li, J. Yang, P. P. Yang, X. M. Zhang, H. Z. Lian and J. Lin, *Cryst. Growth Des.*, 2008, **8**, 923–929.

[10] S. J. Zeng, J. J. Xiao, Q. B. Yang and J. H. Hao, *J. Mater. Chem.*, 2012, **22**, 9870.

[11] L. Y. Wang and Y. D. Li, *Chem. Mater.*, 2007, **19**, 727–734.

[12] L. Xiang, G. Ren, Y. Mao, J. He and R. Su, *Optical Materials*, 2015, **49**, 6–14.

[13] R. D. Shannon and C. T. Prewitt, *Acta Crystallogr. B*, 1970, **26**, 1046−1048.

[14] M. Pedroni, F. Piccinelli, T. Passuello, M. Giarola, G. Mariotto, S. Polizzi, M. Bettinelli and A. Speghini, *Nanoscale*, 2011, **3**, 1456− 1460.

[15] W. Hayes, Crystals with the Fluorite Structure: Electronic, Vibrational and Defect Properties, Oxford University Press, Oxford, UK, 1974.

[16] M. M. Lage, A. Righi, F. M. Matinaga, J. Y. Gesland and R. L. Moreira, *J. Phys.: Condens. Matter*, 2004, **16**, 3207.

[17] J. Suyver, J. Grimm, M. K. van Veen, D. Biner, K. W. Kramer and H. U. Gudel, *J. Lumin.*, 2006, **117**, 1–12.

[18] M. Quintanilla, I. X. Cantarelli, M. Pedroni, A. Speghini and F. Vetrone, *J. Mater. Chem. C*, 2015, **3**, 3108—3113.

[19] P. Rodríguez-Sevilla, H. Rodríguez-Rodríguez, M. Pedroni, A. Speghini, M. Bettinelli, J. García Solé, D. Jaque and P. Haro-González, *Nano Lett.*, 2015, **15**, 5068−5074.

[20] M. Pedroni, F. Piccinelli, T. Passuello, S. Polizzi, J. Ueda, P. Haro-Gonzalez, L. M. Maestro, D. Jaque, J. Garcia-Sole, M. Bettinelli and A. Speghini, *Cryst. Growth Des.*, 2013, **13**, 4906–4913.

[21] J. Sun, J. Xian, X. Zhang and H. Du, *Journal Of Rare Earths*, 2011, **29**, 32-37.

[22] R. Nikifor, R. B. Guimarãesb, D. F. Franceschini, S. M. Glauco and S. Maciel, *Materials Chemistry and Physics*, 2012, **135**, 317-321.

[23] J. Zhang, L. Zhang, L. Shaozhe and W. Qin, *J. Nanosci. Nanotechnol.*, 2010, **10**, 1974−1976.

[24] D. Q. Chen, Y. L. Yu, F. Huang, P. Huang, A. P. Yang and Y. S. Wang, *J. Am. Chem. Soc.*, 2010, **132**, 9976−9978.

[25] N.-N. Dong, M. Pedroni, F. Piccinelli, G. Conti, A. Sbarbati, J. E. Ramírez-Hernandez, L. M. Maestro, M. C. Iglesias-de la Cruz, F. Sanz-Rodriguez, A. Juarranz, F. Chen, F. Vetrone, J. A. Capobianco, J. G. Sole, M. Bettinelli, D. Jaque and A. Speghini, *ACS Nano*, 2011, **5**, 8665−8671.

[26] G. Wang, Q. Peng and Y.Li, *J. Am. Chem. Soc.*, 2009, **131**, 14200− 14201.

[27] J. Y. Sun, J. B. Xian and H. Y. Du, *Appl. Surf. Sci.*, 2011, **257**, 3592.

[28] X. Qiao, X. Fan, Z. Xu and X. Xu, *Journal of Non-Crystalline Solids*, 2011, 357, 83–87.

[29] Z. Xiaowen, C. Zhi and Q. Jianrong, *Materials Chemistry and Physics*, 2015, **162**, 76-81.

[30] R. D. Shannon and C. T. Prewitt, *Acta Crystallogr. B*, 1970, **26**, 1046−1048.

Conclusions

In this PhD thesis, an overview of the MOCVD fabrication of different fluoride phases having multifunctional properties has been provided. As a preliminary study, before applications of the precursors to the multicomponent fluoride films, the metalorganic precursors have been applied to the deposition of binary phases. In particular, the interest has been devoted to the detailed study of the metal sources of Ba, Mg and Ni needed for the growth of ferroelectric and multiferroic systems of formula $BaMF_4$ (M = Mg, Ni) and on the other hand Na, Y, Gd to be applied to the synthesis of host lattice fluorides for lanthanide ions, such as $NaREF_4$ (RE=Y,Gd). In the case of Ba and, for comparison of the host matrix properties, of Sr sources, they have been applied to the synthesis of BaF_2 and SrF_2 films, which possess physical properties of great technological interest in the field of upconversion luminescence. Barium, strontium and magnesium precursors have been just synthesized and characterized, since they were already known in literature. Concerning the Ni precursors, a new synthetic strategy has been presented for the $Ni(hfa)_2$tmeda source, and this precursor has been compared to the $Ni(tta)_2$tmeda in regard to fabrication of NiO thin films. The results indicate that NiO films obtained from $Ni(tta)_2$•tmeda precursor show both morphological and optical properties better than those found for samples grown from $Ni(hfa)_2$•tmeda, thus indicating that the former precursor is more suitable to the MOCVD growth of high quality NiO films. Furthermore, NiO films have been grown on AlGaN/GaN heterostructures. TEM characterization demonstrated that the films are highly oriented and that the film/substrate interface has a good quality. In particular, the NiO thin films showed a perfect <111> epitaxy. Electrical characterization demonstrated that the epitaxial films have dielectric constants very close to the bulk values, and therefore are promising insulators for GaN devices. In addition, the good quality dielectric thin films have been formed at a deposition temperature (500°C) significantly lower than

those usually required for MOCVD thin film synthesis, and this finding represents an important issue since lower deposition temperatures are highly desirable for multilayer device fabrication.

In regard to $NaREF_4$ phase films, two new heterobimetallic adducts have been synthesized: $[Y(hfa)_4]^-[Na•tetraglyme]^+$ and $[Gd(hfa)_4]^-[Na•tetraglyme]^+$. The structural and thermal characterization showed that both possess very good mass transport properties, as required for MOCVD processes. These results can be considered an important advance since the availability of a single source heterobimetallic MOCVD precursor, containing all the required elements (Na,Y,F) in a single molecule, ensures greater homogeneity at atomic level, the absence of unnecessary contaminating ions and also an easier control of the process.

In regard to $BaNiF_4$ films, the structural characterization showed that the formation of nickel oxide is preferential to the fluoride one, thus hampering the formation of mixed-metal fluoride phases. The interest has been turned into another phase of great technological interest, the $BaMgF_4$. BMF films were grown through two different MOCVD techniques, the conventional and liquid-injection processes. In both cases, the characterizations show the formation of the desired phase and the strong influence of deposition parameters, in particular oxygen partial pressure and substrate temperature, onto the structural, morphological and compositional properties of the films. In particular, the present study indicates that the best conditions to grow crystalline, epitaxial phases are temperatures of 700°C and P_{O_2} values of about 3 Torr for the C-MOCVD, whilst for the LI-MOCVD approach the optimal conditions to synthesize pure and epitaxial films are 675°C and P_{O_2} values lower than 5 Torr. In this context, it is worthy to note that epitaxial layers are highly desirable for device fabrication.

The ferroelectrical characterization of BMF films grown with LI-MOCVD process allowed to evidence the presence of different piezoelectrical domains; the hysteresis loop of these domains showed a coercitive voltage around 2V. Manganese-doped films have also been synthesized, in order to achieve the multiferroic properties. The PFM characterization showed a ferroelectrical

behavior for these films too. The magnetic measurements are in progress to investigate the multiferroic properties of the films.

Finally, rare earth doped BaF_2 and SrF_2 thin films have been successfully fabricated through an MOCVD process using a molten multimetal source. Structural analysis indicated the formation of the barium and strontium fluoride phases, with no impurities. From compositional analysis through EDX it is possibile to evidence the presence of Yb dopant in the desired atomic % (20%). The a axis parameter has been extrapolated for the undoped and doped films; the doped barium and strontium films show smaller values of the cell parameters, due to the substitution of Sr and Ba by the smaller Yb. The luminescent properties are under investigation.

These results open the route to the fabrication of lanthanide-doped BaF_2 and SrF_2 films, that represent among the most studied materials for upconversion luminescence.

In conclusion, present data indicate that this MOCVD approach has the advantage of being a very simple method for the easy production of functional fluoride materials in different fields of application. In all cases the MOCVD routes have shown great flexibility and proven to be a really intriguing challenge for implementation on large scale processes that could be superior or, at least, complementary to other methodologies.

Appendix: Experimental details

Precursor mass transport characterization. Infrared transmittance spectra were recorded using a Jasco FT/IR-430 spectrometer as Nujol mulls between NaCl plates. Thermogravimetric (TG) measurements of the precursors were performed using a Mettler Toledo TGA/SDTA 851^e .The weight of the samples was between 10–15 mg (TG). Thermal investigations were carried out at atmospheric pressure, under purified nitrogen, fed into the working chamber with a flow of 30 sccm. The differential scanning calorimetry measurements of the precursors have been carried out under purified nitrogen flow (30 sccm) at atmospheric pressure using a TC10 processor and DSC 30 calorimeter. Weights of the samples were between 5 and 10 mg (DSC). For all thermal measurements, the heating rates were 5 °C/min and temperature was measured with an accuracy of ± 0.1 °C.

X-ray single crystal characterization. Cell parameters and intensity data for $[Y(hfa)_4]^-$ [Na•tetraglyme]$^+$ were obtained on an Oxford Diffraction Excalibur diffractometer using graphite monochromathed Mo-K_α radiation (λ = 0.71069 Å). Cell parameters were determined by least squares fitting of 25 centered reflections. The structure was solved using the SIR-92[1] program and subsequently refined by the full-matrix least squares program SHELX-97.[2] All the hydrogen atoms of the diglyme molecule and of the hfa anion were found in the Fourier difference map and refined isotropically. All the non-hydrogen atoms were refined anisotropically. Fluorine atoms have, as expected, rather large anisotropic factors. Atomic scattering factors and anomalous dispersion corrections for all the atoms were taken from ref. 3. Geometrical calculations were performed by PARST97.[4] The molecular plot was produced by the ORTEP-3 program.[5]

MOCVD processes. The thin films were deposited in a low pressure, horizontal, hot wall reactor (diameter = 25 mm, length = 800 mm) equipped with a single sublimation zone. The precursors were placed in an Al_2O_3 boat, resistively heated at the appropriate vaporization temperature, inside

the reactor in the sublimation zone. The vaporized source materials were transported through argon gas flow to the deposition zone. Oxygen flow was used as reaction gas. The carrier and reactive gas flow, controlled with MKS 1160 flowmeters using an MKS type 247 electronic control unit. were introduced in close proximity to the reaction zone.

Film characterization. Samples were characterized by X-ray diffraction (XRD) in the Bragg–Brentano (θ–2θ) configuration with the Cu Kα1 radiation (0.15406 nm) operating at 40 KV and 30 mA. Two different systems were used: a Bruker D8 Advance diffractometer and a θ-θ Bruker–AXS D5005 diffractometer. Phi-scan and ω-scan rocking curves were recorded on a θ-θ Bruker–AXS D5005 diffractometer or in a D5000 Siemens diffractometer. Films morphology was observed by field-emission scanning electron microscopy (FE-SEM) using a FEI Quanta or a ZEISS VP 55 microscope. Cross-section samples for TEM observation were obtained by the tripod method. Samples were polished on both sides using diamond impregnated films from 15 mm sequentially down to 0.5 mm until they were less than 15 mm thick. Low-angle ion beam milling was used for final perforation of the samples and to minimize contamination. TEM and electron diffraction were achieved with a JEOL 2011 microscope operating at 200 kV with a 0.19-nm point-to-point resolution. Energy dispersive X-ray analyses (EDX) spectra were obtained using a Oxford Inca Energy detector. Raman spectra were acquired using a LabRAM HR Horiba-Jobin Yvon spectrometer with the 473 nm excitation under ambient conditions at low laser power (<1 mW) to avoid laser-induced damage. Optical characterization was performed by spectroscopic ellipsometry (SE) and optical absorption. Spectrophotometric measurements from 300 nm to 800 nm were taken at near-normal incidence on a double-beam Jasco V-650 spectrophotometer. SE measurements were carried out in the range of 0.75-6.5 eV with a phase-modulated spectroscopic ellipsometer (UVISEL-Jobin Yvon) at an angle of incidence of 70° to determine film thickness and optical properties, namely, the refractive index, n, the extinction coefficient, k, and optical bandgap.

For simultaneous topographic and piezoelectric properties evaluation, atomic force and piezoresponce force microscopies (AFM and PFM) were performed adopting Au-coated silicon tips.

[1] Altomare, A.; Cascarano, G.; Giacovazzo, C.; Guagliardi, A.; Burla, M.C.; Polidori, G.; Camalli, M. *J. Appl. Crystallogr.* **1994**, *27*, 435.

[2] Sheldrick, G.M. SHELXL-97, University of Gottingen, Germany (1997).

[3] International Tables for X-ray Crystallography, (1974) Vol. 4, Kynoch Press, Birmingham, UK.

[4] Nardelli, M. *Comput. Chem*. **1993***, 7*, 95.

[5] Farrugia, L.J. *J. Appl. Cryst.* **1997**, *30*, 565.

List of publication

1) R. Lo Nigro, **S. Battiato**, G. Greco, P. Fiorenza, F. Roccaforte, G. Malandrino, Metal Organic Chemical Vapor Deposition of nickel oxide thin films for wide band gap devices technology. *Thin Solid Films*, 2014, **563**, 50-55.

2) R. Lo Nigro, G. Fisichella, **S. Battiato**, G. Greco, P. Fiorenza, F. Roccaforte, G. Malandrino, An insight into the epitaxial nanostructures of NiO and CeO_2 thin film dielectrics for AlGaN/GaN heterostructures. *Mater. Chem. Phys,* 2015, **162**, 461-468.

3) **S. Battiato**, M. R. Catalano, R. Lo Nigro, M. Losurdo, M. M. Giangregorio, G. Bruno, G.Malandrino, Morphology-controlled synthesis of high quality NiO films: the role of the precursor and the effect of the substrate nature on film structural/optical properties. *RSC Advances,* submitted for publication.

4) **S. Battiato**, B. Doisneau, H. Roussel, L. Rapenne, C. Jimenez, J.L. Deschanvres, G.G. Condorelli, , D. Munoz-Rojas, G. Malandrino, The quest towards multiferroic $BaMgF_4$ thin films : Conventional vs Liquid Injection MOCVD. Manuscript to be submitted.

5) **S.Battiato**, B. Doisneau, H. Roussel, L. Rapenne, C. Jimenez, J.L. Deschanvres, G.G. Condorelli, G. Malandrino, D.Munoz-Rojas, Influence of the substrate nature on $BaMgF_4$ films structure. Manuscript in preparation.

6) **S. Battiato**, Patrizia Rossi, G.Malandrino, Single-source Na-Y-F heterobimetallic complex for the deposition of $NaYF_4$ films: third-generation MOCVD precursor. Manuscript in preparation.

7) **S. Battiato**, Adolfo Speghini, G.Malandrino, Yb^{3+}/Er^{3+} doped strontium fluoride films: MOCVD growth and upconversion studies. Manuscript in preparation.

Collaborations

Within the collaboration with Dr. Carmen Jimenez, Dr. Jean-Luc Deschanvres, Dr. David Muñoz-Rojas of the Laboratoire des Matériaux et du Génie Physique (LMGP), I spent 5 months carrying out research on liquid–injection MOCVD at the LMGP, UMR 5628 CNRS – Grenoble INP Minatec 3, Parvis Louis Néel MINATEC CS 50257 38016 GRENOBLE Cedex 1, France.

Dott.ssa Patrizia Rossi, Dip. di Ingegneria Industriale, Università degli Studi di Firenze, via Santa Marta 3, Firenze (Italy): X-ray single crystal structures.

Prof. Adolfo Speghini, Dipartimento di Biotecnologie, Università di Verona, Strada Le Grazie 15, 37134 - Verona (Italy): Luminescence characterization.

Acknowledgments

Firstly, I would like to express my sincere gratitude to my advisor Prof. Graziella Malandrino for the continuous support of my Ph.D study and related research, for her patience, motivation, and immense knowledge. She provided me an excellent atmosphere for doing research and i could not have imagined having a better advisor and mentor for my Ph.D. Besides my advisor, i would like to thank the Prof. Guido Condorelli, not only for the PFM measurements described in this work, but also for his insightful comments and suggestions. My sincere thanks also go to Dr. Carmen Jimenez, Dr. Jean-Luc Deschanvres and Dr. Muñoz-Rojas, who provided me an opportunity to join their team as intern at Laboratoire des Matériaux et du Génie Physique in Grenoble, giving me access to the laboratory and research facilities. The experience abroad allowed me to grow as a research scientist and enrich my scientific knowledge. I thank my fellow labmates Dr. Maria Rita Catalano, Dr. Antonino Giuffrida, Dr. Cristina Tudisco, Dr. Anna Pellegrino, Dr. Alessandro di Mauro and Dr. Emanuele Smecca for all the fun we have had in lab in the last three years and for the countless happy lunch times spent together. I would also like to thank my family for supporting and encouraging me through the good times and bad. Last but not the least, I would like to thank my girlfiend Giulia, whose endless support, love and affection make me always feel beloved and special.

Thank you.